Mass Storage at Heterojunctions: Theory, Experimental Evidence, and Electrochemical Applications

Von der Fakultät Chemie der Universität Stuttgart
zur Erlangung der Würde eines

Doktors der Naturwissenschaften

(Dr. rer. nat.) genehmigte Abhandlung

Vorgelegt von

Chia-Chin Chen

aus Taichung, Taiwan

Hauptberichter:	Prof. Dr. Joachim Maier
Mitberichter:	Prof. Dr. Guido Schmitz
Prüfungsvorsitzender:	Prof. Dr. Joris van Slageren

Tag der Einreichung:	14.12.2015
Tag der mündlichen Prüfung:	01.02.2016

Max-Planck-Institut für Festkörperforschung

2016

To my family.

Erklärung über die Eigenständigkeit der Dissertation

Ich versichere, dass ich die vorliegende Arbeit mit dem Titel *Mass Storage at Heterojunctions: Theory, Experimental Evidence, and Electrochemical Applications* selbständig verfasst und keine anderen als die angegebenen Quellen und Hilfsmittel benutzt habe; aus fremden Quellen entnommene Passagen und Gedanken sind als solche kenntlich gemacht.

Declaration of Authorship

I hereby certify that the dissertation entitled *Mass Storage at Heterojunctions: Theory, Experimental Evidence, and Electrochemical Applications* is entirely my own work except where otherwise indicated. Passages and ideas from other sources have been clearly indicated.

Name/Name: _____

Unterschrift/Signed: _____

Datum/Date: _____

Contents

Acknowledgements

The thesis would not have been possible without the help and support from many great people. In particular, I would like to show my sincere gratitude to Prof. Joachim Maier not only for initiating the scientific concept of the project but also for directly supervising me. The valuable discussion always inspires me. I really enjoy the time to work with him.

I am also grateful to Prof. Guido Schmitz and Prof. Joris van Slageren for reviewing my thesis and being on my examination committee.

Special thanks to my early supervisor Dr. Dominik Samuelis for guiding my project and particularly training me to use molecular beam epitaxy (MBE), although this thesis does not cover my thin film research. In addition, I am grateful to Dr. Lijun Fu, who also supervised my work and generously shared her broad knowledge in chemistry.

Many colleagues assisted me in performing experiments when I started my project. Firstly, I highly appreciate Dr. Chilin Li for showing me the conductivity measurement and the thin-film fabrication technique. His valuable suggestions and discussions are acknowledged. Moreover, I would like to thank Dr. Kun Tang and Dr. Changbao Zhu for training me in battery preparation.

Special thanks to Dr. Nils Ohmer for writing the Zusammenfassung and inviting me to work in the STXM project. I will miss our wonderful beam time in BESSY.

Scientific discussion with Dr. Chao Wu is deeply appreciated. His insightful comments are helpful for experimental interpretations.

Many thanks to the technical supports from the MPI campus, I am grateful to Udo Klock for electronics, Annette Fuchs for SEM and BET, Uwe Traub for IT support, Gabi Götz for XRD, Ewald Schmitt for mechanical works, Peter Senk for glove box, Viola Duppel for TEM, Dr.

Mitsuharu Konuma for XPS, Dr. Helga Hoier for XRD, and Yvonne Link for thin film deposition.

The administrative support from Sofia Weiglein is deeply acknowledged. Furthermore, I would like to thank Dr. Hans-Georg Libuda for his kind help in the IMPRS program.

Many colleagues in the Inter-Maier family contributed in many ways to my study at MPI. I am particularly grateful to Dr. Jan Melchior, Dr. Oliver Gerbig, Dr. Michael Marino, Sebastian Stämmler, Dr. Kiran Adepalli, Michael Weissmayer, Dr. Jiyong Shin, and Dr. Elisa Gilardi.

Finally, I owe my deepest gratitude to my family. Thank my parents for their endless support and love over these years. I am always proud of being your son. Last but not least, I would like to thank my brother and sister for their inspiration. Without them I would not have the opportunity to be here.

Zusammenfassung

Die kombinierte Speicherung von Elektronen und Ionen ist das zentrale Konzept von Batteriespeichertechnologien. Konventionelle Mechanismen beziehen sich auf die homogene Speicherung von Materie in der Volumenphase eines Wirt-Materials. Erst seit Kurzem ermöglicht ein neuer Speichermechanismus die heterogene Speicherung in zwei benachbarten Phasen, von denen keine für sich allein genommen sowohl das Elektron als auch das Ion speichern kann. Diesem Mechanismus gemäß kann die Spezies M an einem Übergang zwischen einer Ionen-leitenden und einer Elektronen-leitenden Phase gespeichert werden. Hierbei geschieht die Speicherung ausschließlich in Form einer Arbeitsteilung der beiden Phasen (engl.: job-sharing mechanism): M^+ wird auf der Ionen-leitenden Seite und e^- auf der Elektronen-leitenden Seite des Kontaktes gespeichert. Ein vollständiges Verständnis des Speichermechanismus ist hierbei nicht nur von fundamentalem, sondern auch von technologischem Interesse.

Die vorliegende Arbeit gliedert sich in drei Hauptteile: Erarbeitung einer detaillierten Theorie des zugrunde liegenden Speichermechanismus, die experimentelle Validierung und die Demonstration des Mechanismus in Anwendungen. Da die gespeichert Spezies M aus verschiedenen Ladungsträgern (M^+ und e^-) besteht, korreliert der Speichermechanismus direkt mit der Defektchemie in den Volumenphasen und Raumladungszonen. Die Thermodynamik der Grenzflächenspeicherung wird umfassend für verschiedene Übergangstypen diskutiert. Das allgemeine Model umfasst drei Speicherregime: den intrinsischen Modus für geringfügige Speicherung, den von diffusiven Schichten dominierten Modus für die moderate Speicherung und den von starren Schichten dominierten Modus für die Speicherung großer Mengen. Wie der klassische Speichermechanismus, so erlaubt auch der job-sharing Mechanismus die Etablierung von Fehlstellen im Gitter, insbesondere realisiert durch die kombinierte Bildung von ionischen

Leerstellen und elektronischen Löchern. Überdies erlaubt die Variation verschiedener Parameter eine quantitative Übersicht über das Model.

Erste experimentelle Hinweise ergeben sich aus der Nichtstöchiometrie von Li in LiF/Ni-Nanokompositen. Da weder LiF noch Ni für sich allein genommen Li speichern kann, treten stöchiometrische Variationen lediglich in den Raumladungszonen der LiF|Ni Grenzflächen auf. Basierend auf dem Zusammenhang zwischen dem Gleichgewichtspotential und der Speicherkapazität sind die Ergebnisse in Einklang mit dem entwickelten Model. Die Ergebnisse sind weiterhin hilfreich für ein vereinheitlichtes Verständnis des Beitrags der Volumenphase und der Grenzflächen bei der Ladungsspeicherung in nanostrukturierten Elektrodenmaterialien.

Eine weitere experimentelle Bestätigung ist die Speicherung von Ag in $RbAg_4I_5$|Kohlenstoff-Grenzflächen. Die hergestellten elektrochemischen Zellen zeigen eine deutliche Stöchiometrievariation an den Grenzflächen des superionischen Leiters $RbAg_4I_5$ mit Kohlenstoff. Das komplette Bild der Ag-Nichtstöchiometrie umfasst: Bildung von I_2, Ag Leerstellenbildung, Ag Überschuss und Ag Abscheidung. Deweiteren ist der Prozess der Speicherung/Entfernung mit einem sehr schnellen Massetransport verbunden. Der Massetransport wird durch chemische Diffusion in Folge des job-sharings interpretiert. Im Unterschied zur klassischen chemischen Diffusion ist die Rate der heterogenen chemischen Diffusion auf Grund der Existenz des Raumladungsfeldes merklich erhöht.

In der Arbeit wird die Anwendbarkeit in verschiedenen Funktionseinheiten im Umfeld Erneuerbarer Energien wie Batterieelektroden, Superkondensatoren und Permeationsmembranen demonstriert. Ihre exzellente Performance ist auf das synergistische Konzept der Grenzflächenspeicherung zurückzuführen. Das neue Konzept bietet weitere Freiheitsgrade beim Design neuer elektronisch-ionischer Mischleiter, und es ist zu hoffen, dass es den Weg für eine neue Klasse funktioneller Verbundmaterialien ebnet.

Abstract

Mass storage is the core concept of energy storage technologies. Conventional mechanisms are to store matter homogeneously in the bulk phase of host materials. Recently, a novel storage mechanism enables one to heterogeneously store matter between two phases, even though the storage is not possible in the individual phases. According to the mechanism, the matter M could be locally stabilized at an ionic conductor/electronic conductor junction. It solely occurs in a job-sharing way: M^+ resides on the ionic conductor side of the interface while e^- on the electronic conductor side. A full understanding of the storage mechanisms is not only fundamentally important but also technologically of interest.

This thesis covers three main parts: the theory of the mechanism, the finding of experimental evidence, and the demonstration of applications. As the stored species consist of different charge carriers, it is directly correlated with the defect chemistry in the bulk and in the space charge regions. The thermodynamics of the interfacial storage is comprehensively discussed for different junction types. The generalized model includes three storage regimes: intrinsically dominated mode for marginal storage, diffusive-layer dominated mode for medium storage, and rigid-layer dominated mode for large storage. Like classic storage mechanisms, the job-sharing mechanism also allows for establishing deficiencies, realized by forming ion vacancies coupled with electron holes. Moreover, an evaluation of the parameter variation gives a quantitative overview of the model.

The first experimental evidence is the non-stoichiometry of Li in the LiF/Ni nanocomposites. As neither LiF nor Ni could accommodate Li by itself, the stoichiometric variation only occurs in the space charge regions of LiF/Ni interfaces. Based on the dependence of the equilibrium potential and the storage capacity, the result is in a good agreement with the developed model.

The understanding is helpful to unify the contributions of bulk and interfacial storage in nanostructured electrode materials.

Another experimental corroboration is Ag storage at the $RbAg_4I_5$/carbon junctions. The fabricated all-solid-state electrochemical cells show distinct stoichiometric variations at the interfaces of superionic conductor $RbAg_4I_5$ and carbon. The full picture of the Ag non-stoichiometry contains four regions: I_2 liberation, Ag deficiency, Ag excess, and Ag deposition. Furthermore, the storage/removal process is kinetically highly favorable, due to an ultrafast mass transport. The anomalous mass transport rate is interpreted by the job-sharing chemical diffusion. Different from classic chemical diffusion, the heterogeneous chemical diffusion mechanism, benefiting from an electrostatic heterogeneity effect, can significantly enhance the rate of mass transport.

Sustainable energy applications including battery electrodes, supercapacitors, and permeation membranes have been successfully verified. The excellent performance is attributed to the synergistic concept of the interfacial storage. The novel concept offers additional degrees of freedom for designing mixed electronic-ionic conductors and is hoped to pave the way for a new class of novel composite materials.

1

Introduction

Chemical energy storage is a key process for portable power. In particular, electrochemical energy storage devices such as lithium batteries provide clean, efficient, and powerful technique [1-3]. The working principle is directly related to the mass storage in the electrodes, because electrons from the external circuit and lithium ions through the electrolyte combine to lithium stored in the electrode. Therefore, the understanding of storage processes is not only fundamentally important but also technologically of interest in developing powerful energy storage devices.

Besides kinetics and charge transport, the thermodynamics of storage is at the heart of electrochemical mass storage. Since the electrode materials typically consist of crystals containing electronic and ionic charge carriers, the storage mechanisms are directly connected with the defect chemistry of the solids [4, 5]. A typical example is lithium intercalation in $LiCoO_2$[6], in which the lithium ion occupies the sites between two adjacent octahedra planes formed by cobalt and oxygen atoms and the electron is captured by the transition metal ion (Figure 1.1). Thus the lithium content in the solid solution is usually expressed as Li_xCoO_2 ($0 < x < 1$). The storage (or removal) of lithium in the electrode materials can be fulfilled by techniques such as coulometric titrations.

1. Introduction

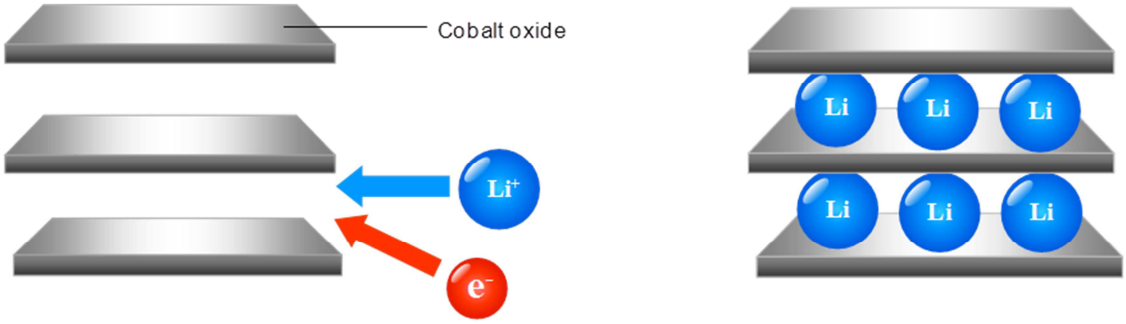

Figure 1.1 Schematic of dissociation mechanism.

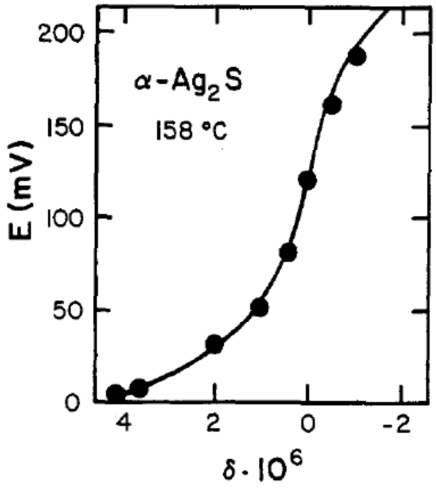

Figure 1.2 Coulometric titrations curve of Ag_2S at 158°C [7].

The nonstoichiometry in electrode materials is not limited to excess ("positive mass"). It also allows for deficiency ("negative mass"), which is connected with the presence of metal ion vacancies and electron holes. Excellently investigated solid in this context are silver chalcogenides. Wagner [8] first studied the nonstoichiometry of Ag_2S by performing coulometric titrations. A distinct stoichiometric variation including both Ag excess and deficiency was observed for Ag_2S and later also for other silver chalcogenides[9-11]. The theoretical treatment of the storage mechanism is correlated with the defect chemistry of solids. It relies on the concentrations of four charge carriers, i.e. interstitial ion, ion vacancy, electron, and holes. Taking into account the corresponding mass action laws and electroneutrality, one can derive a hyperbolic sine relationship between nonstoichiometry and chemical potential[12]. As shown in Figure 1.2, the coulometric titration curve for $Ag_{2+\delta}S$ exhibits a characteristic S-shaped feature of hyperbolic sine function, where the inflection point is the stoichiometric point (δ=0). The

Figure 1.3 Schematic of two phase transition mechanism

positive and negative δ values stand for Ag excess and deficiency, respectively. More complex defect chemistry and mathematics are encountered if the material is doped. For more details, please refer to a recent treatise on thermodynamics of lithium storage [5].

Besides the solid solution mechanism characterized by incorporating point defects in single phase, another vital storage mechanism involves phase transitions. As far as two phase systems such as $FePO_4$/$LiFePO_4$ are concerned, a reversible transformation between the two phases can happen during lithiation (i.e. from $FePO_4$ to $LiFePO_4$) and delithiation (i.e. from $LiFePO_4$ to $FePO_4$) (Figure 1.3). If one dress the analogy between Li chemical potential and temperature, the situation is analogous to the coexistence of boiling water and steam, but here we drive a transition between Li-poor solid and Li-rich solid. During phase transition the chemical potentials of each phase are invariant and only the phase fraction varies. This thus leads to the characteristic feature of such a mechanism: a voltage plateau under battery operation. The equilibrium potential of the phase transition is determined by the local two-phase equilibrium and hence by the reaction Gibbs energy. The latter becomes particularly delicate for nanocrystalline materials because the surface energy contribution to the chemical potential[13]. The lithium potential of the cell thus can be tuned by controlling the size of the electrodes[14].

The above considerations can be applied to multiphase systems as well. In lithium-based batteries, it specifically refers to conversion reactions, e.g. transformation of the transition metal oxides to transition metal/Li_2O nanocomposites, and vice versa [15]. For instance, Figure 1.4

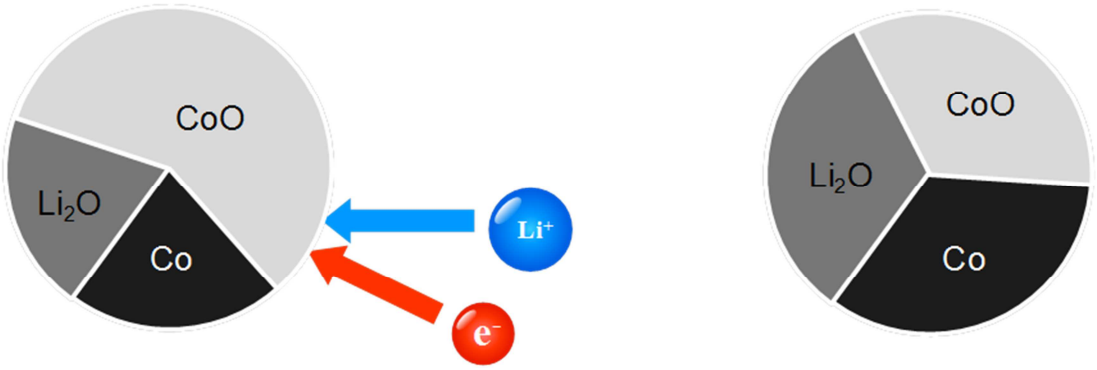

Figure 1.4 Schematic of three phase transition mechanism.

illustrates that a three-phase coexistence of CoO/Co/Li_2O takes place in the conversion from CoO. That is, the lithium can be stored in the material by reacting with CoO and meanwhile producing Co and Li_2O. Similar reactions were observed in metal fluorides and metal sulfides [16, 17]. In battery application, the mechanism may be used in anode materials providing a higher capacity than the insertion mechanism. Even though from a macroscopic thermodynamic point of view, the situation of multiphase coexistence is not different from two phase coexistence, yet surfaces/interfaces energy play a more important role. Products generated by conversion reactions are typically nanocrystalline or even amorphous. The self-formation of nanocrystals leads to a complexity of microstructure, which is a major obstacle for the cyclability of batteries. Taking FeF_2 and CuF_2 for examples, both metal fluorides can react with lithium and decompose to metal nanoparticles embedded in LiF matrices. For the former, iron nanoparticles are interconnected and form electronic pathways within the LiF phase[18]. The Fe/LiF network thus offers a bicontinuous paths for lithium ions and electrons. On the other hand, copper nanoparticles formed from CuF_2 aggregate to large particles. Even though LiF matrix still provides good ionic connection, the lack of electronic paths leads to very poor reversibility.

The aforementioned mechanisms including single phase (solid solution), two-phase transition, and the conversion reaction have been extensively investigated over decades[19]. The similarity of these mechanisms is that the mass storage has to occur in the bulk phase of the host materials. Unlike conventional bulk storage, Jamnik and Maier proposed a novel storage mechanism that can store mass at the contact of two phases[13]. It shows that, for instance, lithium could be stored at the interface even though none of the constituent phases could store lithium themselves.

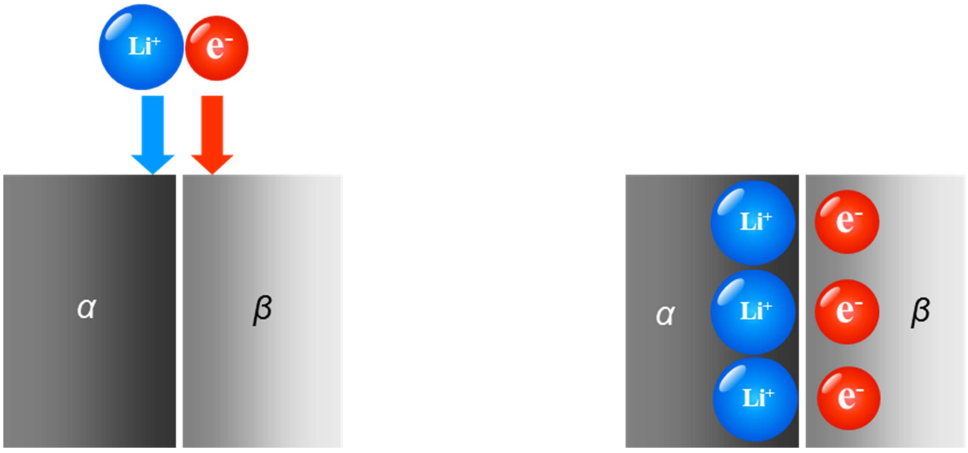

Figure 1.5 Schematic of interfacial storage mechanism.

According to this mechanism, the individual charges (Li^+, e^-) respectively localize in the space charge layers of two adjacent phases. Illustrated in Figure 1.5, the Li^+ distributes at the α phase side of the boundary while the e^- is restricted to the β phase side. Note that α can only accommodate Li^+ (but not e^-) while β can only accommodate e^- (but not Li^+). As neither of the constituents could store Li by itself, this is called "job-sharing" mechanism. Owing to individual pathways for Li^+ and e^-, the mechanism allows for fast storage and may build a bridge between a supercapacitor and a battery electrode.

The interfacial storage for lithium was first observed in Ru/Li_2O nanocomposites synthesized by the conversion reaction of RuO_2[20]. An excess capacity was observed beyond the maximal lithium content that RuO_2 could take up via the classic modes. Since Li_2O is a an ionic conductor that accommodates only Li^+ but not e^- while Ru is a metal that does not alloy with lithium, excess lithium can be stored at the interfaces of Ru/Li_2O nanocomposites. The phenomena of additional capacity beyond complete conversion reaction have been extensively reported in metal oxides and metal fluorides [16, 21]. Density functional theory calculation supported that the storage mechanism is thermodynamically favorable with the storage in metal/Li_2O being more substantial than metal/LiF, due to larger lattice constants of Li_2O [22, 23].

An excellent model material to summarize the aforementioned four mechanisms is RuO_2. As shown in Figure 1.6, RuO_2 can dissolve lithium with a solubility limit of $Li_{0.1}RuO_2$. Upon further

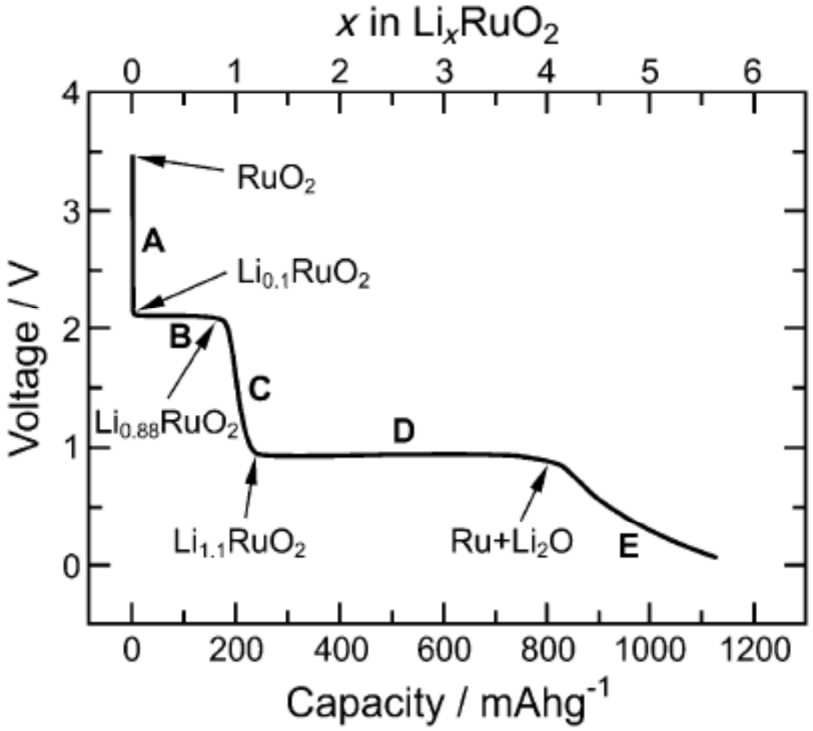

Figure 1.6 The voltage-composition curve on galvanostatic discharge of RuO_2/Li cell.[5]

lithiation a two phase reaction occurs. A potential plateau at 2.1V is clearly seen during the phase transition between $Li_{0.1}RuO_2$ and $Li_{0.88}RuO_2$. Then further lithiation drives the dissolution mechanism taking place again until the composition $Li_{1.1}RuO_2$ is reached. Like the titration curve of Ag_2S, the discharge curve in this regime also exhibits a S-shape feature, which may suggest a transition from lithium deficiency to lithium excess. The highest capacity of the material is due to the conversion reaction, during which $Li_{1.1}RuO_2$ decomposes into to Li_2O/Ru nanocomposite. Since at phase equilibrium the chemical potentials of the three components are fixed, a plateau at 0.8V is observed for the three-phase change reaction. The theoretical capacity of RuO_2 is 800 mAh/g, corresponding to 4 lithium per Ru. However, Figure 6 shows an extra capacity of 300 mA/g beyond the theoretical value. Besides passivation layers that generally form in the first discharge process, another possible way to accommodate the excess lithium is the interfacial storage. It is in particular possible in the case because the Li_2O/Ru nanocomposite has large contact area. Our recent work suggested that the extra capacity in the potential range between 0 to 1V can be reversibly charged even at high current[24]. The superior rate performance is apparently not due to the side reactions such as electrolyte decomposition.

1. Introduction

The novel interfacial storage arouses great interest in scientific understanding. It is also technologically relevant in energy storage devices and may open a new class of mixed conductors. The thesis aims at fully understanding the interfacial storage mechanism. In chapter 2, a comprehensive model in the framework of defect chemistry and space charge concept will be developed. The model addresses the thermodynamics of nonstoichiometry for different contact situations. It is shown that the stoichiometric variation includes not only excess but also deficiency like conventional bulk storage. Furthermore, the dependence of parameter variations on the model will be discussed. Chapter 3 covers experimental evidence in Li batteries. The synthesized LiF/Ni nanocomposite exhibits distinct lithium nonstoichiometry. Based on the equilibrium potential dependence on capacity, the results can be nicely interpreted by the developed model. Another example will be presented in Chapter 4, where all-solid-state Ag batteries are used to study the storage at superionic conductor/carbon contacts. Besides distinct stoichiometric variation is obtained, the storage kinetics is observed to be very fast, which leads to a novel concept of interfacial chemical diffusion. The conclusion and perspective will be discussed in Chapter 5. The development of energy storage technique is undoubtedly at the core of today's societal demands. To realize alternative powerful techniques, the proposed interfacial storage concept can provide a new perspective in forms of fundamental research. Moreover, a comprehensive understanding of the mechanism is helpful for developing interfacially controlled materials with application potential for electrodes, supercapacitors, permeation membranes, and catalysts.

2

Thermodynamics of Mass Storage at Interfaces

The thermodynamics of conventional storage mechanism, i.e. mass being stored in the bulk phase of host materials, has been far-reachingly understood. In contrast to the classic bulk storage, a novel storage mechanism that enables one to store mass at the contact of two phases – even though not possible in the individual phases – was recently proposed [13] and will be comprehensively treated thermodynamically and kinetically. The mechanism is directly connected with the local stoichiometric variation in the space charge regions. It allows for establishing not only excess but also deficiency. This chapter also discusses the effect of varying the basic parameters of the model, which gives advice for designing composite electrode materials.

2.1 Introduction

The concept of interfacial effects in solid-state ionics dates back to the 70s. Liang [25] first discovered a conductivity enhancement for LiI electrolyte if mixing some amount of insulating particles Al_2O_3. The conductivity anomaly of such composite electrolytes was later explained in the framework of space charge concept [26]. It is attributed to the local adsorption of Li^+ on the surface of Al_2O_3, leading to compensation by a high concentration of lithium ion vacancy in the space charge regions at LiI/Al_2O_3 interfaces. Over the past decades, the exploration of interfacial

effects on charge transport has significantly pushed the development of solid-state ionics. Based on the concept, many examples have demonstrated that the electrical properties can be tuned by confining the size of materials or by forming different contact situations [27-31].

The space charge model is directly connected with the defect chemistry at interface. The basis of this is to take seriously the energetic behaviors of ionic and electronic carriers at the interface contact. Maier [32] developed a comprehensive treatise of conduction at interfaces, which has been successfully confirmed by many experimental evidences including experiments with thin films and composites [33, 34]. Apart from charge transport, the space charge model can also be applied to charge storage[4, 5, 13]. A generalized concept will be developed in the context of this thesis.

2.2 Theory

2.2.1 Weakly disordered ionic conductor / Weakly disordered semiconductor junction

We will start with an abrupt junction of two phases: phase α (weakly disordered ionic conductor with metal ion interstitials $\mathrm{M_i^{\cdot}}$ and metal ion vacancies $\mathrm{V_M'}$ as charge carriers) and phase β (weakly disordered semiconductor with electrons e' and holes $h^{\cdot}$ as charge carriers) (Figure 2.1). The description of point defects is according to Kröger-Vink notation. For the sake of simplicity, here we only consider monovalent defects ($M_i^{\cdot}, V_M', e', h^{\cdot}$) and denote the concentration of each type of defects as c_i, c_v, c_n, and c_h, respectively.

Unlike in bulk phase where the local electroneutrality has to hold, in the boundary region the condition of electroneutrality is replaced by Poisson's equation, which correlates the electrostatic potential Φ established around the boundary and the local charge density ρ

$$\nabla^2 \Phi = -\frac{\rho}{\varepsilon \varepsilon_0} = -\frac{F}{\varepsilon \varepsilon_0} \sum_j Z_j c_j . \tag{2.1}$$

Here ε is the relative permittivity, ε_0 vacuum permittivity, F Faraday constant, and Z_j charge number of species j.

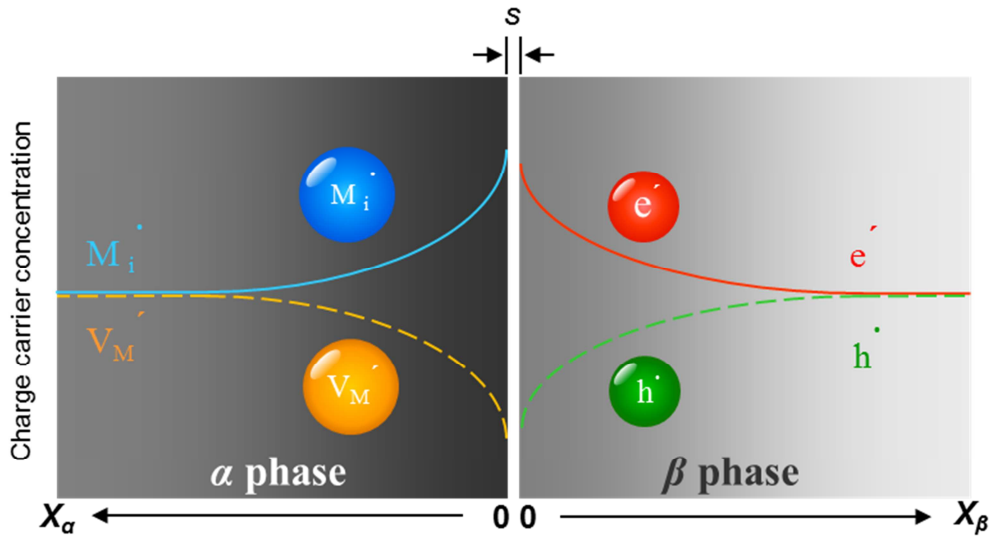

Figure 2.1. Schematic of interfacial storage at a weakly disordered ionic conductor / weakly disordered semiconductor junction.

As illustrated in Figure 2.1, if we only refer to phase α, the space charge region is characterized by an accumulation of $M_i^{\cdot}$ and a depletion of V_M'. The local charge charier concentration is given by a Boltzmann distribution

$$c_j = c_{j\infty}\, exp\left(-\frac{Z_j F(\Phi - \Phi_\infty)}{RT}\right) \tag{2.2}$$

where $c_{j\infty}$ is the bulk concentration of charge carrier j and Φ_∞ the electrostatic potential in the bulk. The symbols R and T have their usual meanings. Substituting (2.2) into (2.1), we can derive the electric field, i.e. $-\frac{d\Phi}{dx}$, for one-dimensional semi-infinite boundary conditions as

$$-\frac{d\Phi}{dx} = -\sqrt{\frac{2RT}{\varepsilon\varepsilon_0}\sum_j\left(c_{j\infty}\exp\left(-\frac{Z_j F(\Phi - \Phi_\infty)}{RT}\right) - c_{j\infty}\right)}. \tag{2.3}$$

(See Appendix I for more details.) Let us first focus on the side of phase α and assume that only two equivalently charge carriers ($M_i^{\cdot}$ and V_M') are relevant. The space charge field will increase one carrier and decrease the counter carrier. In the case that interstitial cations are the major charge carriers, equation (2.3) can be rewritten as

$$-\frac{d\Phi}{dx} = -\sqrt{\frac{2RT}{\varepsilon\varepsilon_0}}\left(\sqrt{c_i(x)} - \sqrt{c_v(x)}\right). \tag{2.4}$$

According to equation (2.1) and (2.4), the total charge along the space charge zone in phase α is determined by the corresponding charge carrier concentration directly at interface ($x_\alpha = 0$)

$$Q_\alpha = \int_0^\infty \rho(x)dx_\alpha = \sqrt{2\varepsilon_\alpha\varepsilon_0 RT}\left(\sqrt{c_i(0)} - \sqrt{c_v(0)}\right). \tag{2.5}$$

The two ionic defects, $M_i^\cdot$ and V_M', are coupled by ionic (Frenkel) disorder equilibrium, established as a consequence of thermal excitation in the crystalline solid. Strictly speaking the perfect (defect-free) solid is only realized at 0K. At T > 0K, the thermal equilibrium concentration of point defects is necessarily greater than zero because of the configuration entropy they introduce. The equilibrium point-defect concentration is the concentration which minimizes the Gibbs free energy of the system [35].

A Frenkel defect, originating from the displacement of an atom from its lattice position to an interstitial site, creating a vacancy on the original site and an interstitial at the new position

$$M_M + V_i \leftrightharpoons M_i^\cdot + V_M'. \tag{2.6}$$

In equation (2.6), M_M and V_i denote the regular structural elements: a cation on its regular site and a vacancy on the interstitial site. This corresponds to an excitation of an ion from a regular energy level to the interstitial level. Such energy levels are more precisely standard electrochemical potentials. The formation free energy of $M_i^\cdot$ and V_M' thus can be viewed as analogy to the band gap between conduction and valance band in semiconductors, as electron/hole pair formation follows an analogous relation [36]. If concentration of $M_i^\cdot$ and V_M' are rather dilute, a mass action law applies with Frenkel constant K_F

$$K_F = c_i(x_\alpha)c_v(x_\alpha). \tag{2.7}$$

Consequently, equation (2.5) can be written as a function of $c_i(0)$ only:

$$Q_\alpha = \sqrt{2\varepsilon_\alpha\varepsilon_0 RT}\left(\sqrt{c_i(0)} - \sqrt{\frac{c_i(0)}{K_F}}\right) \tag{2.8}$$

with the inverse function

$$c_i(0) = \left(\frac{Q_\alpha + \sqrt{{Q_\alpha}^2 + 8\varepsilon_\alpha \varepsilon_0 RT\sqrt{K_F}}}{2\sqrt{2\varepsilon_\alpha \varepsilon_0 RT}} \right)^2 . \tag{2.9}$$

On the other side of the contact (see Figure 2.1), the electronic disorder equilibrium for phase β (semiconductor with electrons and holes) has to be taken into account. As thermal excitation moves some electrons from valence band to conduction band, such excitations create electrons and holes

$$Nil \leftrightharpoons e' + h^{\cdot} . \tag{2.10}$$

Neglecting activity coefficients we can apply an analogous mass action law to equation (2.7)

$$K_B = c_n(x_\beta) c_h(x_\beta) . \tag{2.11}$$

Independent of dopant concentration, the mass action law constant K_B only depends on the intrinsic properties of semiconductors, such as band gap and the effective density of states in conduction and valence band [37]. Therefore, the intrinsic charge carrier concentration, $\sqrt{K_B}$, is a characteristic electrical property of a semiconductor. Similar to the previous derivation for phase α, the total charge along the space charge area in phase β is described as

$$Q_\beta = \int_0^\infty \rho(x) dx_\beta = \sqrt{2\varepsilon_\beta \varepsilon_0 RT}\left(\sqrt{c_h(0)} - \sqrt{c_n(0)}\right) = \sqrt{2\varepsilon_\beta \varepsilon_0 RT}\left(\sqrt{\frac{K_B}{c_n(0)}} - \sqrt{c_n(0)}\right) \tag{2.12}$$

where ε_β is the relative permittivity of phase β.

The ionic and electronic disorder equilibria are assumed to prevail everywhere in phase α and β, respectively. As far as the in-between interface is concerned, the simpler approximation is to assume a charge free zone with linearly electrical potential change (cf. e.g. ref. [38, 39]). Over the charge free zone an electrochemical equilibrium comprising defects in both phases holds

$$M \leftrightharpoons M_i^{\cdot}(x_\alpha = 0) + e'(x_\beta = 0) . \tag{2.13}$$

The physical meaning of (2.13) is that when the component M is accommodated into the lattice it suffices to formulate the incorporation of metal ions into interstitial sites of phase α whereby electrons are injected into the conduction band of phase β. The electrochemical equilibrium follows from the balance of the electrochemical potentials ($\tilde{\mu}_j$) of each species j

$$\tilde{\mu}_M = \tilde{\mu}_{M_i^{\cdot}} + \tilde{\mu}_{e'} \,. \tag{2.14}$$

If the species are dilute, a third mass action law

$$\frac{c_i(0)c_n(0)}{a_M} = K_M \times \exp\left(\frac{-F(\Phi_\alpha(0) - \Phi_\beta(0))}{RT}\right) \tag{2.15}$$

is obtained, where a_M is the activity of M, K_M mass action law constant for M storage, and $(\Phi_\alpha(0) - \Phi_\beta(0)) = \Delta\Phi_0$ the electrical potential drop over the charge free contact zone. (For the readers who are interested in more details, please see Appendix II.) According to Gauss's law, the electrical potential drop is proportional to the product of the total charge and the zone distance (s), i.e. $\Delta\Phi_0 \propto Q_\alpha s$.[1] Note that equation (2.15) involves the defects in both phases ($M_i^{\cdot}$ and e') and thus is recoupled with the other two mass action laws (i.e. (2.7) and (2.11)).

The framework of the interfacial storage at abrupt junctions, consisting of the three mass action laws, conceptually also allows for establishing metal deficiency

$$M + V_M'(x_\alpha = 0) + h^{\cdot}\left(x_\beta = 0\right) \leftrightharpoons \text{Nil.} \tag{2.16}$$

This especially may happen when phase α is a compound in which metal ion vacancies easily form, such as lithium halides. Once M is taken out of the system, V_M' resides on phase α side of the interface while $h^{\cdot}$ forms on phase β side for charge compensation. The stored mass now is therefore "negative".

Due to the global electroneutrality, the total charge stored in phase α and β (notating as Q_α and Q_β) must follow

$$Q = Q_\alpha = -Q_\beta. \tag{2.17}$$

[1] For a parallel plate capacitor, the stored charge (unit: coulomb) = $\varepsilon\varepsilon_0 \frac{plate\ area}{s} \Delta\Phi_0$. So the potential drop $\Delta\Phi_0$ can be replaced by $Q_\alpha s/\varepsilon\varepsilon_0$.

According to (2.8), (2.12), and (2.15), equation (2.17) can be rewritten as

$$\sqrt{2\varepsilon_\alpha\varepsilon_0 RT}\left(\sqrt{c_i(0)}-\sqrt{\frac{K_F}{c_i(0)}}\right)=\sqrt{2\varepsilon_\beta\varepsilon_0 RT}\left(\sqrt{\frac{a_M K_M}{c_i(0)}\,e^{\frac{-F\Delta\Phi_0}{RT}}}-\sqrt{\frac{K_B c_i(0)}{K_M a_M}e^{\frac{F\Delta\Phi_0}{RT}}}\right). \quad (2.18)$$

After rearrangement it yields the following solution:

$$a_M = \left\{\frac{\sqrt{\frac{\varepsilon_\alpha}{\varepsilon_\beta}}\left(\sqrt{c_i(0)}-\sqrt{\frac{K_F}{c_i(0)}}\right)+\sqrt{\left[\sqrt{\frac{\varepsilon_\alpha}{\varepsilon_\beta}}\left(\sqrt{c_i(0)}-\sqrt{\frac{K_F}{c_i(0)}}\right)\right]^2+4\sqrt{K_B}}}{2\sqrt{\frac{K_M}{c_i(0)}\,e^{\frac{-F\Delta\Phi_0}{RT}}}}\right\}^2. \quad (2.19)$$

Substituting (2.5), (2.9), and Gauss's law into (2.19), we can describe the metal activity a_M as an explicit function of storage capacity Q

$$a_M = \frac{\left(Q+\sqrt{Q^2+8\varepsilon_\alpha\varepsilon_0 RT\sqrt{K_F}}\right)^2\left(Q+\sqrt{Q^2+8\varepsilon_\beta\varepsilon_0 RT\sqrt{K_B}}\right)^2}{64K_M\varepsilon_\alpha\varepsilon_\beta(\varepsilon_0 RT)^2}\,e^{\frac{FsQ}{\bar{\varepsilon}\varepsilon_0 RT}} \quad (2.20)$$

where $\bar{\varepsilon}$ is the mean relative permittivity of the two phases.[2] Various cases can be distinguished: (i) For small storage, a_M is rather insensitive with respect to Q. (Note that for small x, $e^x \approx 1+x$.) Here the introduced charge has not yet significantly perturbed the intrinsic disorder. Obviously this range is larger with greater K_F and K_B. (ii) For medium storage, when Q in the prefactor of (2.20) is dominant but the exponential term is still close to unity (i.e. $(\emptyset_\alpha(0)-\emptyset_\beta(0))\approx 0$), a_M is proportional to Q^4. In this range the introduced charge dominates out the intrinsic disorder and the counter defects can be neglected. (iii) For large storage, the exponential term of equation (2.20) becomes dominant and a_M is hence proportional to $e^{\gamma Q}$. ($\gamma=\frac{Fs}{\bar{\varepsilon}\varepsilon_0 RT}$) Owing to significant amounts of $M_i^{\cdot}$ and e' accumulating in the outmost layer of the respective phases, the system exhibits a purely electrostatic capacitor behavior. It is worth mentioning that equation (2.20) is also applicable for deficiency. Since the stored mass is negative and it inversely rises with metal activity, the a_M-Q depedence becomes $a_M \propto |Q|^{-4}$ for medium

[2] Here we follow the relation $\bar{\varepsilon}\frac{\Delta\phi_0}{s}=\varepsilon_\alpha\nabla\phi_\alpha(x_\alpha=0)=\varepsilon_\beta\nabla\phi_\beta(x_\beta=0)$.

storage and still stay $a_M \propto e^{\gamma Q}$ for large storage. The details of different storage regimes will be discussed later.

2.2.2 Weakly disordered ionic conductor / Heavily disordered electronic conductor junction

Another interfacial storage situation is to share accommodation of M between an ionic conductor and a "good electronic conductor", i.e. a metal (that we assume to not alloy with M). This mechanism is of special interest in energy storage applications because metals are extensively used as electrode materials in electrochemical cells. In the language of defect chemistry, we can approximately treat the metal in the limit of a semiconductor with very high K_B [40], i.e "weak metal"[3]. Its Debye length, inversely proportional to the square root of bulk electronic defect concentration, is close or even smaller compared to the lattice size. In view of this, the space charge zone should be represented by a single layer with thickness comparable to the lattice. Another problem we meet is that the high electron concentration in metals actually invalidates the dilute approximation, so it is necessary to consider activity coefficients (non-ideality factor). In this way, the theoretical treatment will become very complicated because the correlation of concentration and activity coefficient is strongly dependent on materials.[41] To avoid the complexities, we only deal with the situation when activity coefficients are negligible (or invariant) and use a single layer approximation to for the space charge zones. Thus the electrons or the holes only locate at the surface of phase β, resulting in a space charge situation displayed in Figure 2.2. Therefore, the total storage in β is simply proportional to the surface charge concentration multiplied by the layer thickness λ_β.

$$Q_\beta = \lambda_\beta F\big(c_h(0) - c_n(0)\big) = \lambda_\beta F\left(\frac{K_B}{c_n(0)} - c_n(0)\right) \tag{2.21}$$

[3] Strictly speaking, it is necessary to apply Fermi-Dirac statistics when calculating the electronic concentration in metal. Then it is required to know the density of states and the corresponding probability of state occupancy. To simplify the mathematical treatment, we assume the "super electronic conductor" being "weak metal", i.e. a semiconductor with close to zero band gap.

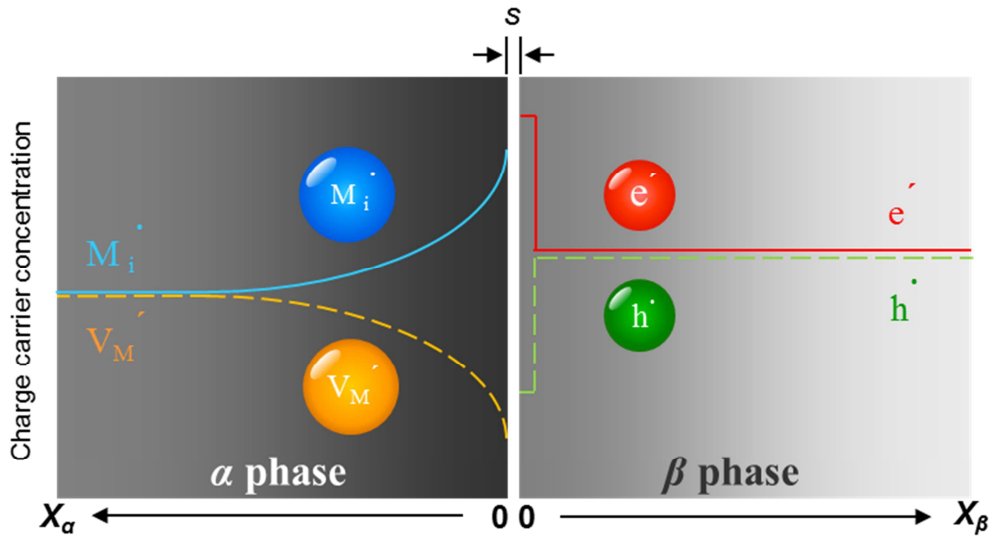

Figure 2.2. Schematic of interfacial storage at a weakly disordered ionic conductor / heavily disordered electronic conductor junction.

Here we assume that the electronic disorder holds even in the small space charge region. Global electroneutrality, i.e. charge conservation, requires, according to (2.8) and (2.21)

$$\sqrt{2\varepsilon_\alpha\varepsilon_0 RT}\left(\sqrt{c_i(0)}-\sqrt{\frac{K_F}{c_i(0)}}\right)=\lambda_\beta F\left(c_n(0)-\frac{K_B}{c_n(0)}\right). \tag{2.22}$$

Substituting (2.15) into (2.22) yields

$$\sqrt{2\varepsilon_\alpha\varepsilon_0 RT}\left(\sqrt{c_i(0)}-\sqrt{\frac{K_F}{c_i(0)}}\right)=\lambda_\beta F\left(\frac{K_M a_M}{c_i(0)}\,e^{\frac{-F\Delta\Phi_0}{RT}}-\frac{K_B c_i(0)}{K_M a_M}\,e^{\frac{F\Delta\Phi_0}{RT}}\right). \tag{2.23}$$

Solving (2.23) for a_M yields

$$a_M=\frac{\sqrt{2\varepsilon_\alpha\varepsilon_0 RT}\left(\sqrt{c_i(0)}-\sqrt{\frac{K_F}{c_i(0)}}\right)+\sqrt{\left[\sqrt{2\varepsilon_\alpha\varepsilon_0 RT}\left(\sqrt{c_i(0)}-\sqrt{\frac{K_F}{c_i(0)}}\right)\right]^2+4\left(\lambda_\beta F\right)^2 K_B}}{\frac{2\lambda_\beta F K_M}{c_i(0)}\,e^{\frac{-F\Delta\Phi_0}{RT}}}. \tag{2.24}$$

With the help of (2.5), (2.9) and Gauss's law, we can eliminate $c_i(0)$ in (2.24). The explicit relation between metal activity and storage capacity thus is

$$a_M = \frac{\left(Q + \sqrt{Q^2 + 8\varepsilon_\alpha \varepsilon_0 RT\sqrt{K_F}}\right)^2 \left(Q + \sqrt{Q^2 + 4\left(\lambda_\beta F\right)^2 K_B}\right)}{16\lambda_\beta F K_M \varepsilon_\alpha \varepsilon_0 RT} e^{\frac{FsQ}{\bar{\varepsilon}\varepsilon_0 RT}}. \qquad (2.25)$$

At small and large storage, equation (2.25) shows same dependence as (2.20), namely $a_M \approx$ constant and $a_M \propto e^{\gamma Q}$. For medium storage, the situation becomes more complicated because it now depends on the intrinsic level of the electronic conductors, i.e. K_B. When K_B is not so large, a relation $a_M \propto Q^{\pm 3}$ is obtained. Here again the plus sign refers to excess and minus sign to deficiency. An extreme case is met when K_B is very large, then second term in the numerator is anyway a constant ($Q + \sqrt{Q^2 + 4\left(\lambda_\beta F\right)^2 K_B} \approx \sqrt{4\left(\lambda_\beta F\right)^2 K_B}$), it yields a different relation $a_M \propto Q^{\pm 2}$.

It is also worth mentioning that the electronic layer thickness λ_β always stays constrained and ionic space charge layer changes its extent on varying storage. The coupling of a continuous function on one side and a step function on the other may lead to a physical misinterpretation in the outmost defect concentrations. Further discussion will be touched upon in section 2.3.2.

2.2.3 Heavily disordered ionic conductor / Weakly disordered semiconductor junction

A similar storage situation occurs when phase α is a superionic conductor while phase β is a semiconductor (Figure 2.3). Superionic conductors – ionic solids in which ions are highly mobile – exhibit anomalous ionic conductivity that even is comparable with liquid electrolyte. Unlike liquid electrolytes in which both cations and anions are mobile, superionic conductors only allow the movement of either cations or anions. A textbook example is AgI. It experiences a phase transition at 147°C from a weak ionic conductor (β-AgI, wurtzite) to a superionic conductor (α-AgI, body-centered cubic) structure, accompanied by a significant increase of Ag^+ conductivity to the order of 1 S/cm [42]. The extremely high conductivity is attributed to 42 available sites for

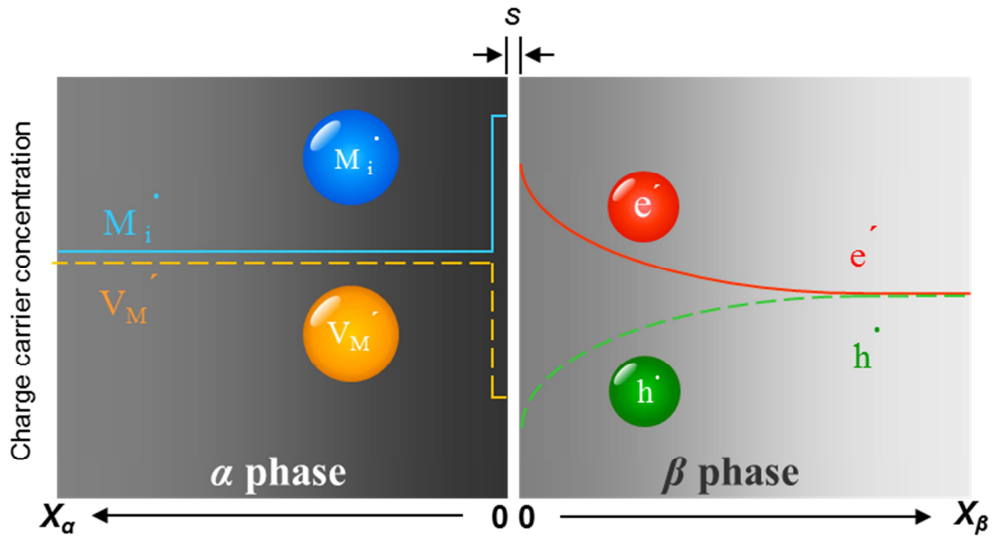

Figure 2.3. Schematic of interfacial storage at a heavily disordered ionic conductor / weakly disordered semiconductor junction.

2 Ag^+ in a cubic unit cell of iodide ions. The large number of available sites therefore causes that Ag^+ moves "freely" within the lattices ("molten sublattice").

An interesting approach to this phenomena of sublattice melting is to consider the columbic interactions between charged defects [43]. At temperatures far below the transition temperature, the defect concentration is small enough to allow us to ignore the interactions. With the rise of temperature, Frenkel disorder equilibrium introduces more point defects, which not only increase the configuration entropy but also the attractive interactions. These two effects respectively refer to different contributions to activity coefficients [44]. Thermodynamically, the electrostatic interaction reduces the formation free energy for Frenkel defects. That is, in the physical view (band structure) of equilibrium, the distance of the energy level of $M_i^{\cdot}$ and $V_M^{\prime}$ is decreased. The level narrowing keeps with the rise of defect concentration driven by thermal excitation. At a specific temperature, the two energy levels eventually coincide, meaning Ag^+ is free to move from a regular site to an interstitial site. This turns an initially weakly defective conductor into a superionic conductor. In spite of neglecting structural effects, the above model is surprisingly in

nice agreements with experimental data. In short, this concept builds a bridge between defect properties in solid and liquid state.

Since point defects in a superionic conductor are concentrated, the space charge zone should be viewed as a single layer. Mathematically the storage situation at the interface of superionic conductor/semiconductor is as isomorphic to the case of ionic conductor / highly disordered electronic conductor contact. So it is straightforward to swap the physical notations in (2.25), resulting in

$$a_M = \frac{\left(Q + \sqrt{Q^2 + 4(\lambda_\alpha F)^2 K_F}\right)\left(Q + \sqrt{Q^2 + 8\varepsilon_\beta \varepsilon_0 RT\sqrt{K_B}}\right)^2}{16\lambda_\alpha F K_M \varepsilon_\beta \varepsilon_0 RT} e^{\frac{FsQ}{\varepsilon\varepsilon_0 RT}}. \qquad (2.26)$$

Equation (2.26) reveals the same dependence of a_M on Q: (i) small storage, $a_M \approx$ constant, (ii) medium storage, $a_M \propto |Q|^{\pm 3}$ or $a_M \propto |Q|^{\pm 2}$, and (iii) large storage, $a_M \propto e^{\gamma Q}$. Opposite to the previous case, the broad space charge layer is now on the side of electronic conductor while the single charge-conducting layer is on the ionic conductor side. Furthermore, although metal ion moves freely in the superionic solid as in liquid, the anion is immobile, which leads to either metal excess or deficiency storage thermodynamically feasible.

2.2.4 Heavily disordered ionic conductor / Heavily disordered electronic conductor junction

The last situation under consideration is that M is stored at the contact of heavily disordered ionic conductor and heavily disordered electronic conductor. Strictly speaking the situation is most complicated because the activity coefficients now enter the game for both sides. To treat the problem more generally and more simply, we still use the same approach that assumes the activity coefficients are negligible or invariant. Due to high charge carrier concentrations in both phases, now both space charge layers are very thin, and no diffusive layers appear (Figure 2.4). The inner layer capacitance is dominant and therefore the system behaves like a parallel-plate electrostatic capacitor.

The stored charge is directly the net charge in the outmost layer of α

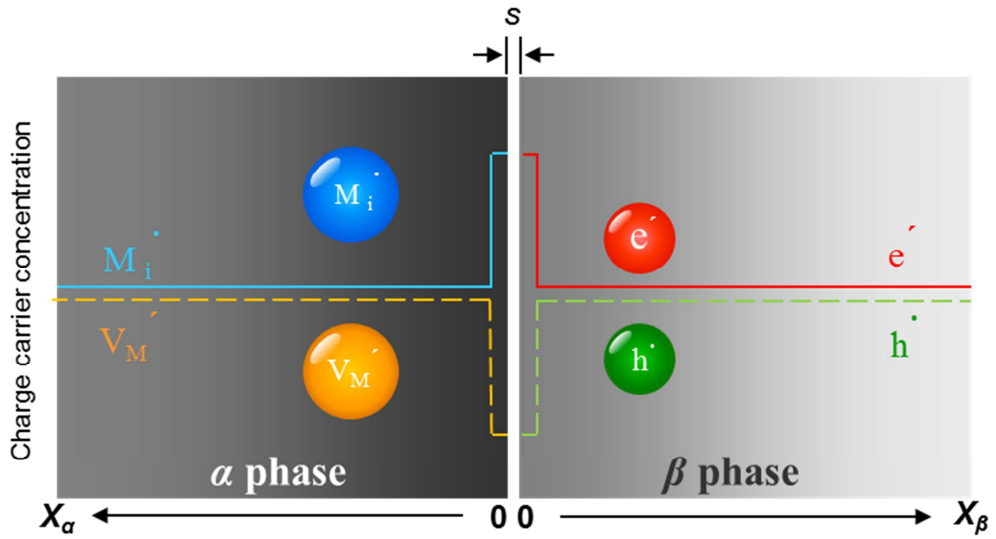

Figure 2.4. Schematic of interfacial storage at a heavily disordered ionic conductor / heavily disordered electronic conductor junction.

$$Q_\alpha = \lambda_\alpha F\big(c_i(0) - c_v(0)\big) = \lambda_\alpha F\left(c_i(0) - \frac{K_F}{c_i(0)}\right) \tag{2.27}$$

where λ_α stands for the layer thickness in α. Algebraic rearrangement leads to

$$c_i(0) = \frac{Q_\alpha + \sqrt{{Q_\alpha}^2 + 4(\lambda_\alpha F)^2 K_F}}{2\lambda_\alpha F} \tag{2.28}$$

The condition of overall electroneutrality (2.17) at the interface still holds, explicitly connecting equation (2.15), (2.21), and (2.27)

$$\lambda_\alpha F\left(c_i(0) - \frac{K_F}{c_i(0)}\right) = \lambda_\beta\left(\frac{K_M a_M}{c_i(0)}\, e^{\frac{-F\Delta\Phi_0}{RT}} - \frac{K_B c_i(0)}{K_M a_M}\, e^{\frac{F\Delta\Phi_0}{RT}}\right) \tag{2.29}$$

Solving equation (2.29) for a_M yields

$$a_M = \frac{\lambda_\alpha\left(c_i(0) - \frac{K_F}{c_i(0)}\right) + \sqrt{\left[\lambda_\alpha\left(c_i(0) - \frac{K_F}{c_i(0)}\right)\right]^2 + 4{\lambda_\beta}^2 K_B}}{\frac{2\lambda_\beta K_M}{c_i(0)}\, e^{\frac{-F\Delta\Phi_0}{RT}}} \tag{2.30}$$

After adopting (2.27), (2.28) to eliminate $c_i(0)$ and using Gauss's law in equation (2.30), the desired a_M vs. Q relation is obtained

$$a_M = \frac{\left(Q + \sqrt{Q^2 + 4(\lambda_\alpha F)^2 K_F}\right)\left(Q + \sqrt{Q^2 + 4(\lambda_\beta F)^2 K_B}\right)}{4\lambda_\alpha \lambda_\beta K_M F^2} \, e^{\frac{FsQ}{\varepsilon\varepsilon_0 RT}}. \tag{2.31}$$

The $a_M - Q$ dependence for small and large storage stay as same as in previous situations. For medium storage, the n value of the relation $a_M \propto |Q|^{\pm n}$ varies from 2 to 0, depending on the intrinsically disorder level. The characteristic value 0 refers to the extreme case with both very high K_F and K_B, e.g. superionic conductor and metal. As the two mass action constants are so high, the two terms in the numerator of equation (2.31) always maintain constants. This implicitly suggests that the intrinsic concentrations on both sides are too high to be altered by the added charges. It is straightforward to follow that n value of 1 is obtained for either very high K_F or K_B and 2 is given for not very high K_F or K_B.

Table 2.1 summarizes the expressions of a_M as a function of Q for different junctions. To investigate these correlations, electrochemical methods, such as coulometric titration techniques, are applied. As a pure metal M is usually selected as reference electrode, a_M can be determined by measuring the chemical potential difference between the working and the reference electrode, c.f. Nernst equation

$$E \ (vs.\, M/M^+) = -\frac{RT}{F}\ln(a_M) \tag{2.32}$$

with $a_M(pure\ M) = 1$. The material specificity enters via the various mass action constants and the dielectric constants in Table 2.1. In particular, the three mass action law constants (K_F, K_B, K_M) play key roles for the charge carrier concentrations at the interfaces. The details of defect chemistry for interfacial storage will be extensively discussed in the next section.

Table 2.1. Summary of metal activity dependence on capacity for different interfaces (neglect of activity coefficients)

Semiconductor / Ionic conductor	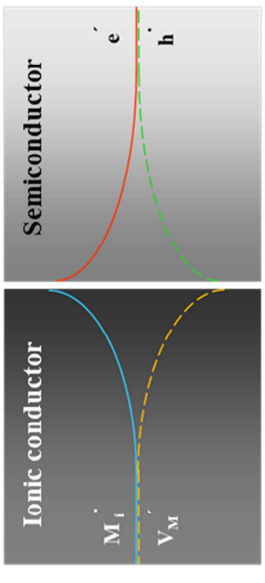	$a_M = \frac{\left(Q+\sqrt{Q^2+8\varepsilon_\alpha\varepsilon_0 RT\sqrt{K_F}}\right)^2\left(Q+\sqrt{Q^2+8\varepsilon_\beta\varepsilon_0 RT\sqrt{K_B}}\right)^2}{64K_M\varepsilon_\alpha\varepsilon_\beta(\varepsilon_0 RT)^2}\,e^{\frac{FsQ}{\bar{\varepsilon}\varepsilon_0 RT}}$
(Weak) metal / Ionic conductor	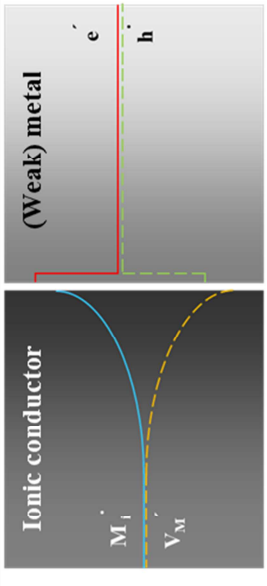	$a_M = \frac{\left(Q+\sqrt{Q^2+8\varepsilon_\alpha\varepsilon_0 RT\sqrt{K_F}}\right)^2\left(Q+\sqrt{Q^2+4(\lambda_\beta F)^2K_B}\right)}{16\lambda_\beta FK_M\varepsilon_\alpha\varepsilon_0 RT}\,e^{\frac{FsQ}{\bar{\varepsilon}\varepsilon_0 RT}}$
Semiconductor / Superionic conductor	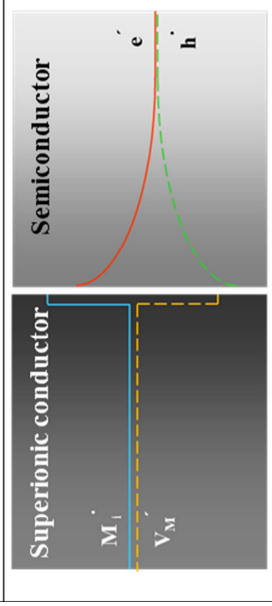	$a_M = \frac{\left(Q+\sqrt{Q^2+4(\lambda_\alpha F)^2K_F}\right)\left(Q+\sqrt{Q^2+8\varepsilon_\beta\varepsilon_0 RT\sqrt{K_B}}\right)^2}{16\lambda_\alpha FK_M\varepsilon_\beta\varepsilon_0 RT}\,e^{\frac{FsQ}{\bar{\varepsilon}\varepsilon_0 RT}}$
(Weak) metal / Superionic conductor	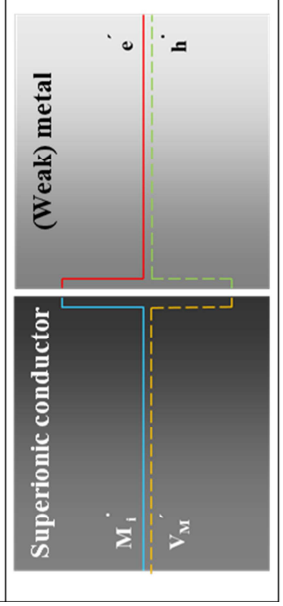	$a_M = \frac{\left(Q+\sqrt{Q^2+4(\lambda_\alpha F)^2K_F}\right)\left(Q+\sqrt{Q^2+4(\lambda_\beta F)^2K_B}\right)}{4\lambda_\alpha\lambda_\beta K_M F^2}\,e^{\frac{FsQ}{\bar{\varepsilon}\varepsilon_0 RT}}$

2.3 Results

2.3.1 Weakly disordered ionic conductor/Weakly disordered electronic conductor junction

Figure 2.5 shows the cell voltage versus capacity (M content) for interfacial storage at an ionic conductor/semiconductor junction. Like usual notation used in non-stoichiometry, positive Q refers to excess and negative Q refers to deficiency. The intrinsic point, i.e. the zero storage point, corresponds to an activity ($\sqrt{K_F K_B}/K_M$) that is only determined by the three mass action law constants. The mathematical expression is analogous to that of the zero point for bulk storage [5], showing a satisfactory correspondence between heterogeneous storage and homogeneous storage. Note that these three constants for interfacial storage are adopted from different phases while for bulk storage they are from the same phase.

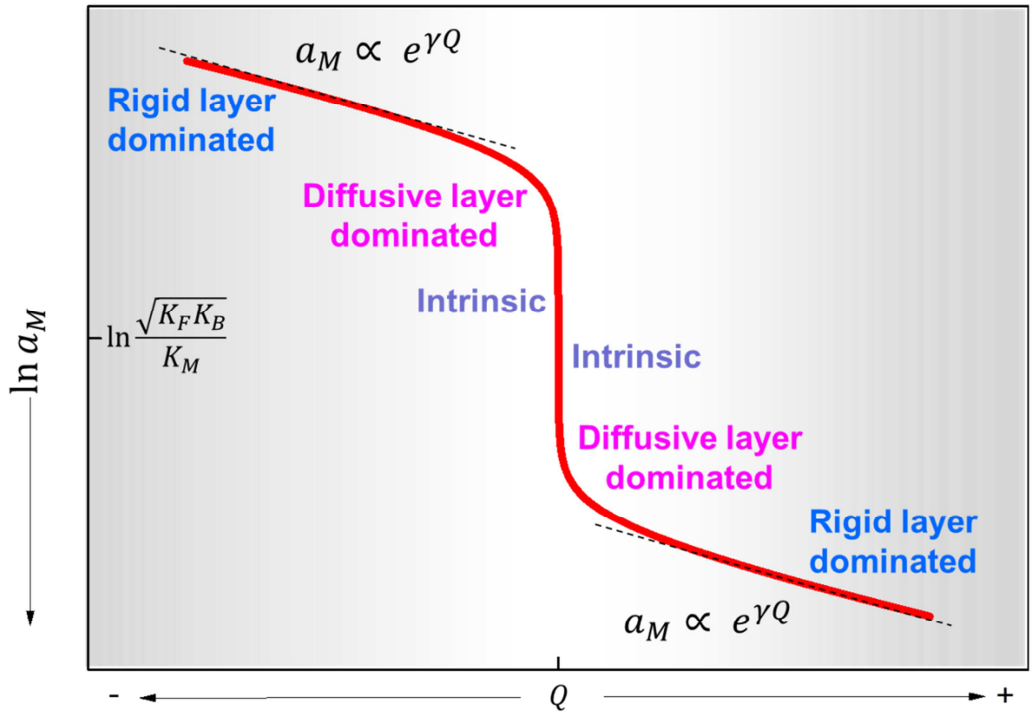

Figure 2.5. The metal activity versus non-stoichiometry for a job-sharing mechanism. Apart from the stoichiometric point, positive Q refers to excess ($M_i^{\cdot}/e'$) and negative to deficiency ($V_M'/h^{\cdot}$). The three different storage modes are dependent on the interfacial defect chemistry.

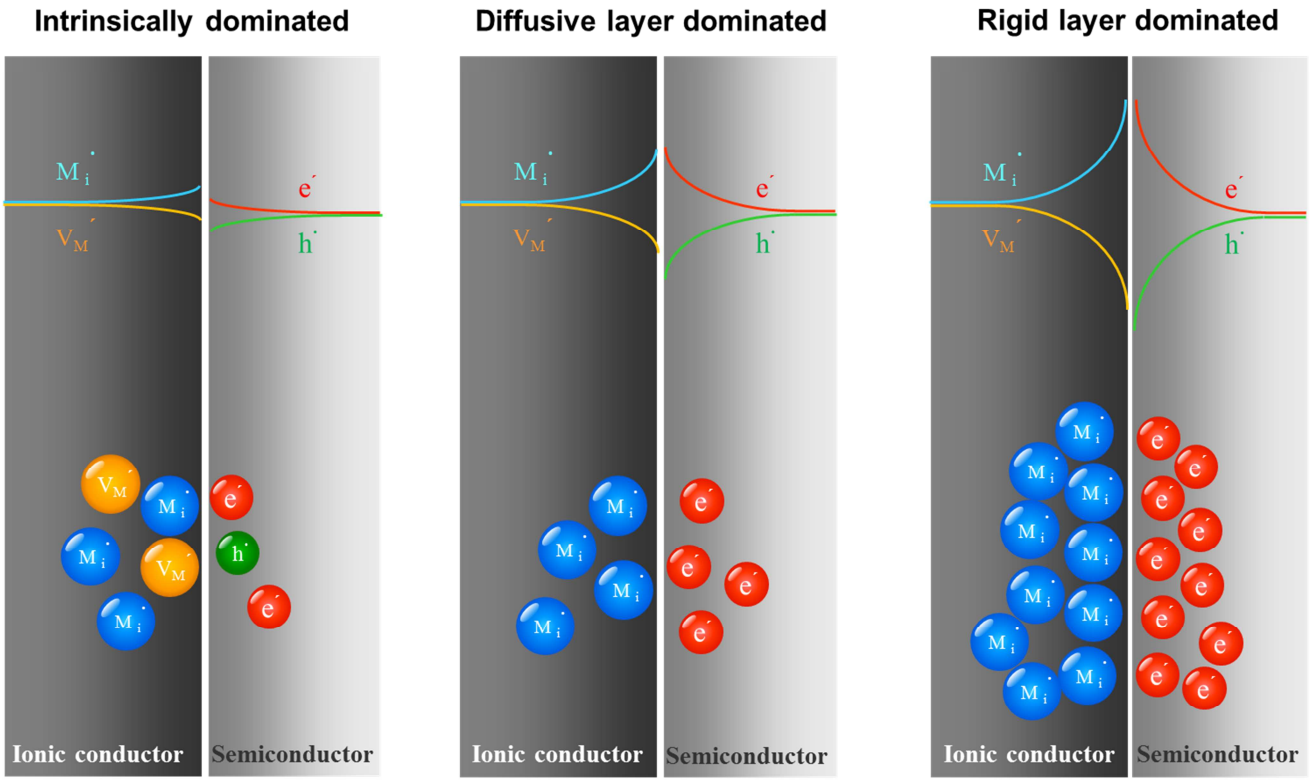

Figure 2.6. Schematic of different storage modes for excess. (a) Intrinsically dominated. All four types of defects are non-negligible. Even though the total number on the left is more than on the right, the net charges on both sides should be equal. (b) Diffusive-layer dominated. The stored charge is great enough to allow neglect of the counter defects. On both sides the charges distribute in the diffuse layers and $\Delta\Phi_0$ is still negligible. (c) Rigid-layer dominated. The charges accumulate in the rigid layer and yields substantial $\Delta\Phi_0$. Note that the Debye length, determined by the bulk defect concentration, does not change.

Similar to bulk storage, the equilibrium potential vs. capacity exhibits a s-shape curve. As introduced in section 2.2, the total charge in the space charge zone is directly correlated with the defect concentrations in the outmost layers. Here we first consider the situation of the ionic conductor/semiconductor interface. The cartoon in Figure 2.6 illustrates the defect chemistry at the contact.

For given mass action law constants and the physical parameters in Table 2.2, Figure 2.7 displays the metal activity dependence on capacity, defect chemistry at interface, and the

electrostatic potential drop over the interface. Three different storage modes will be discussed as follows.

Table 2.2. Physical parameters for the calculation shown in Figure 2.7

$K_F \,/\, \frac{mol^2}{m^6}$	$K_M \,/\, \frac{mol^2}{m^6}$	$K_B \,/\, \frac{mol^2}{m^6}$	$R \,/\, \frac{kg\, m^2}{s^2\, K\, mol}$	$T \,/\, K$	$F \,/\, \frac{sA}{mol}$
10^{-3}	10^{-6}	10^{-9}	8.314	298	96500
$s \,/\, m$	ε_α	ε_β	$\bar{\varepsilon}$	$\varepsilon_0 \,/\, \frac{s^4 A^2}{m^3 kg}$	
3×10^{-10}	10	10	10	8.9×10^{-12}	

2.3.1.1 Intrinsically dominated storage

The total storage in phase α is determined by the integral of $(c_i(x) - c_v(x))$ while in phase β, by the integral of $(c_n(x) - c_h(x))$. That is, the stored charge is solely dependent on the net defect concentration instead of the absolute concentration of each defect. Note that the different defects in the different phases may be very different in concentrations, depending on K_F and K_B. The storage regime is called intrinsically dominated storage where $(c_i(x),\ c_v(x))$ in phase α and $(c_n(x),\ c_h(x))$ in phase β are comparable, respectively. As mentioned in previous section, the interfacial storage mechanism not only allows establishing metal excess but also deficiency. The former consists of $(M_i^{\cdot}, e')$ and the latter consists of $(V_M', h^{\cdot})$. In both situations it is necessary to consider the four charge carriers in this regime.

For instance, Figure 2.7(b) illustrates that $(c_n(0),\ c_h(0))$, i.e. the concentrations of e^- and h^+ in the outmost layer of phase β, are on the same order of magnitude and markedly higher than $(c_i(0),\ c_v(0))$. Note that $c_n(0) \approx c_h(0) \gg c_i(0) \approx c_v(0)$. Nevertheless, $(\sqrt{c_n(0)} - \sqrt{c_h(0)})$ must be equal to $(\sqrt{c_i(0)} - \sqrt{c_v(0)})$, if we assume the same dielectric constant for both phases. (cf. equation (2.5) and (2.12).) Due to global electroneutrality, for excess it should hold that $c_n(0) > c_h(0),\ c_i(0) > c_v(0)$ while for deficiency $c_h(0) > c_n(0),\ c_v(0) > c_i(0)$.

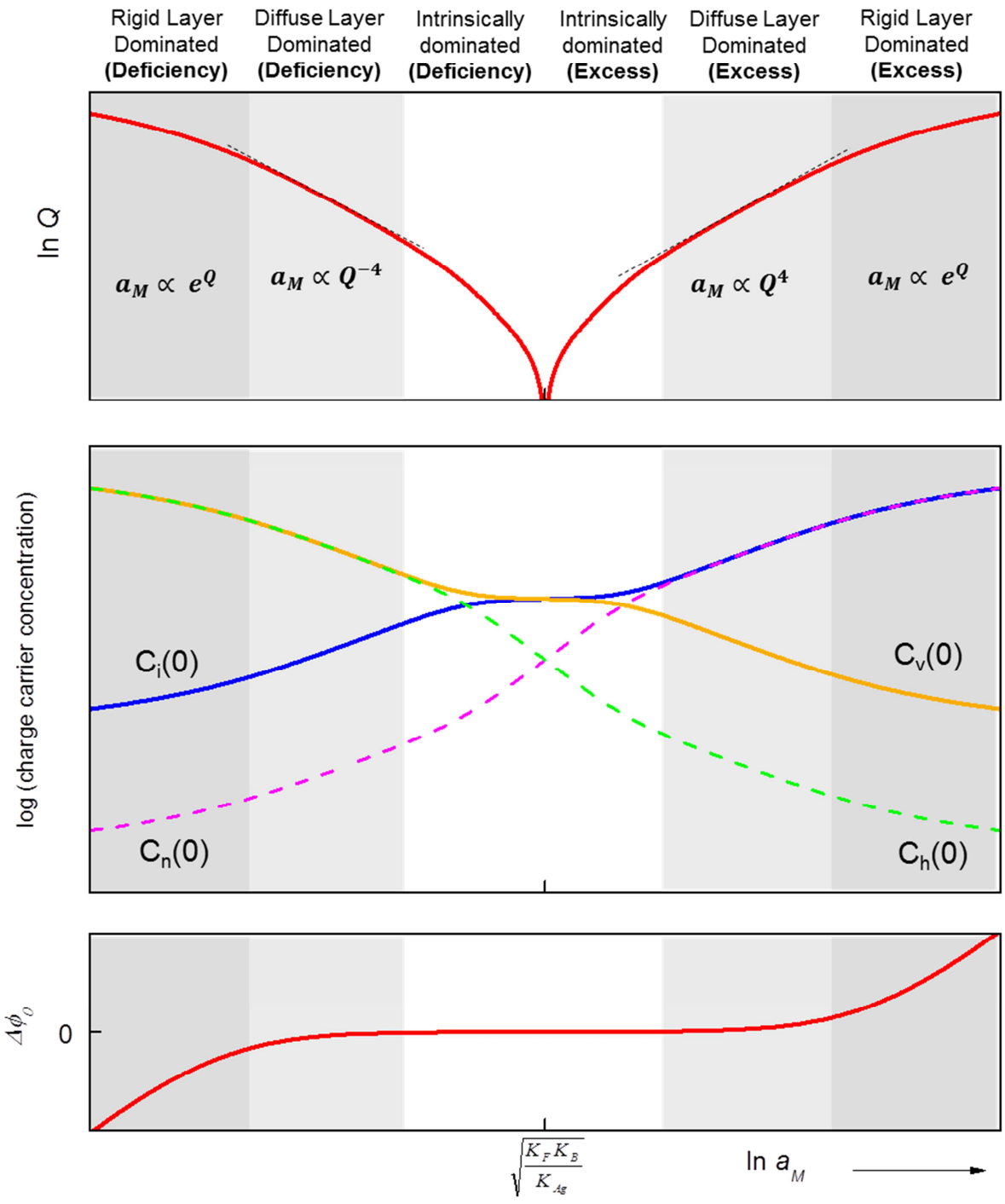

Figure 2.7. Interfacial defect chemistry of ionic conductor/semiconductor contact. (a) Dependence of capacity on metal activity. E is linear with $Q^{\pm 4}$ in the diffuse-layer dominated regime while the curve bends in the rigid layer dominated regime, owing to the contribution from $\Delta\Phi_0$. (b) Defect concentrations versus metal activity. (c) The electrostatic potential drop over the interface. It becomes perceptible in the rigid layer dominated regime.

2.3.1.2 Diffusive-layer dominated storage

With the storage increases, the majority defects become predominant and the corresponding counter defects hence negligible. If we take excess as example, $M_i^{\cdot}$ in phase α and e' in phase β, both increase with storage and eventually turn to be dominant. Meanwhile, V_M' and $h^{\cdot}$ in the respective phase become minor defects. This leads to typical Gouy-Chapman profiles in both phases. The width of the space charge layer varies from atomic scale to several nanometers, depending on material, temperature, impurity, etc[32]. Because two diffusive layers are respectively formed by majority defects ($M_i^{\cdot}$, e'), the storage mode is called diffusive-layer dominated storage. In this storage mode, the stored charge is mostly contributed by the majority defect, that is, Q is approximately proportional to the integral of $c_i(x)$ or $c_n(x)$. Consequently, equation (2.5) and (2.12) can be rewritten as

$$Q_\alpha = \int_0^\infty \rho(x)dx_\alpha = \sqrt{2\varepsilon_\alpha\varepsilon_0 RTc_i(0)} \tag{2.33}$$

$$Q_\beta = \int_0^\infty \rho(x)dx_\beta = \sqrt{2\varepsilon_\beta\varepsilon_0 RTc_n(0)}. \tag{2.34}$$

Substituting (2.33) and (2.34) into (2.15) and neglecting the exponential term of (2.15), we can derive a correlation that a_M is proportional to Q^4, exactly as we introduced in section 2.1. By plotting $\ln Q$ vs. $\ln a_M$, Figure 2.7(a) clearly shows a linearity relation. Based on equation (2.32), the power order can be calculated, from the slope, to be 4. A similar derivation applies for deficiency if we treat (V_M' , $h^{\cdot}$) as majority defects. Instead of 4, one should note that the power is -4 for deficiency, simply because the removal of metal leads to the decrease of metal activity.

According to Boltzmann distribution, defect concentration and electrical potential depend on each other, implying that space charge potentials build up in phase α and β, respectively. However, the potential drop between the outmost layers of the two phases has not been considered so far.

The potential drop ($\Delta\Phi_0 = (\Phi_\alpha(0) - \Phi_\beta(0))$ builds up on charge accumulation at the interface. At not so high storage, the potential drop is negligible, i.e. $\Delta\Phi_0 \approx 0$ in equation (2.15). This actually reduces equation (2.15) to a typical mass action law

$$\frac{c_i(0)c_n(0)}{a_M} = K_M \tag{2.35}$$

and the system can be regarded as a pure chemical capacitor.

2.3.1.3 Rigid-layer dominated storage

The potential drop ($\Delta\Phi_0$) becomes perceptible when a large amount of $M_i^{\cdot}$ and e' gather in adjacent lattice planes of phases α and β. In this case, the system behaves like an electrostatic capacitor, and the stored capacity is mostly contributed by the charges at the boundary ($x = 0$). A similar phenomenon is expected for deficiency. Since most charges accumulate in the rigid layer of the interface, the storage mode is called rigid-layer dominated storage. In this mode we need to take seriously the exponential term in (2.15), which leads to the significance of the exponential term in the analytical solution (2.20). Mathematically, at high Q the exponential function dominates the prefactor in (2.20), so we can obtain

$$a_M \propto e^{\gamma Q} \tag{2.36}$$

where $\gamma = \frac{Fs}{\bar{\varepsilon}\varepsilon_0 RT}$. Substituting equation (2.36) into equation (2.32), one can derive that the equilibrium potential is proportional to the capacity, a characteristic relation for electrostatic capacitors. Furthermore, it is worth mentioning that the matter stored in this interfacial mechanism is at the solid/solid interface while for conventional supercapacitors the matter is stored at a solid/liquid interface.

Figure 2.7(c) shows how $\Delta\Phi_0$ varies with $\ln a_M$. As expected, $\Delta\Phi_0$ is negligible in the intrinsically and diffusive-layer dominated storage domains. It dramatically increases when entering the rigid-layer dominated regime. Compared with the defect chemical picture in Figure 2.7(b), the rise of $\Delta\Phi_0$ is due to significant amount of charges accumulating in the outmost layer. (Note the y-axis is the logarithm of defect concentration.) As $\Delta\Phi_0$ refers to the difference of the two phase (outmost layers), it is positive for excess while negative for deficiency in Figure 2.7(c).

Finally, the readers should note that the exponential function in (2.15) essentially leads to the interfacial storage being distinct from bulk storage. In the case of bulk storage, $\ln Q$ is always linear with $\ln a_M$ (cf. reference [5]). However, $\ln Q$ vs. $\ln a_M$ in Figure 2.7(a) is bent in the rigid-layer dominated storage regime, simply because the exponential function in (2.15) enters the game.

2.3.1.4 Quantitative discussion of parameter variations

The thermodynamics of interfacial storage, as illustrated in Figure 2.7, is dependent on the properties of the constituting phases α and β. To apply the model to different materials, it is of interest to evaluate how the material parameters influence the storage and defect chemistry.

Table 2.2 lists the parameters used in Figure 2.7. Among the listed parameters, the dielectric constants and mass action constants are directly related to phase α and β. In particular, K_F and K_B may vary, from material to material, up to several orders different. In this section, we will demonstrate the influence of K_F and K_B on interfacial storage.

The electronic conductivity of phase β monotonically increases with the concentration of electronic defects[40], so the variation of K_B directly influences its electronic conductivity. Figure 2.8 shows the voltage-capacity curve when the K_B value increases by five orders of magnitude, which in practice can be achieved by choosing better electron conductors or raising the temperature. The corresponding parameters are given in Table 2.3. Although it still exhibits a typical S-shape characteristic, the potential jump at the stoichiometric point for the high K_B curve is smaller than for the low K_B one.

Compared with Figure 2.7, the intrinsically dominated regime for high K_B case is narrower (Figure 2.8a). With the increase of K_B, the intrinsic defect concentrations rise and are closer to the intrinsic ionic defect concentration, c.f. Figure 2.7b and 2.8b. Moreover, high K_B also leads to the shrinking of diffusive region because the Debye length of space charge region is inversely proportional to the square root of the defect concentration in bulk. The smaller intrinsic and diffusive storage regions lead to the dominance of the rigid layer mode. That is, the potential

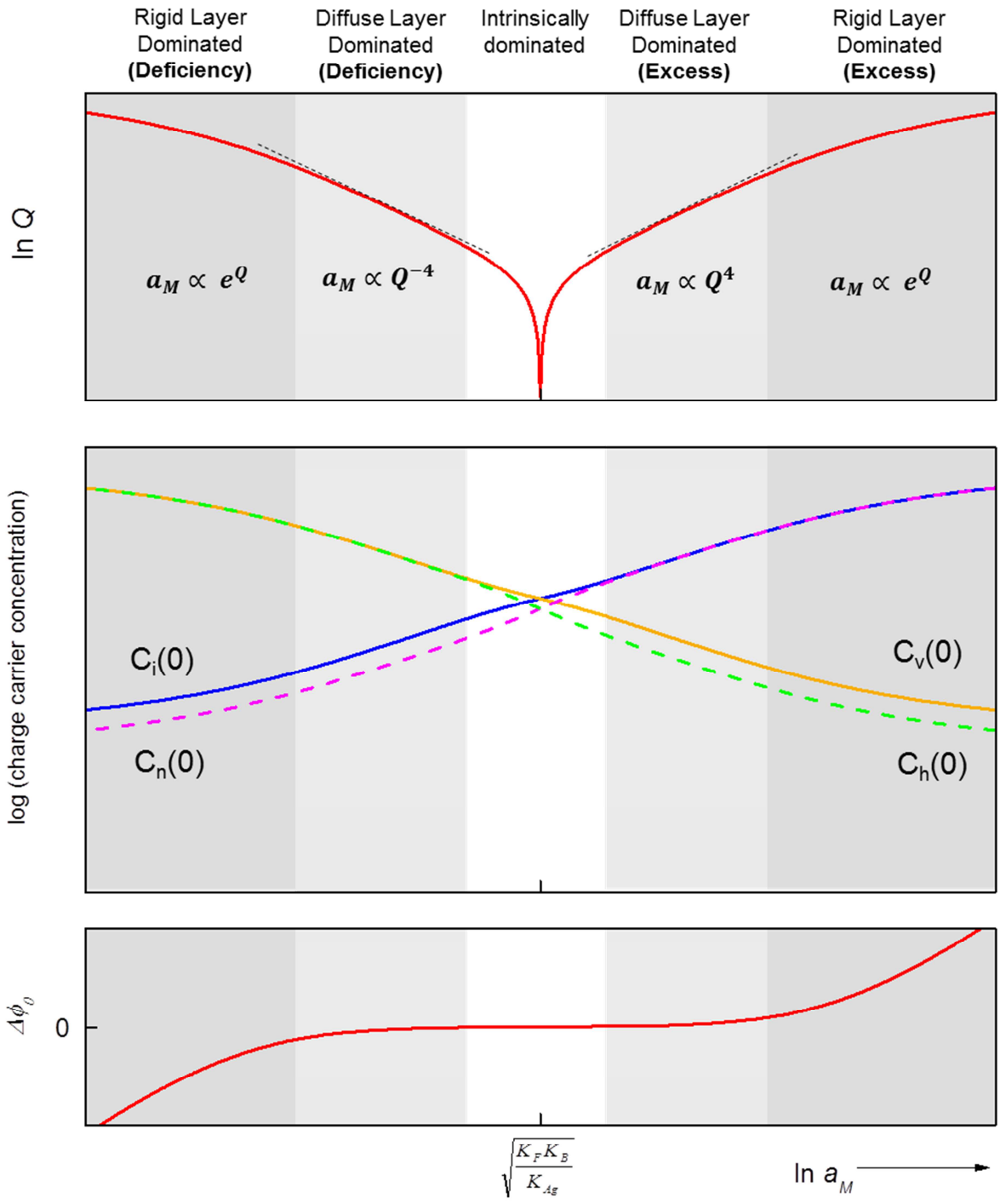

Figure 2.8. Interfacial defect chemistry of ionic conductor/semiconductor contact with higher K_B than Figure 2.7. (a) Dependence of capacity on metal activity. (b) Defect concentrations versus metal activity. (c) The electrostatic potential drop over the interface. The corresponding parameters are given in Table 2.3. Compared with Figure 2.7, the intrinsically dominated regime is narrower with K_B increases.

Table 2.3. Physical parameters for the calculation shown in Figure 2.8

$K_F \,/\, \frac{mol^2}{m^6}$	$K_M \,/\, \frac{mol^2}{m^6}$	$K_B \,/\, \frac{mol^2}{m^6}$	$R \,/\, \frac{kg\,m^2}{s^2\,K\,mol}$	$T \,/\, K$	$F \,/\, \frac{sA}{mol}$
10^{-3}	10^{-6}	10^{-4}	8.314	298	96500
$s \,/\, m$	ε_α	ε_β	$\bar{\varepsilon}$	$\varepsilon_0 \,/\, \frac{s^4A^2}{m^3kg}$	
3×10^{-10}	10	10	10	8.9×10^{-12}	

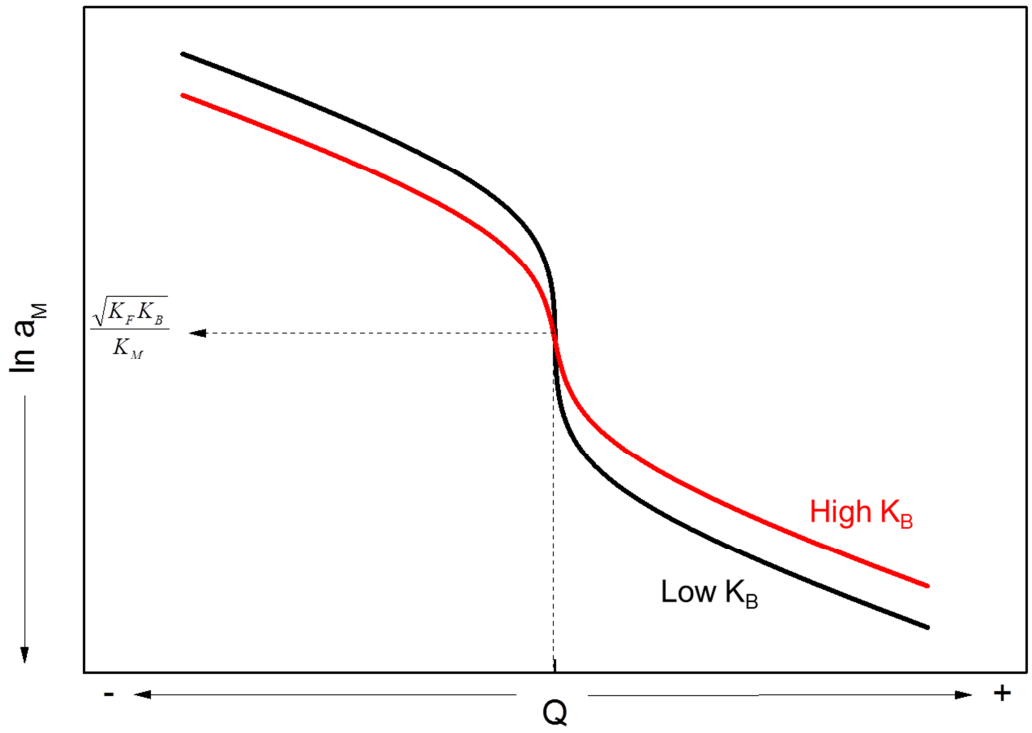

Figure 2.9. The metal activity versus non-stoichiometry with different K_B. The potential jump around the stoichiometric point reduces with K_B increases.

drop over the interface becomes non-negligible with smaller amount of accumulated charge, as shown in Figure 2.8c. Note that the increase of K_B does not only enhance the transport, i.e. leading to higher conductivity, but also guarantees a thermodynamically favorable storage. For given stored charges the potential range for high K_B case is smaller (c.f. Figure 2.9). In the

electrochemical applications, such as battery and supercapacitor, the working potential is usually limited by the decomposition of electrolyte. Therefore, the curve with high K_B can have a higher storage density in a given potential range. An extreme case is when K_F and K_B both approach very large numbers. One can imagine the potential jump around the stoichiometric point will turn to be zero and the curve hence becomes a straight line. This case, which happens for superionic conductor/metal contact, will be discussed later.

2.3.2 Weakly disordered ionic conductor / Heavily disordered electronic conductor junction

Let's move to the case in which the semiconductor is replaced by a good electronic conductor, e.g. metal. Although the corresponding voltage-capacity curve still suggests the S-shape characteristic, the defect chemistry picture is different (Figure 2.10). In particular, one may notice for large storage $c_i(0) > c_n(0)$, which is obviously unreasonable because the space charge layer of phase α is wider than of phase β.

The discrepency is illustrated in Figure 2.11. Due to the global charge concervation, the total charge on the left side should be equal to the right side. The screening lengths, however, are very different. Here we take the monolayer approximation for the metal, i.e. a step function profile. The electron concentration $c_n(x_\beta = 0)$ is hence equal to $c_n\left(x_\beta = \frac{\lambda_\beta}{2}\right)$, where λ_β is the layer thickness. On the other side of the ionic conductor, the concentration is a Gouy-Chapman profile. The continuous function cannot strictly apply if we take the atomic structure into account. Although the electrochemical equilibrium need to consider the outmost surface concentration, the effective ionic defect concentration should refer to the position at r, i.e. $c_i(x_\alpha = r)$, rather than $c_i(x_\alpha = 0)$. In Figure 2.11 the situation $c_i(x_\alpha = 0) > c_n(x_\beta = 0) > c_i(x_\alpha = r)$ reaveals the realistic case of ionic conductor/metal contact. An improvement here would require a discretization calculation, c.f. [39]. The detailed discussion is out of the scope of the present work. Finally, it is worth mentioning that the contact of superionic conductor/semiconductor is conceptually similar to the case described above as long as we swap the results of the ionic and the electronic defect species.

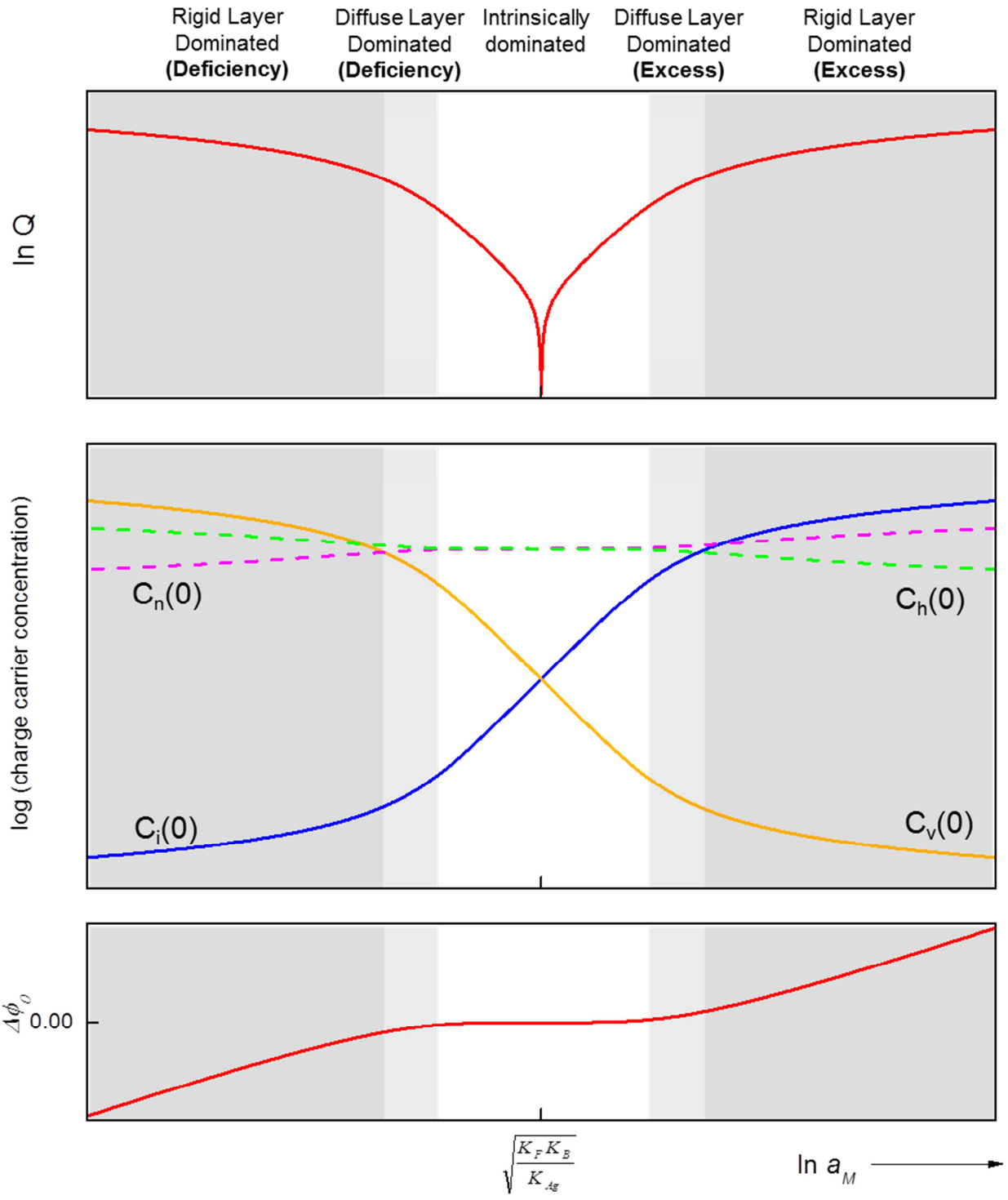

Figure 2.10. Interfacial defect chemistry of ionic conductor/metal contact. The input parameters are listed in Table 2.4.

Table 2.4. Physical parameters for the calculation shown in Figure 2.10

$K_F \,/\, \frac{mole^2}{m^6}$	$K_M \,/\, \frac{mole^2}{m^6}$	$K_B \,/\, \frac{mole^2}{m^6}$	$R \,/\, \frac{kg\, m^2}{s^2\, K\, mole}$	$T \,/\, K$	$F \,/\, \frac{sA}{mole}$
10^{-4}	10^{1}	10^{6}	8.314	298	96500
$s \,/\, m$	λ_β / m	ε_α	ε_β	$\bar{\varepsilon}$	$\varepsilon_0 \,/\, \frac{s^4 A^2}{m^3 kg}$
3×10^{-10}	3×10^{-10}	10	10^{-10}	10	8.9×10^{-12}

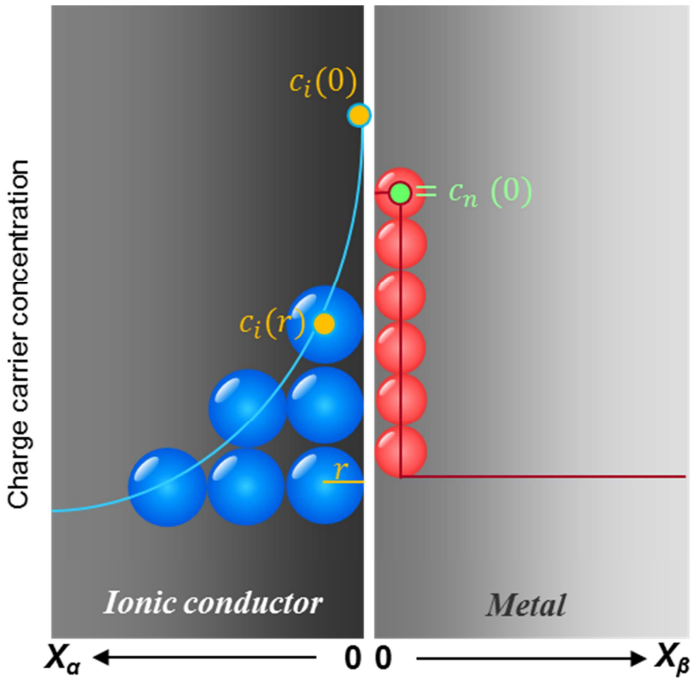

Figure 2.11 Schematic of the simplified model of an ionic conductor/metal contact. The radius of ion denotes as *r*.

2.3.3 Heavily disordered ionic conductor / Heavily disordered electronic conductor junction

The last situation is the contact of a heavily disordered ionic conductor and a heavily disordered electronic conductor, e.g. superionic conductor and metal. The disappearance of diffusive layers

forces us to use the single layer model for both sides. For the sake of simplicity, the saturation effects and interactions are ignored here.

As introduced earlier in section 2.3.1.4, the shape of the titration curve (i.e. $\ln a_M$ vs. Q) is actually determined by the value of K_F and K_B. An extreme case is reached when both K_F and K_B are huge numbers, which refers to a straight line in Figure 2.13. Such high K_F and K_B thus leads to the relation $a_M \propto Q^0 e^{\gamma Q}$, indicating that the intrinsic concentrations are difficult to be altered by the titration. Note that the maximal K_F (or K_B) refers to the total available sites (or states).

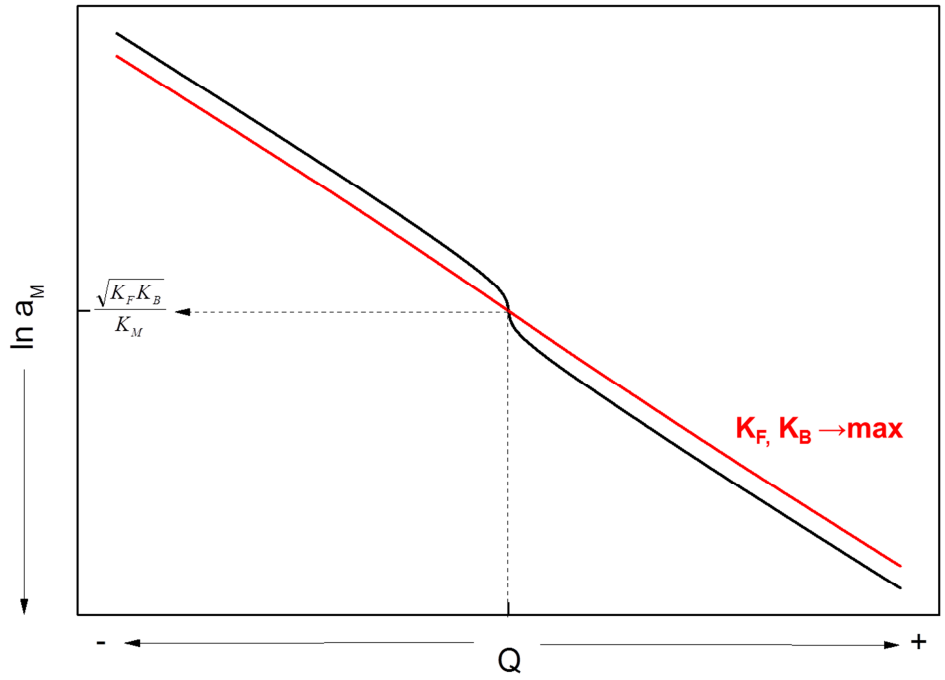

Figure 2.12. The metal activity versus non-stoichiometry for superionic conductor/metal contact. .

2.4 Discussion

The electrochemical devices, such as batteries and supercapacitors, are vital for energy storage research. For batteries the nonstoichiometric variations mostly occur in bulk phase while they suffer from the sluggish mass transport rate. Since the mass transport is the rate-determining step

for storing mass (e.g. chemical diffusivity of Li in Li-battery electrode is on the order of 10^{-10} cm^2/s), enormous studies have tried to confine the size of the electrode materials to enhance the rate performance. (The diffusion time is inversely proportional to the square of diffusion length.) On the other hand supercapacitors, storing charges at the electrode/electrolyte interface by applying an electric filed, exhibit fast charge/discharge rate but the nonstoichiometry of the electrode is invariant. That is, the electrodes only serve as electron source (or sink), but the stoichiometric variations, involving both ions and electrons, do not change.

In the study our job-sharing mechanism apparently builds a bridge between these two classic concepts. Early work by Kimura *et al.*[45] reported that at the AgBr/graphite interface the double-laer capacitance is a function of equilibrium potential (vs. Ag/Ag^+). The tendency of the potential-capacitance curve (a S-shape characteristic if we replot $\ln a_M$ vs. Q) is in agreement with our model of ionic conductor/metal case. This is realized because AgBr is a typical Frenkel disorder conductor and graphite is a good electronic conductor. However, systematic studies bridging the theoretical treatment and experiment are still lacking. In the next two chapters we will quantitatively demonstrate that the job-sharing mechanism is able to store metal (Li and Ag) in a composite materials consisting of two phases that both cannot store the metal individually.

3

Experimental Evidence I:
Lithium Storage and Removal at LiF/Ni Interface

As chapter 2 has comprehensively introduced the theoretical background of interfacial storage, in this chapter the experimentally investigation of the non-stoichiometry of Li at heterogeneous LiF/Ni junctions will be described. The model system is selected because neither LiF nor Ni could store Li by itself. The LiF/Ni nanocomposites are synthesized via electrochemical method. The dependence of equilibrium potential and storage capacity shows that the results are consistent with the developed model. Moreover, the stoichiometric variation covers Li excess and deficiency, indicating the possibility of both reversible Li addition and removal at the heterogeneous junctions.

The interfacial effect turns out to be particularly vital for nanocrystalline electroactive materials which have been widely used in batteries. Since the crystalline materials consist of bulk and boundary zone, it is fundamentally important to unify conventional bulk storage and the interfacial storage. The chapter allows for a generalized storage picture of electrode materials.

3.1 Introduction

Li-based battery is the core technology for portable devices and electric vehicles. As far as higher capacity and power density are concerned, the study of storage mechanisms has aroused great attention. The thermodynamics of electrochemical lithium storage is connected with the

defect chemistry of solids [5] (cf. Chap. 1). The dissolution of lithium in single phases, usually called intercalation, is a most common storage mechanism. The storage of lithium, comprising storage of two charge carriers (Li^+ and e^-), is located in the lattice of host materials. The second mechanism involves the transition between two phases, such as $LiFePO_4/FePO_4$ [46]. As long as Li storage involves variation of phase fraction rather than variation of stoichiometry, a voltage plateau is characteristic of this mechanism. Another similar but more complicated mechanism is the conversion reaction. This mechanism involves at least three phases and is met, for instance, when a transition metal oxide is converted to the nanocrystalline composite of Li_2O and the metal [15]. Besides the voltage plateau like for two phase systems, another characteristic of this mechanism is the additional capacity obtained after the conversion reactions has completed. The extra storage is not only substantial but it can be partly reversed when charged at high current. The details of such unusual finding are still under debate. Reasonable interpretations include *in-situ* polymer/gel film growth during lithiation [47] or generation of Li_2O and LiH [48]. Both interpretations involving the decomposition of liquid electrolyte seem plausible but have difficulties in explaining the good rate performance. Jamnik and Maier [13] proposed that the excess lithium could be heterogeneously stored at the interface of Li_2O and metals, the thermodynamic principle dating back to reference [49]. (Here the metals only refer to those not alloying with lithium, e.g. Cu, Ru, etc.) Since neither Li_2O nor metal could store lithium alone, it only happens in a "job-sharing" way: Li^+ resides on one side of the interface in Li_2O (which accommodates Li^+ but not e^-) while e^- resides on the other side in metal (which accommodates e^- but not Li^+); therefore, lithium is locally stabilized at the interfaces of the composites. Owing to individual pathways for Li^+ and e^-, the job-sharing mechanism is proved to show fast storage and may build a bridge between a supercapacitor and a battery electrode

Interfacial storage of nanocomposites has been observed in M/Li_2O or M/LiF, where M stands for electron conductor (e.g., metal or semiconductor) that does not alloy with lithium [16, 20, 21]. Density functional theory (DFT) calculation supported that the mechanism is thermodynamically favorable in both systems, with the storage in M/Li_2O being more substantial than M/LiF [22, 23]. The electrochemical reactions of a variety of metal oxides and metal fluorides were investigated by Li *et al.*[16]. The conversion reaction of metal fluorides normally occurs at higher potential than metal oxides. To eliminate the interference of side reactions, e.g. the decomposition of liquid electrolyte that in particular becomes severe at low potential, here we

choose LiF/Ni nanocomposites as model system. We will perform a series of electrochemical studies and explained them in the framework of a thermodynamic model based on Chapter 2.

3.2 Materials and Methods

Nickel fluoride powder was purchased from Alfa Aesar (99%). For the electrochemical characterization, two electrode Swagelok type cells were assembled in argon filled glove box. As the working electrode, NiF_2 was first mixed with 10 wt.% carbon black, and then the mixture was mixed with a solution of poly(vinyl difluoride) (PVDF) in N-methyl-2-pyrrolidone (NMP) at the weight ratio of 92:8. The slurry was pasted on titanium foil (99.6%, Goodfellow) followed by drying in vacuum at 80 °C overnight. Pure lithium metal (Aldrich) was used as the counter electrode. The electrolyte was 1M $LiPF_6$ in ethylene carbaonte/dimethyl carbonate with the volume ratio of 1:1. Whatman Glass fiber (GF/D) was employed as the separator. The electrochemical measurements were performed at room temperature on an Arbin MSTAT system.

Structure and crystallinity were characterized by X-ray diffraction (XRD) using a Philips PW3710 (40 kV/30 mA) with Cu-Kα radiation. High resolution transmission electron microscope (HRTEM) was carried out using a Philips CM30 ST (300 kV). Prior to XRD and HRTEM characterizations, the Swagelok type cells were dissemble in argon filled glove box and the electrodes were washed using anhydrous dimethyl carbonate.

3.3 Results

LiF/Ni nanocomposites were prepared by an electrochemical conversion reaction from lithium and NiF_2.

$$NiF_2 + 2Li \leftrightharpoons 2LiF + Ni$$

Early works reported that a complete electrochemical insertion of lithium into transition metal fluoride can form a nanocomposite in which LiF is dispersed with transition metal on an atomic or nanometer scale [16, 21].

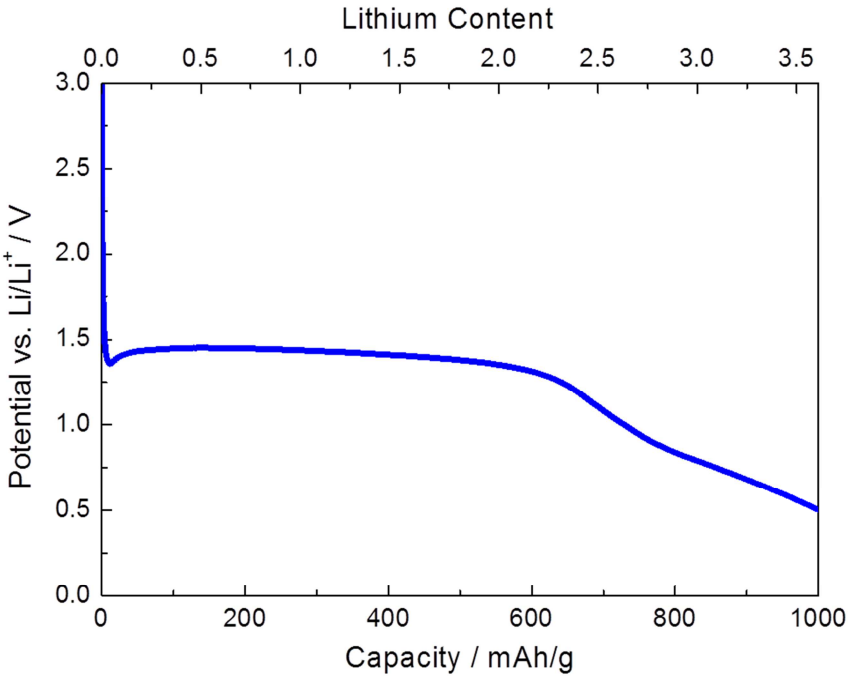

Figure 3.1. Galvanostatic discharge (C/10) curve vs. Li/Li^+ for NiF_2

Figure 3.1 shows the electrochemically lithium insertion into NiF_2 by a galvanostatic discharge on the battery. A plateau at 1.4V is an indication of a three-phase reaction regime where NiF_2 is continuously decomposed into Ni and LiF. If neglecting size effects, the theoretical potential of the plateau is 3V [16]. The high overpotential, probably due to the high energy barrier for nanocrystalline LiF/Ni nucleation, is commonly observed for conversion reactions [50]. The phase evolution on lithiation can be characterized by *ex-situ* x-ray diffraction (XRD). As shown in Figure 3.2, NiF_2 decreases with increase of lithium content and mostly disappears after 2 Li. On the other hand, Ni and LiF appear upon lithiation and a broad hump forms around $2\theta=44.5°$ in the XRD pattern, indicating amorphous or nanophase formation. For some metal oxides such as RuO_2, an intermediate phase ($LiRuO_2$) is formed and involved in the phase transitions [20]. Yet the XRD pattern in Figure 3.2 does not show any intermediate phase and hence LiF/Ni is directly converted from NiF_2. In order to get insight into the nanocomposite, high resolution transmission electron microscope (HRTEM) was performed for the insertion of 2.2 Li (Figure 3.3), where the conversion reaction is definitely complete. It shows that the grain size is around 1-2 nm, similar to other transition metal fluoride systems [16, 21]. Such structure is kinetically favorable for lithium insertion/extraction, and the large contact area of Ni/LiF is suitable to study

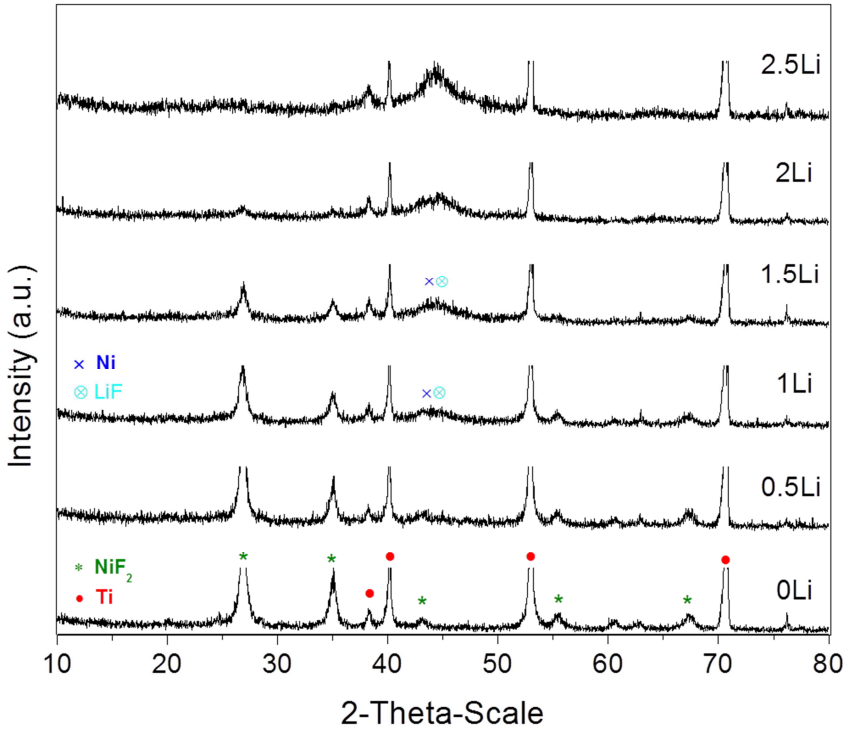

Figure 3.2. Ex-situ XRD for different lithium content during electrochemical synthesis of LiF/Ni. Titanium foil was used as current collector.

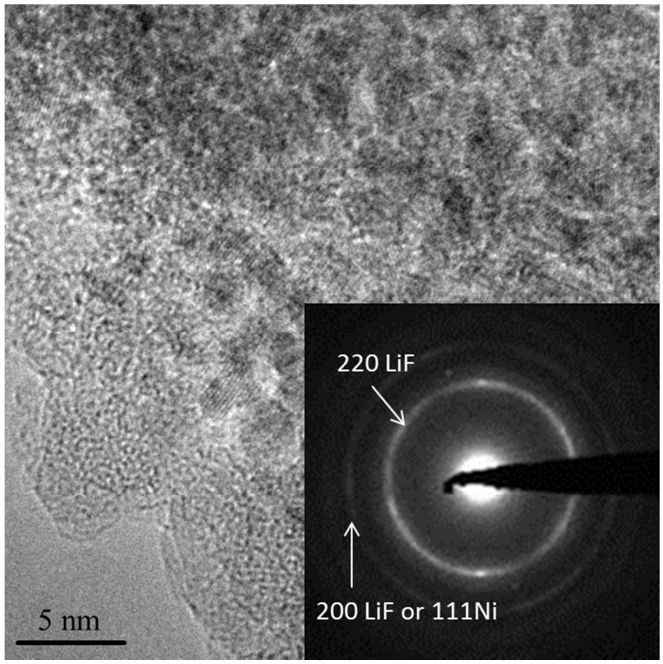

Figure 3.3. HRTEM image of LiF/Ni nanocomposites, synthesized after 2.2Li on NiF_2. The grain size is 1-2nm. SAED pattern confirms no NiF_2 remaining after 2.2Li. .

interfacial storage mechanism. In addition, selected area electron diffraction (SAED) pattern confirmed that there is no NiF_2 remaining at 2.2 Li.

A thin surface film (about 5 nm) is observed around the particles. This attributes to the solid electrolyte interface (so called SEI), which is a passivation layer that forms at electrode/electrolyte contact at low potential. The SEI is believed to be ion-conducting but electron-blocking. Although detailed compositions are not fully clear yet, it may consist of inorganic components reacted from the salts and organic components reduced form the solvent of electrolyte [51]. The SEI growth depends on the surface chemistry of the electrode/electrolyte interface. It mostly forms during the first cycle and is actually a result of electrolyte decomposition leading to irreversible lithium storage. Literature has reported that the SEI formation typically occurs below 0.8V [51, 52] but is also possible at higher potential with the existence of nanometals [53]. Another side reaction that may occur is the formation of LiH, recently proposed by Hu *et al* [48]. They claimed the reaction, due to the absorbed water on the electrode surface, takes place of an equilibrium potential of 0.89V. To exclude the interferences from the above side reactions, NiF_2 was chosen as model material because the potential of NiF_2 conversion reaction (1.4V shown in Figure 3.1) is far away from the range of LiH formation reaction. Cyclic voltammetry in Figure 3.4 displays the reversibility of LiF/Ni nanocomposite. The oxidation peak at 2V in first cycle is likely attributed to electrolyte decomposition [53], and it is greatly diminished after three cycles. The following cycles indicate lithiation/delithiation to be fully reversible between 1.5-2.6V. The voltammetry without obvious redox peaks is analogous to the characteristics of a supercapacitor [54]. Since the electrode particles are surrounded by SEI film which blocks electrolyte, the charges stored in the system are mostly at the solid/solid (LiF/Ni) rather than the solid/liquid (Ni/electrolyte) contact. All in all, the above side reactions that may occur in parallel with interfacial storage can be eliminated or significantly reduced if we choose suitable experiment conditions.

The LiF/Ni nanocomposite was synthesized by inserting 2.2Li into NiF_2. Before any further lithiation, the system was rested for 5 days to reach equilibrium. During the rest period, the potential gradually relaxed to about 1.8V, which we assigned as upper limit of cycling. Figure 3.5a and 3.5b show that the slow discharge/charge (3mA/g) between different potential ranges

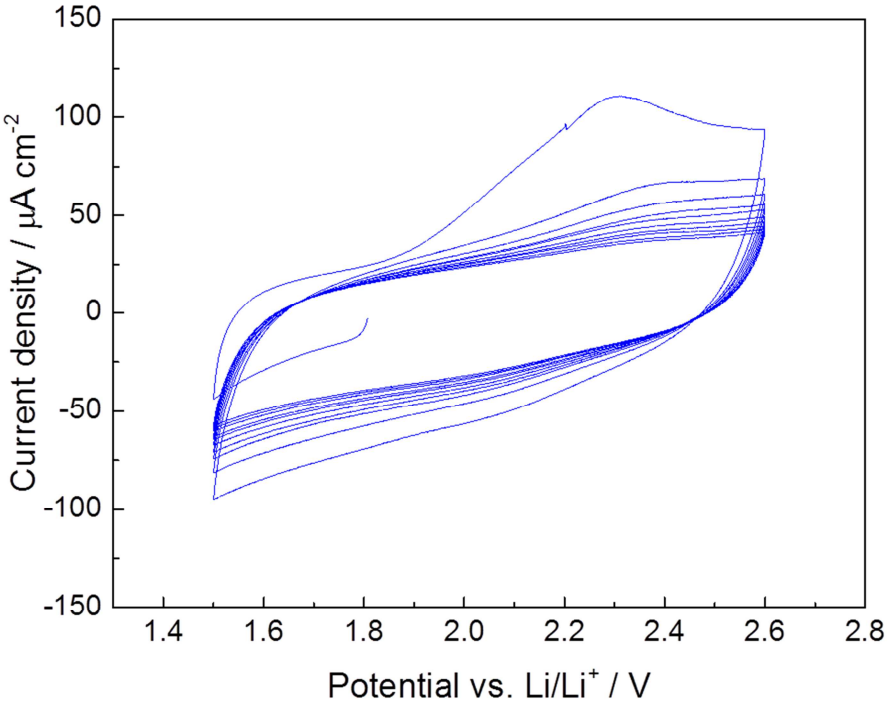

Figure 3.4. Cyclic voltammetry for LiF/Ni nanocomposites, synthesized after 2.2Li on NiF_2 and rested for 5 days. The scan rate is 0.1mV/s.

are fully reversible except the first cycle. To collect most reversible data, the 10th cycle of each potential range was taken for the following analysis.

According to the discussion in Chapter 2, the job-sharing storage contains three regimes: intrinsically dominated mode, diffusive-layer dominated mode, and rigid-layer dominated mode. If we ignore the first mode that only covers marginal capacity, the analytical solution can be simplified as follows

$$a_{Li} \propto {Q_M}^n e^{\gamma Q_M} \qquad (3-1)$$

where a_{Li} is the lithium activity and Q_M stands for capacity per unit mass. The interpretation of the two physical parameters: (i) the power number n, varing with different ionic conductor/electronic conductor situations, and (ii) the pre-factor γ, reciprocal of the space charge capacitance, requires a full understanding of the interfacial defect chemistry.

By plotting $\ln Q_M$ versus equilibrium potential (E) (see Figure 3.5c), we can explore the dependence of interfacial storage on lithium activity. The storage process could be discussed in

different regimes. In the trivial capacity regime (less than 1mAh/g, about 1.7-1.8V), ln $Q_M$increases rapidly with decreasing E. The dramatic change of the dependence is due to the stored capacity being too marginal. Taking into account the resolution of the electrometer and other experimental uncertainties, it is difficult to quantitatively analyze the curve in the region. Nevertheless, the tendency of the discharge curve is very similar to the intrinsically dominated storage curve that we predicted in Chapter 2.

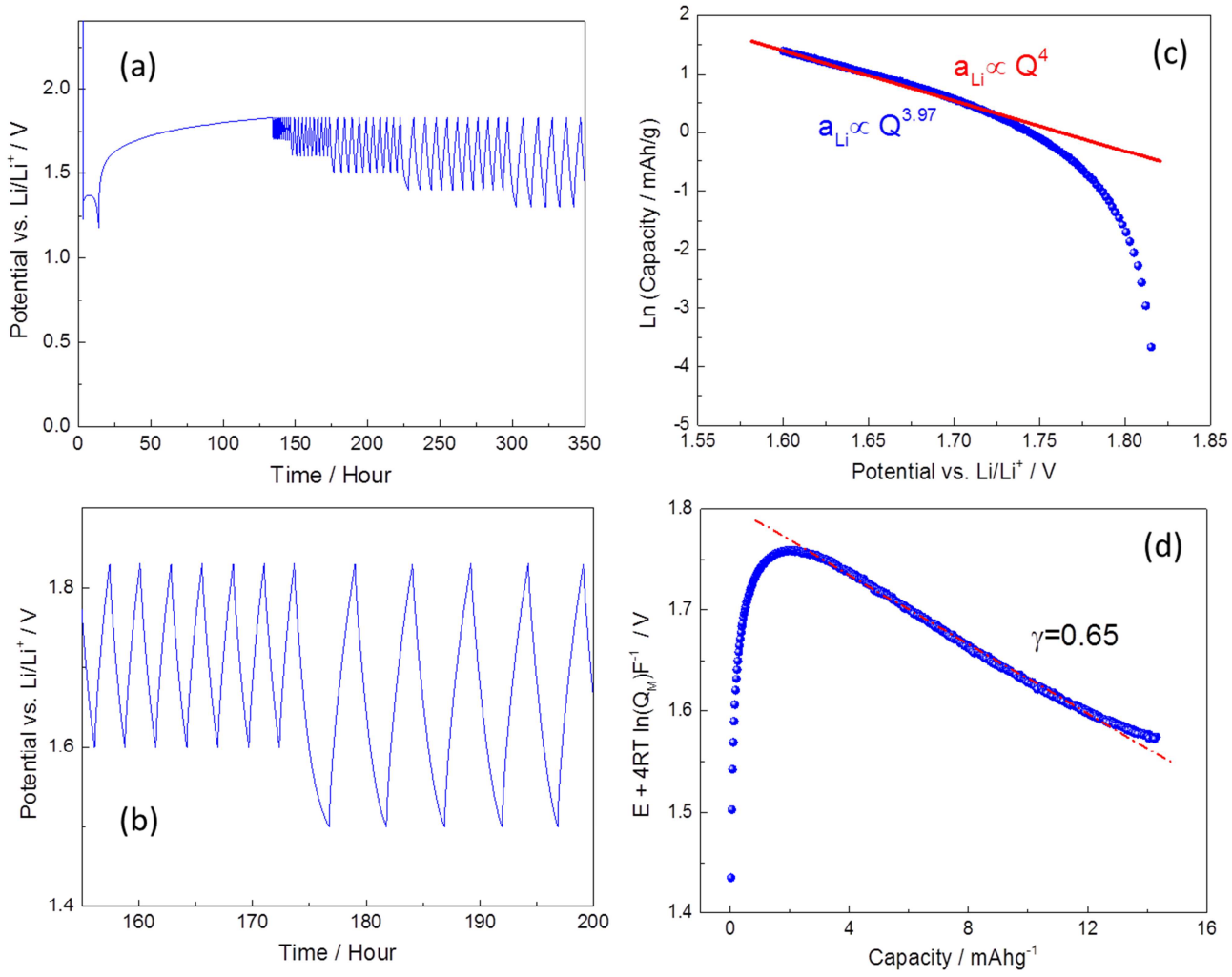

Figure 3.5. (a) LiF/Ni nanocomposites were synthesized after 2.2 Li on NiF_2 and rested for 5 days to reach equilibrium. Except 1st cycle, discharge/charge curves between 1.83-1.3V are highly reversible. (b) The discharge/charge cycles are highly reversible. (c) Dependence of lithium excess storage on lithium activity (10th cycle). (d) Dependence of E + 4RTln(Q_M)/F on interfacial storage.

Now we extend the analysis to lower potential regime in Figure 3.5c where the capacity becomes perceptible. First, the diffusive layer dominated mode is highlighted when the capacity is not so pronounced. The power law of a_{Li} and Q_M varies, depending on the nature of electronic conductor, from n = 2 (as weak metal) to n = 4 (as semiconductor). Although metallic Ni is produced by conversion reaction of NiF_2, we cannot exclude the possibility that some of the Ni were oxidized in contacted with the electrolyte thereafter. The complexity of the system makes an accurate analysis challenging. However, in any case the value of the power in diffusive layer dominated storage should be between 2 and 4. In Figure 3.5c, a straight line starting from the origin of y-axis (i.e. Q_M is 1mAh/g) is observed, and the exponent is calculated to be 3.97, which nicely fits in the predicted range of the model. Similar results were reported for Li_2O/Ru systems recently [24]. Both systems show that the developed model is in good agreement with experimental results and independent of the specificities of materials.

When the capacity becomes more considerable, the electrostatic part starts playing an important role. Thus, the power law deviates from diffusive-layer dominated storage behavior. To extract more physical properties from the discharge curve, we use the same approach as given in our paper [24]. The γ value (reciprocal of the space charge capacitance) of the rigid double layer could be obtained if we plot E + nRTln(Q_M)/F vs. Q_M. Here n is the power value retrieved from diffusive layer dominated storage. Figure 3.5d suggests that the curve linearizes with a γ value of 0.65, which again nicely fits the anticipated magnitude of our model. (The γ value is expected to be on the order of 1 g/mAh, when using reasonable values of s, ε, and grain size of the composite. See more details in reference [24] or Appendix III.) Note that the linear fitting deviates from the curve when capacity is small because the n value 3.97 is not applicable for the intrinsic storage mode.

Another method to obtain these physical parameters is directly fitting the discharge curve. Figure 3.6 shows that the fitting curve conforms with the discharge curve except the region $Q_M \leq 1$ mAh/g. The deviation is mainly because equation (3-1) does not take the intrinsically dominated storage mode into account. The obtained physical parameters n =3.25 and γ =0.74 g/mAh are in agreement with the above discussion.

So far, we have explored the lithium excess storage of LiF/Ni nanocomposites. For this system, an inverse process, via forming lithium deficiency (V'_{Li}, $h^{\bullet}$), appears to be thermodynamically

favorable as well. Like other lithium halides, LiF exhibits Schottky disorder and hence intrinsically forms lithium and fluoride vacancies, while the former is reported more mobile than the latter, characterized by nuclear magnetic resonance (NMR) techniques [55, 56]. On the other hand, Ni is a neutral transition metal that may serve as either electron accepter or donor, at least on the first layer. These physical properties may cause LiF/Ni to be a good model system for studying lithium removal in the composite materials.

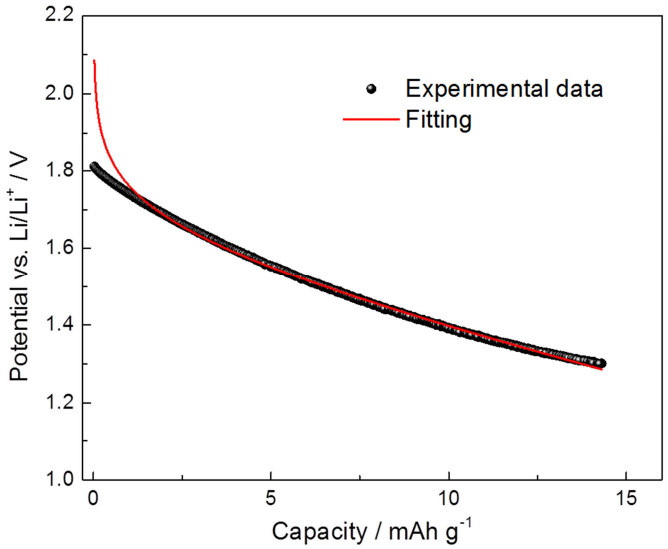

Figure 3.6. Comparison of the discharge curve in Figure 3.5a and the corresponding linear fitting.

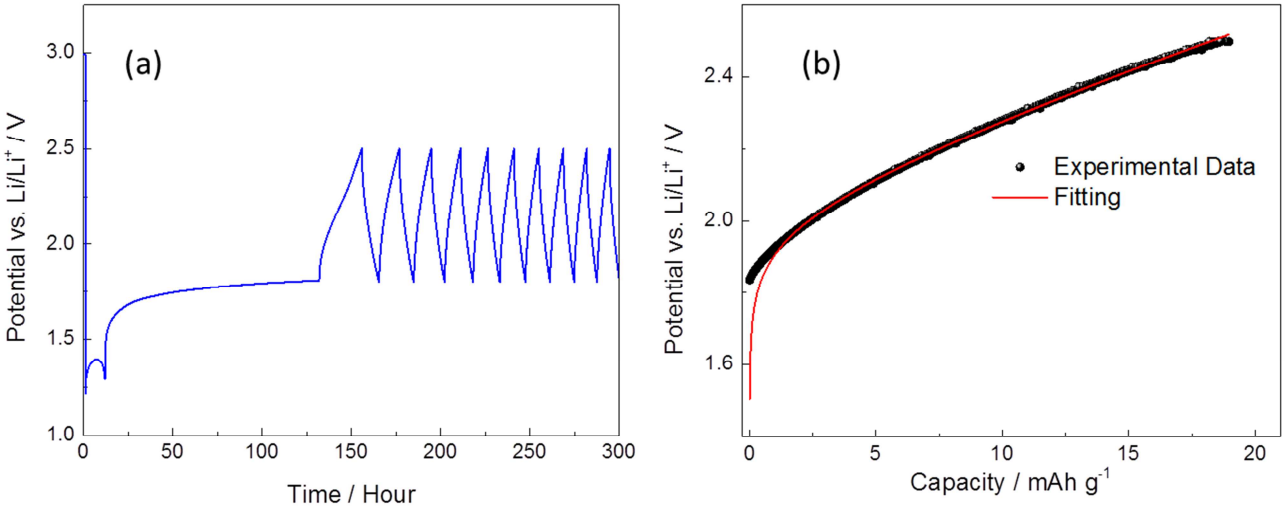

Figure 3.7. (a) Lithium removal for LiF/Ni nanocomposites. The synthesis is as same as described in Figure 3.5a. (b) Experimental data and fitting of the dependence of lithium deficiency on lithium activity (10^{th} cycle).

LiF/Ni nanocomposites were again synthesized via conversion reaction of NiF_2 and relaxed for 5 days (Figure 3.7). Instead of discharge, the system was directly charged and then slowly cycled (3mA/g) between different potential ranges. Note that the upper limit should not be above the equilibrium potential of conversion reaction, i.e. 2.96V [16]. Otherwise, the LiF/Ni composite will be back-converted to nanocrystalline NiF_2.

The charge/discharge processes are fully reversible except the first cycle. To analyze the lithium removal in LiF/Ni composites, we adopted the data from the 10^{th} cycle. The fitting curve with equation (3-1) turns out to be in a good agreement with the experimental data except the marginal storage region where the intrinsically dominated mode is dominant. Taking account of the complexity of the system, the extracted parameters n and γ, 3.01 and 0.84, are close to those for lithium excess storage. This indicates that for LiF/Ni nanocomposites both lithium excess and deficiency are feasible. More importantly, the comparable values of n and γ suggest that the storage mode relies on the physical properties of the interface rather than the operating potential range in which different side reactions may take place.

Since γ (reciprocal of double layer capacitance) is linearly proportional to the contact distance, it is expected that γ increases upon forming lithium vacancies at the interface. If we assume that a monolayer of lithium is removed and hence the average contact distance extends, it is understandable why the γ value slightly increases on increasing deficiency.

3.4 Discussion

The interfacial storage has demonstrated the significance of space charge effects for mass storage. In addition to fundamental research, it also raises the interest for energy storage applications. Almost all battery electrode materials are ionic crystals with mixed electronic-ionic conductivities. As the crystal grains consist of bulk and boundary zones, the mass storage is composed of bulk and interfacial contributions. Figure 3.8 illustrates the charge carrier distributions at the boundary of a lithium electroactive material. For ionic materials, the interfacial and bulk properties are strongly correlated. For instance, the thickness of the space charge layer is inversely proportional to the square root of the charge carrier concentration in bulk phase [57]. At small lithium content, the low bulk concentration leads to a broad space

charge layer (Figure 3.8a). With the increase of lithium storage, both bulk and interfacial storage increase but the space charge thickness is shirked due to the rise of bulk concentration (Figure 3.8b).

To analyze the contributions from the bulk and from the interfacial zone, it is straightforward to compare the corresponding $a_{Li} - Q$ relations. For the storage in bulk phase, a_{Li} is proportional to the square of capacity [4] while for the storage in boundary region, the dependence of a_{Li} varies with different storage modes. Whether in diffusive or rigid layer dominated modes, it follows the same tendency: at low storage the interfacial capacity exhibits higher degree of influence. At high storage, although the interfacial and bulk capacity both increase, the former becomes less relevant.

It is also worth mentioning that the space charge region in Figure 3.8 is key to kinetic and transport properties. The incorporation of Li^+ and e^- into electroactive materials relies on charge transfer reactions and Li transport. On one hand, the Li^+ accumulation layer could increase the rate of charge transfer reaction, because Li^+ serves as the reactant species. On the other hand, Li transport along the interface also benefits from rapid Li storage. Since the ionic conductivity is proportional to the charge carrier concentration [40], a significant enhancement of local conductivity at the interface is expected.

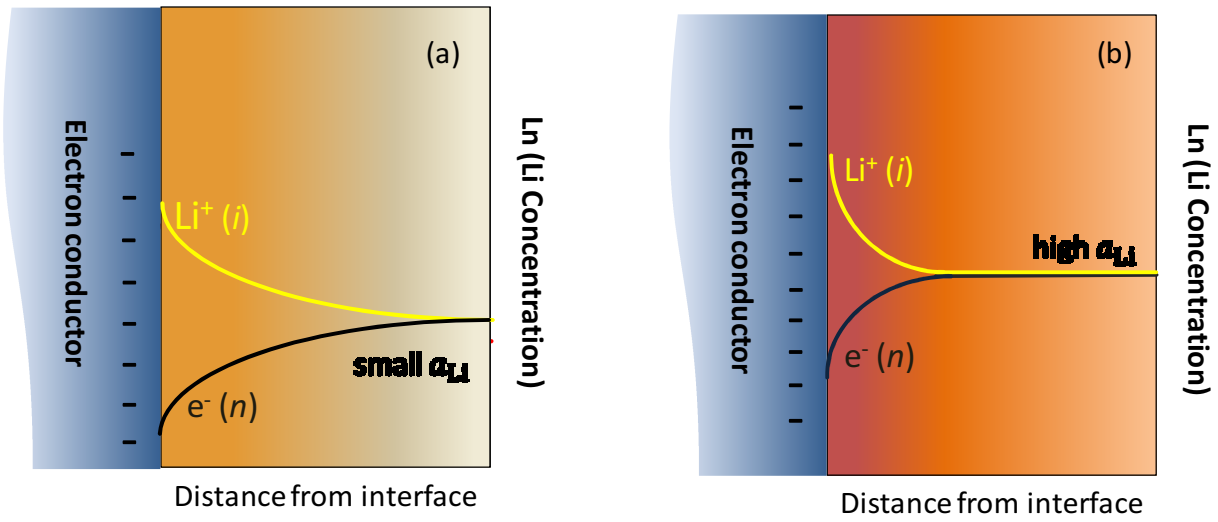

Figure 3.8. Sketch of Li storage in a nanocrystalline electroactive material which can store Li in bulk and subsurface. (a) Small storage and (b) large storage. Figure is taken from [24].

The interfacial effects on kinetic and transport aspects turn out to be particularly important for nanocrystalline materials. This is not only due to the short diffusion length in the bulk of the nanocrystals but also due to the high impact of space charge effects taking place on the large surface area. These highly favorable factors in kinetics and transports enable nanostructured materials to offer efficient and fast storage techniques. Examples with excellent rate performance in Li batteries have been recently reported for nanocrystalline TiO_2 [58] and MoS_2 [59].

3.5 Conclusion

This chapter presents experimental evidence to support the developed storage model in chapter 2. The model system LiF/Ni nanocomposite has been electrochemically synthesized via conversion reactions. As neither LiF nor Ni could accommodate Li alone, the LiF/Ni composite is a good candidate for studying the stoichiometric variation at space charge layers. Based on the dependence of the equilibrium potential on storage capacity, the experimental results are in a good agreement with the developed model. The stoichiometric change covers different regimes and the extracted parameters n and γ are physically reasonable. More excitingly, the nonstoichiometry range covers not only Li excess but also Li deficiency. It suggests that Li can be reversibly added or removed in the LiF/Ni junctions.

The finding is important for a complete understanding of conventional storage mechanism. As ionic materials contain bulk and boundary zones, it is necessary to unify both bulk and space charge storage, in particular for nanocrystalline electrodes. The space charge effects play a key role in storage, charge transfer, and mass transport aspects. As we will show in the next chapter, the novel mechanism is able to push mass transport rates to expectedly high level.

4

Experimental Evidence II:

Silver Storage and Removal at $RbAg_4I_5$/Carbon Interface

In this chapter we will continue to experimentally investigate the interfacial storage. The chosen model system is the $RbAg_4I_5$/carbon junction, whereby $RbAg_4I_5$ is a superionic conductor and carbon a good electronic conductor. The fabricated silver all-solid-state batteries clearly suggest distinct stoichiometric variations in the $RbAg_4I_5$/carbon composites used as electrodes. The full picture of defect chemistry includes four regions: I_2 liberation, Ag deficiency, Ag excess, and Ag deposition. Unlike stoichiometric variation in conventional mixed conductors, here the deficiency and excess are established in a job-sharing way. That is, Ag deficiency is realized by vacancies on the $RbAg_4I_5$ side and holes on the carbon side while Ag excess is realized by interstitials on $RbAg_4I_5$ and electrons on carbon.

Equally exciting as the finding of a compositional variation is the kinetics. The storage/removal process has highly favorable kinetics. The obtained mass transport rate is bounded by the ambipolar interfacial diffusion. As interpreted by the heterogeneous diffusion model, the enormous chemical diffusion coefficient is attributed to the very low chemical resistance and the very low chemical capacitance. Moreover, electrochemical applications including permeation membranes, battery electrodes, and supercapacitors will be demonstrated.

4.1 Introduction

Solid state ionics is the scientific discipline concerned with the motion of ions in the solid state. It started with the work by Michael Faraday, who discovered the ionic conductivity of high temperature solid electrolyte Ag_2S and PbF_2 in 1834 [60]. Several decades later Walther Nernst [61] elucidated a theory that enables one to predict the equilibrium potential of a galvanic cell. His famous Nernst equation marks not only the foundation of solid state ionic but also that of modern electrochemistry. In the early 20^{th} century another big step forward was made by Frenkel, Schottky, and Wagner [62, 63]. They developed the thermodynamics of point defects in ionic crystals, which later became the core of the study of defect chemistry. In the 1970s, Liang [25] discovered that the ionic conductivity of LiI could be increased by orders of magnitude by mixing some amount of insulating material Al_2O_3. The anomalous increase of the conductivity, later realized by the space charge effects in the nanosized systems, is the beginning of nanoionics [64]. The study of nanoionics turns out to be very important today as nanomaterials are extensively used in many applications such as fuel cells, batteries, and sensors [65].

The job-sharing storage concept expands the space charge effect from charge transport to mass storage. Chapter 3 has illustrated that, by choosing LiF/Ni nanocomposites as a model material, the experimental evidence nicely agrees with the developed model. In this chapter, we will show another experimental corroboration using Ag all-solid-state batteries. As we are able to vary the ratio of ionic conductor/electronic conductor in the composites, it can directly be proved that the storage is related to the contact area. More importantly, the solid electrolyte could avoid passivation layer formation that usually occurs in liquid electrolyte systems.

The solid electrolyte is the key component of the all-solid-state cells. One breakthrough of solid electrolyte development was the discovery of superionic conductors. In 1914, Tubandt and Lorenz [66] observed that the ionic conductivity of AgI increases by three orders of magnitude above 147^oC even though it is a weak ionic conductor at low temperature. As later suggested by the structural analysis [67], the unprecedented ionic conductivity (≈1S/cm) is due to a phase transition from wurtzite to body-centered cubic; in the latter form AgI could provide 42 available sites for 2 silver ions in the cubic unit cell. The large number of available sites therefore causes Ag^+ to move "freely" within the lattices. In the 1960s, two groups [68, 69] simultaneously developed a new family of superionic conductors, in which $RbAg_4I_5$ exhibits the highest ionic

conductivity at room temperature. Like the high temperature phase AgI, the structure of $RbAg_4I_5$ is also cubic and it provides 56 available sites for 16 silver ions in a unit cell [70].

In this chapter $RbAg_4I_5$ is used not only as electrolyte but also as the component of the working electrode. $RbAg_4I_5$/carbon is selected as our model system to investigate the case of superionic conductor/weak metal junction. As introduced in Chapter 2, the prerequisite of mass storage needs both adequate ionic and adequate electronic charge carriers. Due to its extremely low electronic defects [42], $RbAg_4I_5$ is thermodynamically unable to accommodate Ag, i.e. Ag^+ and e^- . On the other hand, carbon is the most common electrode materials used in sustainable energy applications [71]. In lithium batteries, for instance, graphite can accommodate lithium via the intercalation reaction, i.e. lithium being located between the graphene layers linked by van der Waal bonds. The intercalation mechanism, however, is not applicable for storing silver [72], due to the large size of silver atom.

Another concern worth mentioning is that there is no indication of under-potential deposition (UPD) at the $RbAg_4I_5$/carbon contact. Here UPD refers to the electrodeposition of silver above 0V vs. Ag/Ag^+. Typically such a mechanism involves Ag monolayer adsorption on the metal (e.g. Pt) surface [73], as a result of strong interaction between Ag and the metal. The readers should not confuse the proposed job-sharing storage with the UPD, although they both seem to occur on the electrode surfaces. For the former the metal ions and the electrons locate in difference phases (no neutral metal precipitation) while for the latter both charge carriers are in the same phase (presence of neutral metal). Hull *et al.* [74] studied the double layer capacitances of the interface of AgI in contact with graphite or Pt. The capacitance of AgI/graphite interface is independent of the potential over the range of -0.03~0.46 V (vs. Ag/Ag^+), indicating a pure double-layer behavior. In contrast, the AgI/Pt interface behaves like an ideal reversible system involving UPD. Their conclusion was confirmed in other silver halides or silver alkaline halides systems [75-77].

In views of the above aspects: (i) neither $RbAg_4I_5$ nor carbon could store Ag in the bulk phase and (ii) no indication of UPD at the $RbAg_4I_5$/carbon interface. The composites of $RbAg_4I_5$/carbon are chosen as model material for studying the job-sharing storage mechanism.

4.2 Materials and Methods

4.2.1 Synthesis of $RbAg_4I_5$ and $RbAg_4I_5$/Carbon composites

$RbAg_4I_5$ was synthesized by melting a near-stoichiometric mixture (83:17mol%) of AgI (Sigma-Aldrich, 99.999%) and RbI (Sigma-Aldrich, 99.9%) at 450°C for 2 hours, followed by rapid cooling. $RbAg_4I_5$/graphite composites were first mixed with AgI/RbI and the appropriate amount of graphite (Alfa Aesar, 99.9995%) in an agate mortar. (The water content of graphite is less than 100ppm, according to thermogravimetric analysis.) To improve the $RbAg_4I_5$/graphite contact, the mixture was melted at 450°C for 10 hours. For composites of $RbAg_4I_5$ and multi-wall carbon nanotubes (MWCNTs), the procedure was the same except replacing graphite with MWCNTs (Sigma-Aldrich, 98% O.D. 10nm × I.D. 4.5nm × L 6μm). All syntheses were carried out in dark under Ar atmosphere.

4.2.2 Characterization methods

Structure and crystallinity were characterized by X-ray diffraction (XRD) using a Philips PW3710 (40 kV/30 mA) with Cu-Kα radiation. Scanning electron microscopy (SEM) analysis was performed using a Zeiss Gemini DSM 982 scanning electron microscope. The nitrogen-adsorption and desorption isotherms were measured using an Autosorb-1 system (Quanta Chrome). Transmission electron microscopy (TEM) was performed with a Phillips CM30 ST (300 kV, LaB_6 cathode). Thermogravimetry was carried out with Netzsch STA449C Jupiter TG.

4.2.3 Wetting experiment

Synthesized $RbAg_4I_5$ was melted on highly oriented pyrolytic graphite (HOPG, NT-MDT, ZYB) surface. To obtain a smooth and clean surface, before the wetting experiment the top side of HOPG was cleaved by using scotch tape. The experiments were performed under the same conditions as described in section 4.2.1.

4.2.4 Electrochemical experiment

The prepared $RbAg_4I_5$ and $RbAg_4I_5$/graphite composites served as solid electrolyte and cathode. A mixture of silver powder (Sigma-Aldrich, 99.9%) and $RbAg_4I_5$ in the weight ratio of 4:1 was used as anode. Powder compacts of each cell component were uniaxially pressed into 5mm diameter pellets at 35 MPa for 1 minute. Graphite pellets are difficult to prepare by cold-pressing, hence graphite rods (Sigma-Aldrich, 99.999%) were used instead. Platinum foil and Ag foil were employed as cathodic and anodic current collectors, respectively (Figure 4.1). After assembling all the components, the batteries were placed in gas tight quartz setups. To reduce the contact resistance, the cell was slightly spring-loaded. Under Ar atmosphere, the electrochemical experiments were performed in dark at 25°C on an Arbin MSTAT system.

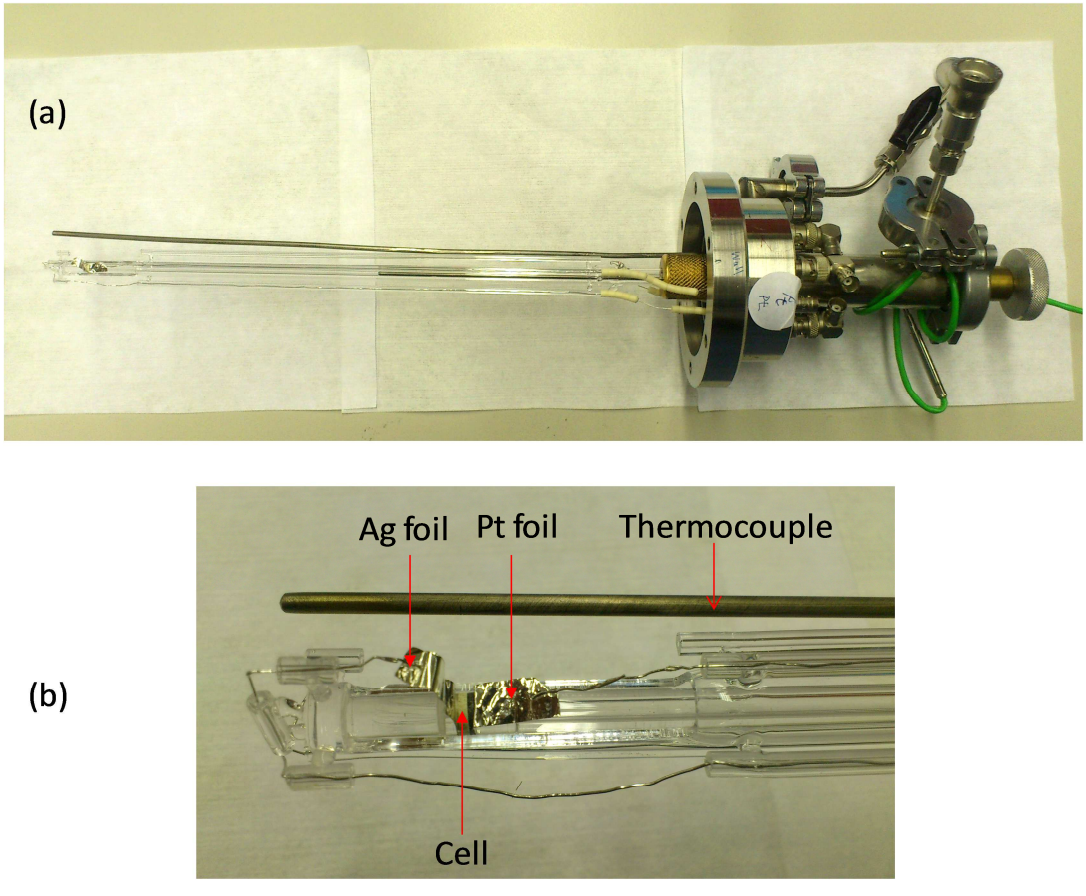

Figure 4.1 Apparatus of electrochemical experiment. Ag and Pt foil are anodic and cathodic current collector, respectively. The cell is sandwiched between the two foils.

The coulometric titration experiment (i.e. galvanostatic intermittent titration technique, GITT) consists of a series of current pulses, followed by an equilibration period. Then constant currents for specific intervals of time were applied. Depending on the volume ratio, the time intervals ranged from 30 seconds to 3 minutes for $RbAg_4I_5$/graphite composites (10^{-5}A/g) and from 3 to 5 minutes for $RbAg_4I_5$/MWCNTs composites (10^{-4}A/g). After switching off the current, the open circuit potential was measured until the system has reached equilibrium. The equilibration time typically ranged from 15 to 30 minutes.

For the extremely slow galvanostatic charge/discharge on pure $RbAg_4I_5$, a very small constant current of $4 \times 10^{-10}Ag^{-1}$ was supplied by Keithley 220 current source. The potential was measured by Keithley 6514 electrometer.

Besides battery cells, all-solid-state supercapacitors were fabricated by sandwiching a $RbAg_4I_5$ pellet in between two $RbAg_4I_5$/graphite composite pellets. The preparation methods and the pellet sizes were the same as mentioned earlier. Platinum foils were used as current collectors. For the rate evaluation the electrochemical cells (i.e. batteries and supercapacitors) were tested in Swagelok type cells. The assembling was done in argon filled glove box. The electrochemical impedance spectroscopy was conducted by Voltalab PGZ402 impedance analyzer with 5mV signal amplitude. The frequencies ranged from 10^5 to 0.01 Hz. The relaxation time of the supercapacitor was obtained by analyzing the frequency dependence of the real and imaginary part of the complex capacitance [78].

4.2.5 Electrical Characterization

The samples were pressed into 5mm diameter pellets under same pressing conditions as described above. Conducting platinum electrodes (about 400 nm thick) were sputtered onto the both sides of the pellets. The impedance measurements were carried out using a Novocontrol Alpha-A High Performance Frequency Analyzer at frequencies ranging from 10 MHz to 0.01 Hz.

4.2.6 Ag permeation experiment

Ag_2S (Sigma-Aldrich, 99.9%), Ag_2Se (Sigma-Aldrich), and $RbAg_4I_5$/graphite composites were used as working electrodes. The anode, electrolyte, anodic current collector, and the pressing conditions were the same as for the electrochemical experiments. The sensor probe was similar to the electronic probe used in reference [79]. The length of the working electrode was about 2-3 mm. Pt wire was wrapped around the working electrode bar. The position of the Pt wire was in the center of the bar.

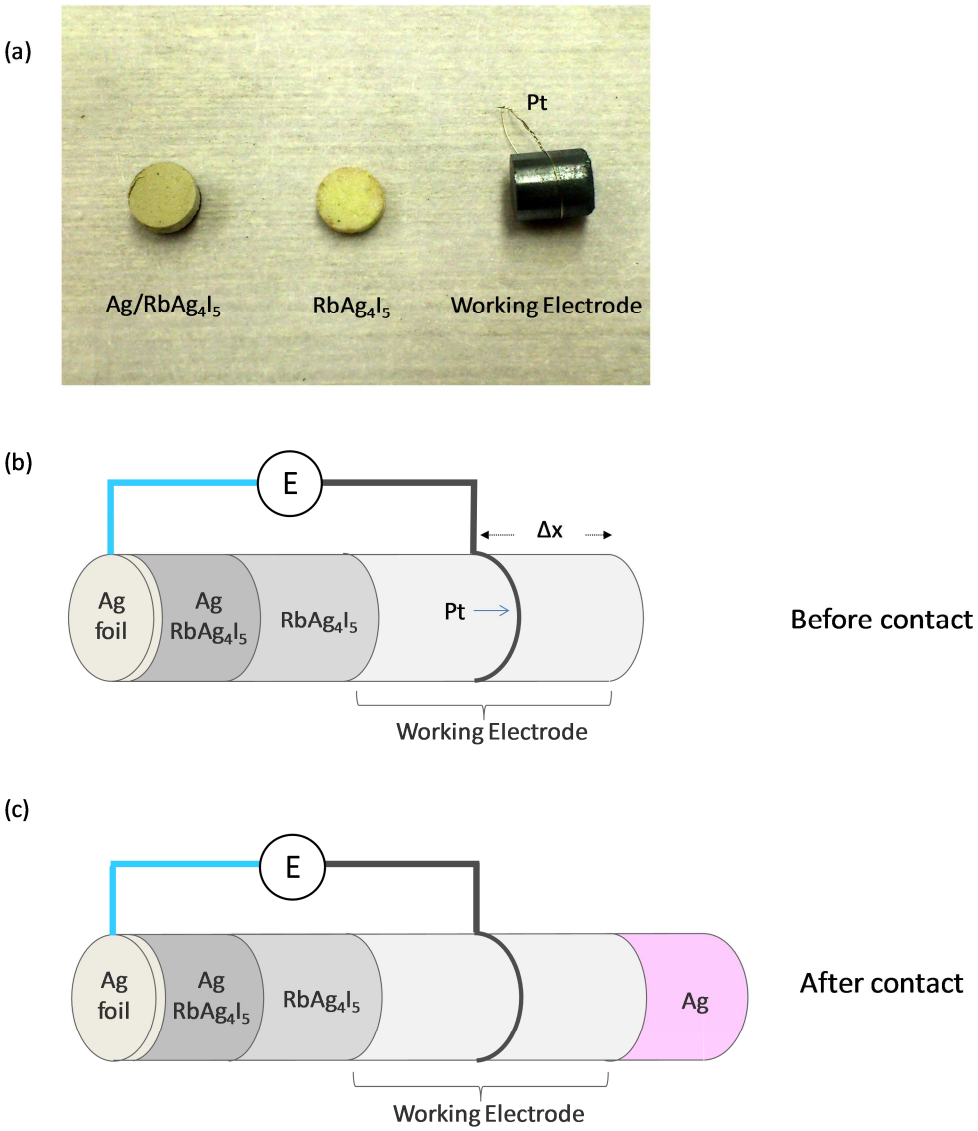

Figure 4.2. Permeation experiment. (a) Electrode components. (b) Schematic of cell configuration before Ag contact and (c) after Ag contact.

The electromotive force (emf) was measured under Ar atmosphere between Ag anode and the working electrode. The emf was very stable, at least for 10 hours. Before starting the permeation experiment, the quartz setup was opened and the emf measurement was switched off. An Ag pellet was contacted and fixed on the outer side of the working electrode. Then the measurement setup was closed and vented with Ar. The process took about one minute. Afterwards, the emf was recorded for at least 6 hours.

4.3 Results

4.3.1 Material Characterization

Since $RbAg_4I_5$ is prepared by melting the stoichiometric mixture of AgI and RbI, the SEM image (Figure 4.3) suggests the morphology to be flat and dense. Like silver halides, $RbAg_4I_5$ decomposes to metallic silver upon exposure to light. So the focus time during the SEM observation should be as short as possible. The prepared $RbAg_4I_5$ pellets exhibit very low ionic resistance and the corresponding conductivity are consistent with the literature [80, 81].

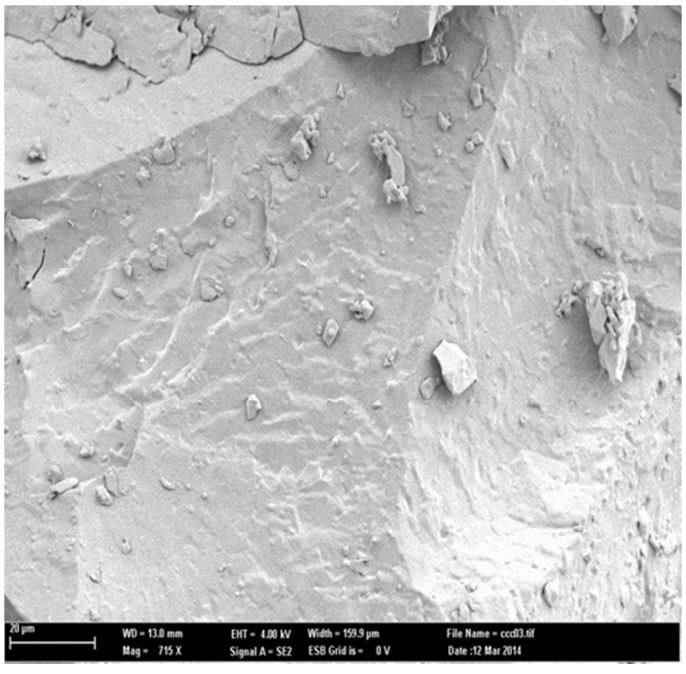

Figure 4.3 SEM image of $RbAg_4I_5$.

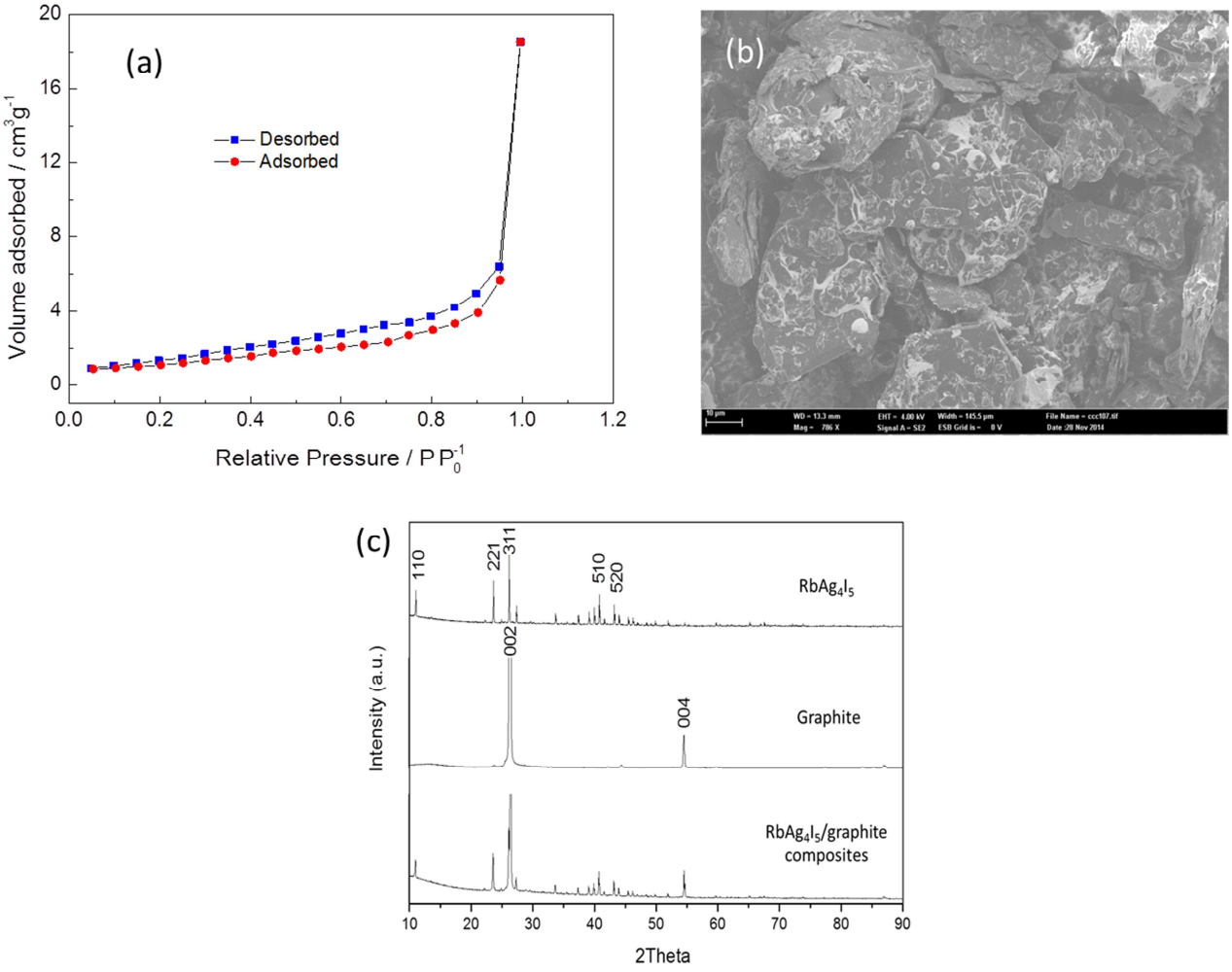

Figure 4.4 (a) Nitrogen adsorption and desorption isotherm for graphite powder. (b) SEM image of $RbAg_4I_5$/graphite composites (25% volume fraction of $RbAg_4I_5$). (c) XRD for $RbAg_4I_5$, graphite, and $RbAg_4I_5$/graphite composites.

The resulting composite is composed of $RbAg_4I_5$ and graphite. According to the nitrogen adsorption and desorption isotherm (Figure 4.4a), the BET area of graphite is characterized to be 4.26 m^2/g. Figure 4.4b shows that $RbAg_4I_5$ is dispersed in the micrograin sized graphite. The percolation of heterophase boundary is essential for the storage in the job-sharing composites. Phase diagram of AgI-RbI [82] suggests that below 27^{o}C $RbAg_4I_5$ is thermodynamically unstable and decomposes to Rb_2AgI_3 and AgI, leading to a significant drop of ionic conductivity. Fortunately, the kinetics of the decomposition reaction is very sluggish especially in absence of water vapor in the air [83]. Thus the prepared samples should be stored in evacuated desiccators.

As confirmed in Figure 4.4c, the XRD pattern of $RbAg_4I_5$ does not show any indication of Rb_2AgI_3.

The contact situation of $RbAg_4I_5$ and graphite is the key factor for the interfacial storage. To further investigate the contact properties, it is necessary to understand the wetting behavior of $RbAg_4I_5$ on graphite surface. The SEM image in Figure 4.5a suggests that the drop-like $RbAg_4I_5$ on HOPG surface is a nonwetting characteristic. As we will show later, taking the significant amount of interfacial storage into account, such wetting behavior is characteristic of Stranski–Krastanov growth and has been clearly observed for growth of H_2O on Pt surface [84]. The growth process is characterized by distinct wettability for the first monolayer on the substrate but poor wettability for further H_2O on this monolayer. For the $RbAg_4I_5$/graphite composite, such microstructure is indeed observed by TEM: Figure 4.5b shows ultrathin films on the graphite surface in between the $RbAg_4I_5$ islands. The diffraction pattern further confirms the lattice of the film corresponding to cubic structure (as $RbAg_4I_5$) rather than hexagonal (as graphite). The heterophase percolation is crucial not only for interfacial storage but also for interfacial transport because it enables the charge transport along the interface even without bulk percolation.

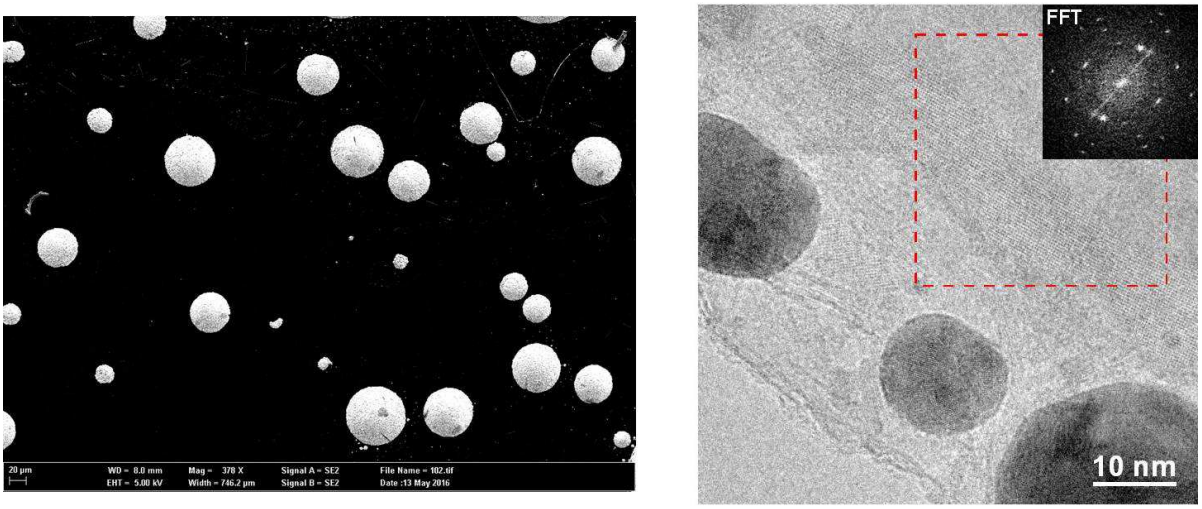

Figure 4.5 (a) SEM image for $RbAg_4I_5$ on HOPG surface. (b) TEM image for the $RbAg_4I_5$/graphite composite.

To evaluate the influence of contact area on the storage, multi-wall carbon nanotubes (MWCNTs), a highly conductive carbon with large surface area, were used to replace the graphite. Unlike the microflake-like structure of graphite, Figure 4.6 suggests that the nanofiber-like structure of MWCNTs results in high BET area 274 m^2/g, 60 times of the graphite.

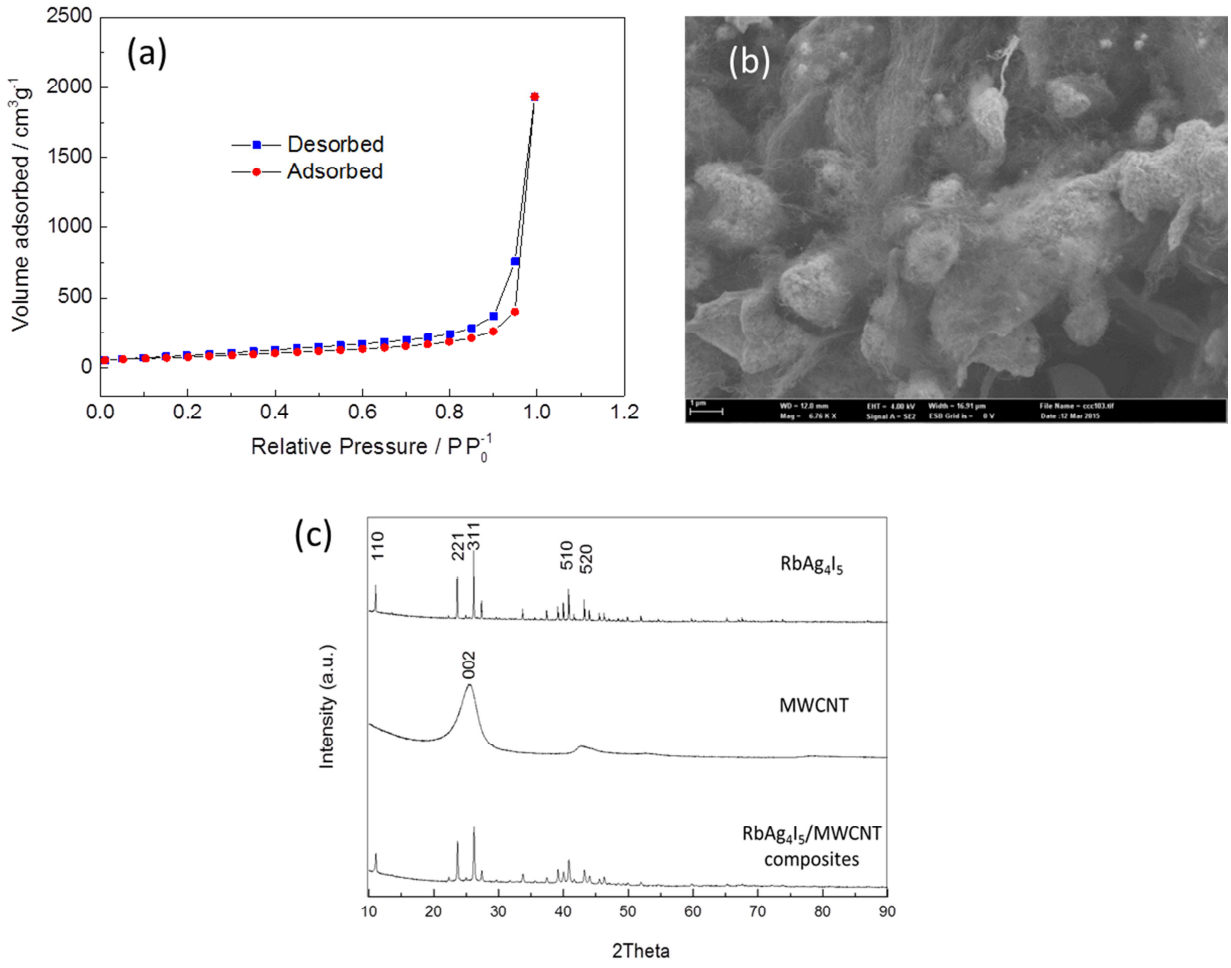

Figure 4.6 (a) Nitrogen adsorption and desorption isotherm for MWCNTs powder. (b) SEM image of $RbAg_4I_5$/ MWCNTs composites. (c) XRD for $RbAg_4I_5$, MWCNTs, and $RbAg_4I_5$/ MWCNTs composites.

4.3.2 Thermodynamic study by coulometric titration

Coulometric titration is a useful technique to study the electrochemical properties of mixed conductors. Wagner [8] first employed the coulometric titration in 1953 and reported a reversible silver addition/removal for Ag_2S. The compositional variation is realized by excess (silver

interstitial ions $Ag_i^{\cdot}$ and electrons e') and by deficiency (silver vacancies V'_{Ag} and electron holes $h^{\cdot}$). Note that the typical expression representing the compositional variation is $Ag_{2+\delta}S$, where the positive value of δ stands for silver excess and negative for silver deficiency. Later the technique has been generally used in the study of nonstoichiometry of other ionic materials, such as lithium [85] and oxide [86] conductors.

The GITT technique uses a series of current pulses, each followed by an equilibration time. Illustrated in Figure 4.7 inset, an open circuit potential of 200mV (vs. Ag/Ag^+) is stably shown before titration. Upon applying current on the composites, the polarization is characterized by IR drop and Ag diffusion [40, 87]. After cutting off the current, the potential relaxes to a higher equilibrium potential (234mV). The 34mV potential rise indicates, according to Nernst equation, a variation of Ag activity due to the compositional change.

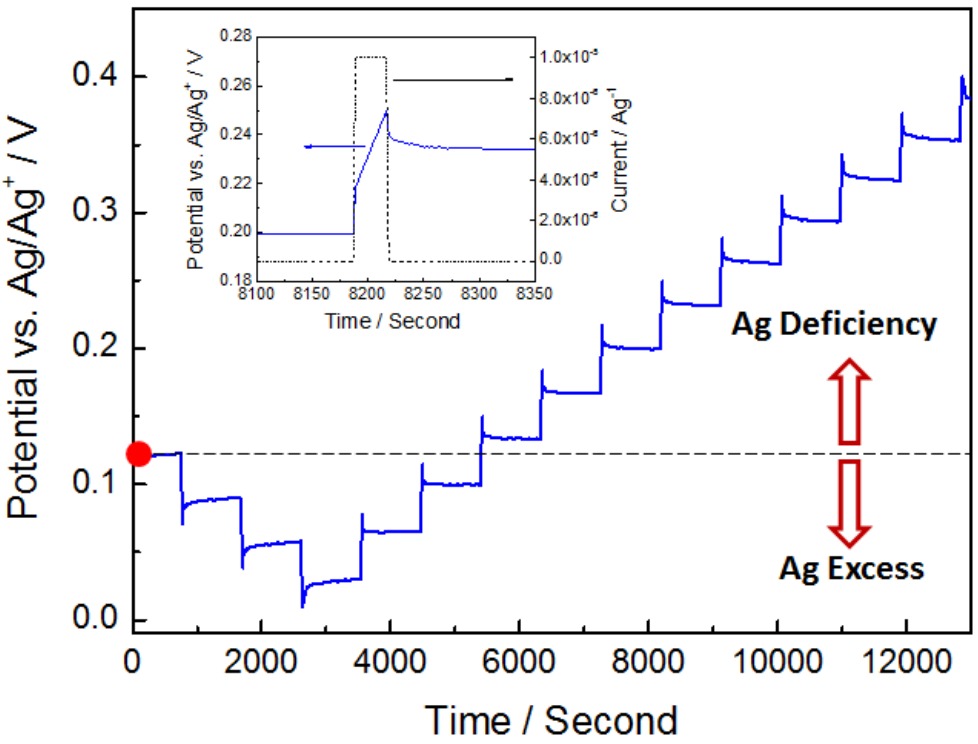

Figure 4.7 The coulometric titrations of the $RbAg_4I_5$/graphite composite. A current of $10^{-5}Ag^{-1}$ was applied to the cell for 30 seconds, followed by a cut-off relaxation for 15 minutes. The lower limit is bounded by Ag deposition reaction (0V). The titrations are reversible and include both silver excess and silver deficiency.

In Figure 4.7 an initial potential of 120mV is assigned as equilibrium potential of the stoichiometric point.[4] The lowering of the equilibrium potential upon each titration stands for the addition of silver in the composites. Since neither $RbAg_4I_5$ nor graphite could accommodate silver excess, it can only happen when $Ag_i^{\cdot}$ locates on the $RbAg_4I_5$ side of the boundary while e' on the graphite side. The lower limit of the titration is bounded by silver deposition, i.e. 0V. Then reversed titrations are performed to remove the additive silver. After up-taking almost same amount of excess storage, the equilibrium potential returns to the stoichiometric point, demonstrating that the addition/removal process is highly reversible.

More exciting is that the charging titrations can be continued above the stoichiometric potential. It suggests that Ag can be additionally removed from the composites. As $RbAg_4I_5$ is the only Ag source for removal, it solely happens when V_{Ag}' is formed in $RbAg_4I_5$ with $h^{\cdot}$ compensation from the adjacent graphite phase. The coupling of V_{Ag}' and $h^{\cdot}$ is comparable to the Ag deficiency in bulk phase.

The limit of silver removal is bound by the point at which iodide ion oxidizes to iodine, corresponding to 670mV (vs. Ag/Ag^+) [80]. As shown in Figure 4.7, a complete picture of the non-stoichiometry in $RbAg_4I_5$/graphite composite has been established. Unlike the conventional storage mode where the (positive and negative) extra mass is homogeneously accommodated in the bulk phase, Figure 4.8 indicates a heterogeneously mode that enable mass storage in the space charge regions. Since both $RbAg_4I_5$ and graphite are purely stoichiometric phases, the pristine composite has no stoichiometric deviation. Owing to the very low electronic defect concentration [42], $RbAg_4I_5$ itself does not to tolerate any compositional change. The stoichiometric variation only becomes possible in the boundary as long as contact with a good electronic conductor, such as graphite. As far as the silver excess is concerned, it can be realized by an interfacial defect chemistry situation (Figure 4.8): Ag^+ localizes mainly in the rigid layer of $RbAg_4I_5$ while e^- is injected into the conduction band of graphite, namely, the excess charges are accommodated at the interface. Since graphite can exhibit n- or p-type conductivity [88], the

[4] A more precise way to determine the stoichiometric potential is to coulometrically titrate the cell with capacity Q_0 until it reaches a thermodynamically self-defined potential (e.g. 0V for Ag deposition). Then the stoichiometric potential can be obtained by removing the additive Q_0 via the reversed titrations. In Figure 4.7 the potential at 0s and 6300s are very close, so we refer the stoichiometric potential to the initial open circuit potential. Note that the removal charge, i.e. from 3500 to 5400s, is slightly more than storage charge, i.e. from 750 to 2700s, so the potential at 6300s is expected higher than the potential at 0s.

$RbAg_4I_5$/graphite junction also allows for silver deficiency, which is established by V'_{Ag} on $RbAg_4I_5$ side and $h^{\cdot}$ on graphite side.

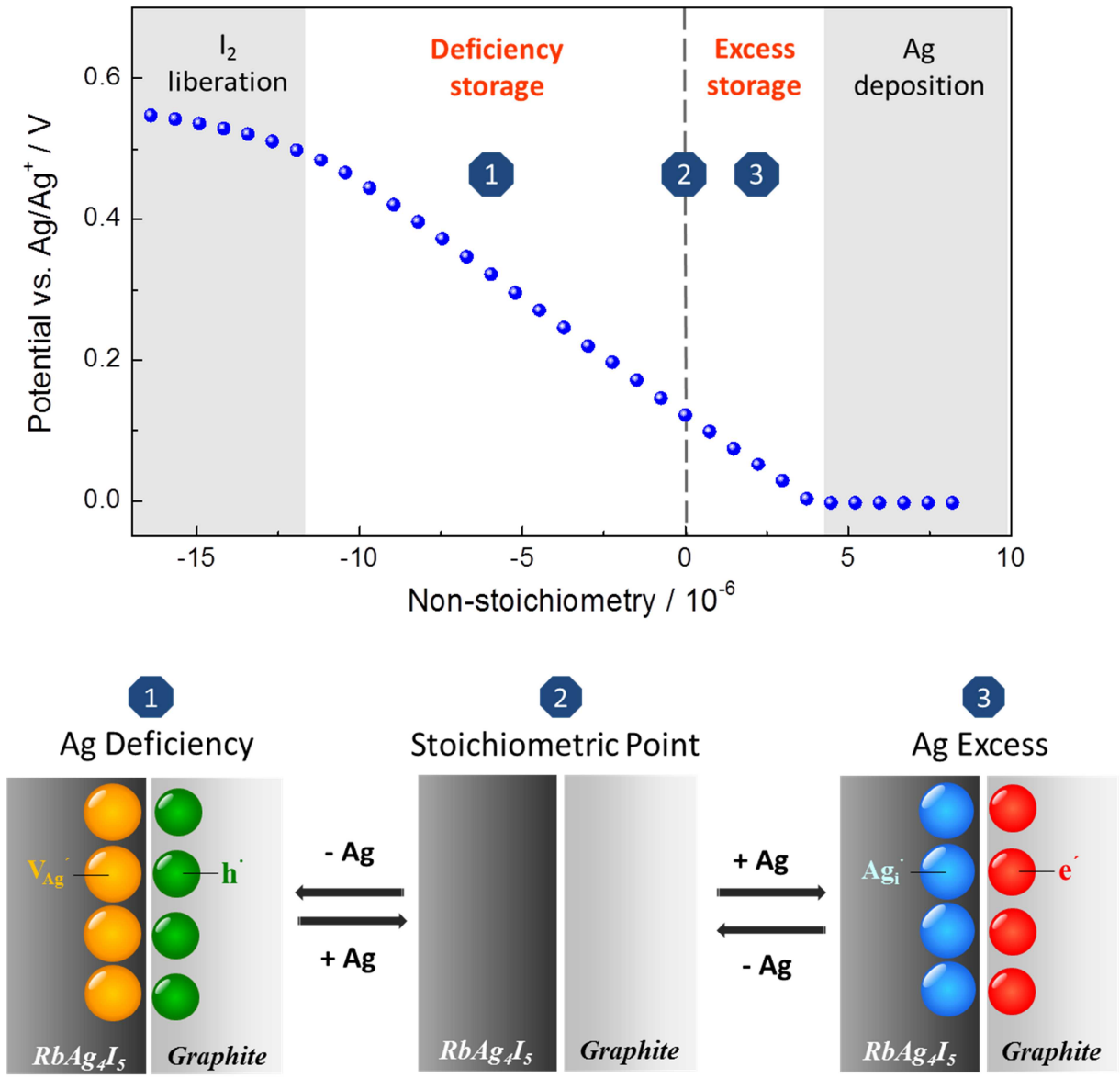

Figure 4.8 The stoichiometric variation of a $RbAg_4I_5$ /graphite composite.[5] The storage at the heterojunctions covers four regimes and in particular the Ag excess and deficiency are illustrated by the schematic.

[5] The mean molecular weight is averaged over the composite i.e. weight according to the mole fractions of the two phases.

More importantly, the rather straight titration curve covering excess and deficiency regions can be interpreted by the developed model given in Chapter 2. It suggests the shape of titration curve is determined by the mass action constants K_F and K_B. When both K_F and K_B are very high, the titration curve becomes a straight line. This is exactly the case for the junction of a superionic conductor $RbAg_4I_5$ and a good electronic conductor graphite. Since they both have very high charge carrier concentration, the screening length is ultrathin and stored charges distribute in the rigid layers of the constituting phase. The intrinsically dominated and diffusive-layer dominated modes are negligible and only the rigid layer dominated mode plays a key role in this system. The characteristic of E linearity with Q is clearly observed in $RbAg_4I_5$/graphite composites. The linear behavior also allows us to calculate the double layer capacitance of the composite electrode.

The silver removal is limited by the oxidation of iodide ion to iodine. Although the decomposition reaction of pure $RbAg_4I_5$ takes place at 0.67V [80], Hull *et al.* [74] reported that monolayer iodine may start forming above 0.46V when AgI is in contact with carbon. Our result is agreement with their finding as the titration curve bends at 0.47V.

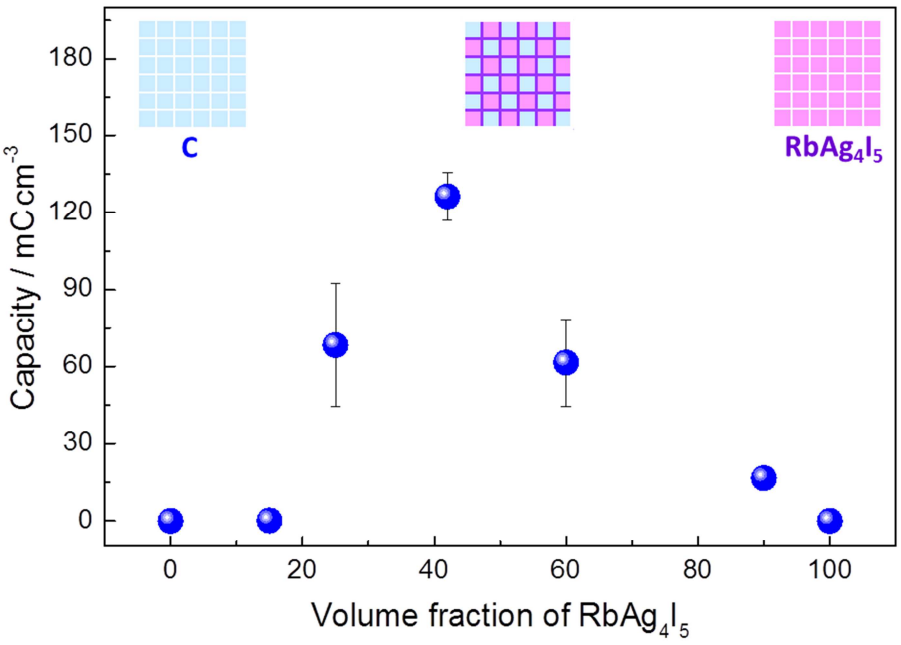

Figure 4.9 Storage capacity of $RbAg_4I_5$/graphite composites as a function of volume fraction, measured by coulometric titration between 10-400mV.

Figure 4.9 shows the dependence of storage on the $RbAg_4I_5$/graphite volume fraction. The capacity increases with the dispersion of graphite in $RbAg_4I_5$. It directly proves the nonstoichiometry occurring at the $RbAg_4I_5$/graphite contact because the storage reaches maximum at about 1:1 volume fraction. Pure $RbAg_4I_5$ and pure graphite expectedly show no non-stoichiometry (Figure 4.10a, b). To confirm the zero storage capacity of $RbAg_4I_5$ being a thermodynamic phenomenon rather than a kinetic one due to high overpotentials, the cells were charged at an extremely small current. Figure 4.10c shows that the nonstoichiometry of pure $RbAg_4I_5$ is three orders of magnitude smaller than for the composites. Note that the position of the maximum varies if different normalization is used (e.g. coulomb per gram), but the general trend remains that the capacity increases with the contact area.

Unlike conventional battery electrodes where the theoretical capacity is determined by the host materials, the maximum capacity in composites is based on the contact area. According to Figure 4.4, the BET area for graphite power is 4.26 m^2/g. Figure 4.9 shows that the maximum capacity is found for 40% volume fraction $RbAg_4I_5$, corresponding to a weight ratio of 63%. If we assume that the surface area is similar in the composite, for such a composite the total surface area of graphite is 1.6 m^2/g. Conway [54] suggested that the carbon surface can accommodate 0.18 electron/atom. This is equivalent to 1.8 electron/nm^2 if the atom density is taken as 10^{15} atom/cm^2. As far as $RbAg_4I_5$ is concerned, we assume, for an order of magnitude consideration, that the surface can accommodate 1 silver atom/nm^2, corresponding to 0.16 C/m^2. If we assume that the graphite surface is almost (so that we still have electronic percolation) completely contacted by $RbAg_4I_5$, the theoretical maximum storage (i.e. monolayer of Ag) is $1.6 \times 0.16 = 0.25$ C/m^2. Therefore, the experimental maximum capacity in $RbAg_4I_5$/graphite composites is 0.035 C/g, equivalent to 15% of a Ag monolayer.

Note that the high value of 15% refers to the local compositional change. However, the overall nonstoichiometry in Figure 4.8 ($\approx 10^{-5}$) is averaged over the composite by taking a mean molecular weight. The overall value can be significantly improved by increasing the contact area. To explore the influence of contact area on storage, the electronic conductor graphite was replaced with multi-wall carbon nanotubes (MWCNTs), because MWCNTs has similar crystalline structure of graphite but larger surface area [89]. Figure 4.11 shows that the storage of $RbAg_4I_5$/MWCNTs composites is also dependent on the volume fraction of the constituting

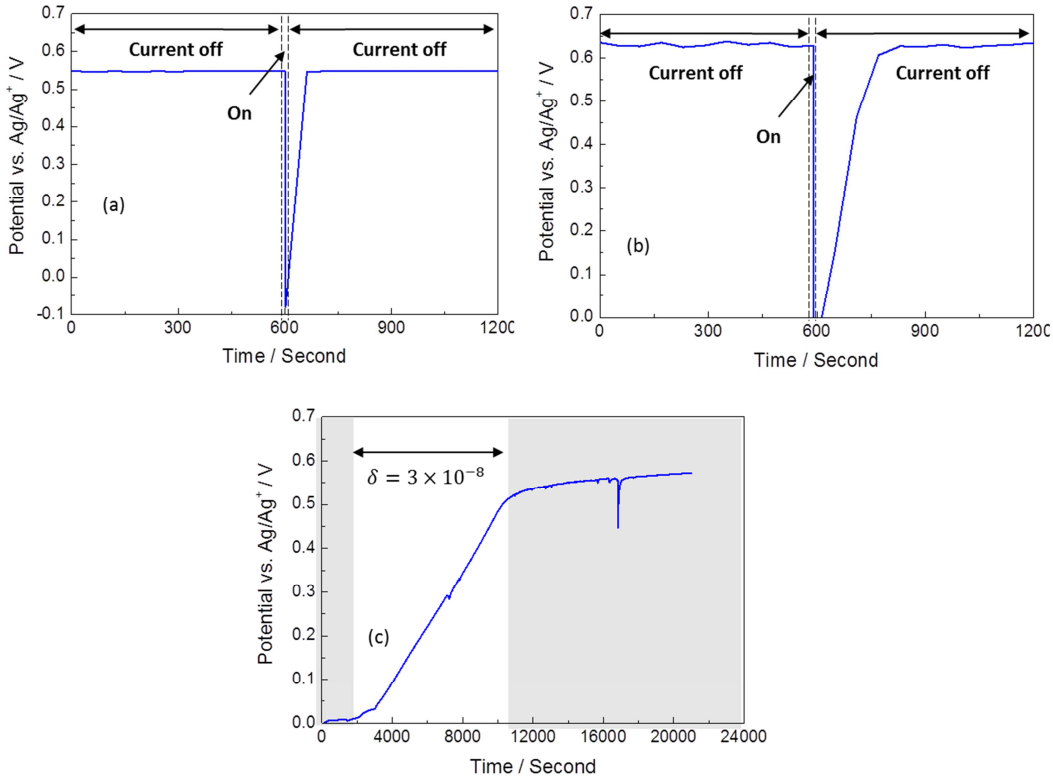

Figure 4.10 Coulometric titrations of (a) pure graphite electrode and (b) pure $RbAg_4I_5$ electrode. Upon applying a current of $10^{-5}Ag^{-1}$ the potential jumped to below 0V in 1 second, indicating negligible silver storage. (c) To confirm that the storage is a thermodynamic phenomenon, a galvanostatic charging with an extremely small current of $4 \times 10^{-10}Ag^{-1}$ was performed on pure $RbAg_4I_5$. The stoichiometric variation is only 3×10^{-8}, three orders of magnitude smaller than for the composites.

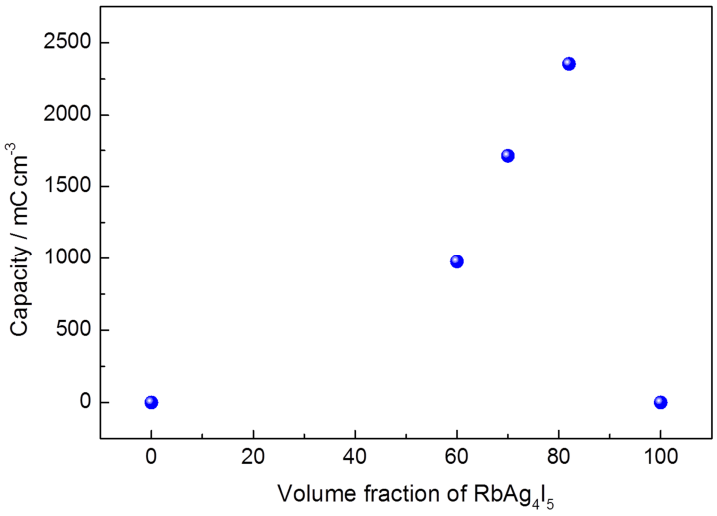

Figure 4.11 Storage capacity of $RbAg_4I_5$/ MWCNTs composites as a function of volume fraction, measured by coulometric titration between 10-400mV. At low $RbAg_4I_5$ volume fraction (<50%) densification to pellets was not successful. The point at zero $RbAg_4I_5$ volume fraction refers to graphite rod rather than MWCNTs.

phases while the capacities are orders of magnitude higher than for $RbAg_4I_5$/graphite. The increase of the maximum storage of $RbAg_4I_5$/MWCNTs composites (20 times of $RbAg_4I_5$/graphite composites) is consistent with the rise of surface area of MWCNTs (60 times of graphite). Thus, one can easily expect that the overall storage certainly can be pushed forward when the size of the two phases shrink to nano or atomic scale, i.e. mesoscopic mixed conductors. Furthermore, the maximum in Figure 4.11 appears at higher volume fraction of $RbAg_4I_5$ when compared to $RbAg_4I_5$/graphite composites. The reason may be attributed to porosity.

4.3.3 Mass transport in job-sharing composites

Besides the aspect of thermodynamics, the kinetics of the storage process is also fundamentally important. As job-sharing storage does not involve the charge transfer reactions that typically occur in conventional battery materials, the kinetics of the interfacial storage is highly favorable. Thus the rate of process is mainly determined by the rate of mass transport.

In ionic solids the motion of charge species is driven by the electrical field gradient (migration) and concentration gradient (diffusion). To measure the rate of charge carrier movement, several techniques have been applied [40, 90, 91]. A typical method is a conductivity experiment that drives ions (or electrons) within the solid by passing current through an external circuit. The ionic or electronic conductivity thus can be measured if suitable electrodes are selected (cf. reversible electrodes, blocking electrodes [92]). Another usual technique is a tracer diffusion experiment. It results from spontaneous mixing of isotopes in absence of the concentration gradient. The third method is a chemical diffusion experiment in which a species moves by virtue of a chemical concentration gradient.

In ionic crystals the term chemical diffusion specifically refers to ambipolar diffusion. It describes that the mass transport of component M needs to consider both the ionic (M^+) and electronic (e^-) motion, coupled through electroneutrality. The theoretical treatment has been comprehensively set out in literature [12, 93, 94] and experimental verification has been widely demonstrated, e.g. $LiCoO_2$ [95], Ag_2Te [96].

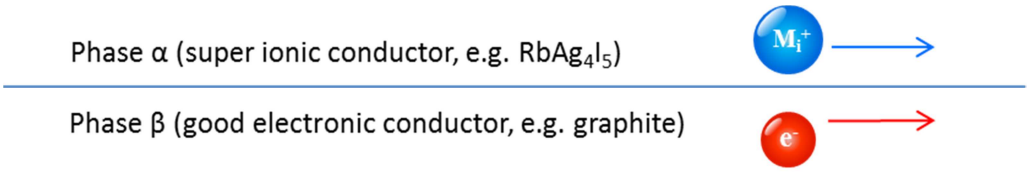

Figure 4.12. Schematic of interfacial chemical diffusion

Unlike classic chemical diffusion during which M^+ and e^- move within the homogeneous bulk phase, here we propose a novel mass transport mechanism that allows the carriers moving along the interface. More specifically, it only refers to the local movement in the space charge region. For convenience, we denote the superionic conductor (e.g. $RbAg_4I_5$) as phase α and the good electronic conductor (e.g. graphite) as phase β (see Figure 4.12).

As the mass flux of species (j) can be described in terms of the conductivity (σ) and the gradient of electrochemical potential ($\nabla\overline{\mu}$), (see references [40, 97]), one obtains

$$\text{Ion flux in phase } \alpha \qquad j_{ion}^{\alpha} = -\frac{\sigma_{ion}^{\alpha}}{F^2}\nabla\,\overline{\mu_{ion}^{\alpha}} \tag{4.1}$$

$$\text{Electron flux in phase } \beta \qquad j_{e}^{\beta} = -\frac{\sigma_{e}^{\beta}}{F^2}\nabla\,\overline{\mu_{e}^{\beta}}\,. \tag{4.2}$$

Owing to charge conservation, the flux of M

$$j_M = j_{ion}^{\alpha} = j_{e}^{\beta} \tag{4.3a}$$

and hence

$$\nabla\,\overline{\mu_{e}^{\beta}} = \frac{\sigma_{ion}^{\alpha}}{\sigma_{e}^{\beta}}\,\nabla\,\overline{\mu_{ion}^{\alpha}}\,. \tag{4.3b}$$

According to the equilibrium reaction in the space charge region,

$$M(at\ interface) \rightleftarrows M^+(phase\ \alpha) + e^-(phase\ \beta)$$

the chemical potential of M (μ_M) is equal to the sum of the electrochemical potential of ions and electrons

$$\nabla \mu_M = \nabla \overline{\mu_{ion}^{\alpha}} + \nabla \overline{\mu_e^{\beta}} = \nabla \overline{\mu_{ion}^{\alpha}} + \frac{\sigma_{ion}^{\alpha}}{\sigma_e^{\beta}} \nabla \overline{\mu_{ion}^{\alpha}} \ . \tag{4.4}$$

On substituting (4.1) and (4.4) into (4.3), the metal flux can be written as

$$j_M = -\frac{1}{F^2}\frac{\sigma_{ion}^{\alpha}\sigma_e^{\beta}}{\sigma_{ion}^{\alpha}+\sigma_e^{\beta}}\nabla \mu_M = -\frac{1}{F^2}\frac{\sigma_{ion}^{\alpha}\sigma_e^{\beta}}{\sigma_{ion}^{\alpha}+\sigma_e^{\beta}}\nabla \left(\overline{\mu_{ion}^{\alpha}} + \overline{\mu_e^{\beta}}\right). \tag{4.5}$$

For charged species, the electrochemical potential is composed of the chemical potential (μ) and the electric potential (Φ), i.e.

$$j_M = -\frac{1}{F^2}\frac{\sigma_{ion}^{\alpha}\sigma_e^{\beta}}{\sigma_{ion}^{\alpha}+\sigma_e^{\beta}}\nabla \left(\mu_{ion}^{\alpha} + F\Phi_{ion}^{\alpha} + \mu_e^{\beta} - F\Phi_e^{\beta}\right) \tag{4.6}$$

where Φ_{ion}^{α} and Φ_e^{β} is the electric potential of ion in phase α and electrons in β, respectively. In the classic chemical diffusion situation where the two species are in the same phase, the electric potential terms are equal and cancel out (i.e. $\Phi_{ion}^{\alpha} = \Phi_e^{\beta}$). Yet they are unequal in the case of interfacial mass transport. Equation (4.6) can be written as

$$j_M = -\frac{1}{F^2}\frac{\sigma_{ion}^{\alpha}\sigma_e^{\beta}}{\sigma_{ion}^{\alpha}+\sigma_e^{\beta}}\left[\frac{\partial \mu_{ion}^{\alpha}}{\partial c_{ion}^{\alpha}}\nabla c_{ion}^{\alpha} + \frac{\partial \mu_e^{\beta}}{\partial c_e^{\beta}}\nabla c_e^{\beta} + F\frac{\partial\left(\Phi_{ion}^{\alpha} - \Phi_e^{\beta}\right)}{\partial c_M}\nabla c_M\right] \tag{4.7}$$

where c_{ion}^{α} and c_e^{β} are the overall concentrations of ions and electrons in the outmost layers, and c_M refers to the concentration of M stored at interface.

In the case of superionic conductor/good electronic conductor, the space charge layers, where the excess ions and the excess electrons are located, are expected to be of atomic scale. As the degree of stoichiometric variation of c_{ion}^{α}, c_e^{β}, and c_M are equal[6], it follows

$$dc_{ion}^{\alpha} = dc_e^{\beta} = dc_M. \tag{4.8}$$

[6] The absolute value of c_{ion}^{α}, c_e^{β}, and c_M are not necessarily equal because they are dependent on the intrinsic concentration, e.g. $c_{ion}^{\alpha} = \Delta c_{ion}^{\alpha} + c_{ion,\text{intrinsic}}^{\alpha}$, where Δc_{ion}^{α} stands for the stored ion concentration.

Substituting (4.8) into (4.7), one can describe the M flux in terms of the concentration gradient of M.

$$j_M = -\frac{1}{F^2}\frac{\sigma_{ion}^{\alpha}\sigma_e^{\beta}}{\sigma_{ion}^{\alpha}+\sigma_e^{\beta}}\left[\frac{\partial\mu_{ion}^{\alpha}}{\partial c_{ion}^{\alpha}}+\frac{\partial\mu_e^{\beta}}{\partial c_e^{\beta}}+F\frac{\partial(\Phi_{ion}^{\alpha}-\Phi_e^{\beta})}{\partial c_M}\right]\nabla c_M \tag{4.9}$$

Compared with the classic chemical diffusion formula [40, 97], the third term in the bracket of (4.9) is an additional term and it originates from the electric potential over the interface. According to Gauss's law, the potential drop $(\Phi_{ion}^{\alpha}-\Phi_e^{\beta})$ over the interface region is proportional to the total stored charge at the interface (cf. reference [32] for more details). In the case of a superionic conductor/good electronic conductor, the total stored charge is simply the product of excess ion (or electron) concentration and the space charge layer thickness. Since the layer thickness and the width of interface region both are assumed to be close to the size of atoms, for the sake of simplification we equalize them and assume the corresponding value to be the separation distance of atoms (denoted as s). It yields

$$\frac{\Phi_{ion}^{\alpha}-\Phi_e^{\beta}}{s}=\frac{Fs\,\Delta c_{ion}^{\alpha}}{\bar{\varepsilon}\varepsilon_0}\,. \tag{4.10}$$

Here $\bar{\varepsilon}$ is the mean dielectric constant of the composite and $\bar{\varepsilon}\varepsilon_0$ is the absolute dielectric constant. Substituting (4.8) and (4.10) into (4.9), one can write

$$j_M = -\frac{1}{F^2}\frac{\sigma_{ion}^{\alpha}\sigma_e^{\beta}}{\sigma_{ion}^{\alpha}+\sigma_e^{\beta}}\left[\frac{\partial\mu_{ion}^{\alpha}}{\partial c_{ion}^{\alpha}}+\frac{\partial\mu_e^{\beta}}{\partial c_e^{\beta}}+\frac{F^2s^2}{\varepsilon\varepsilon_0}\right]\nabla c_M \tag{4.11}$$

If we express the chemical potential in terms of activity (a), it yields the general formula

$$j_M = -\underbrace{\frac{RT}{F^2}\frac{\sigma_{ion}^{\alpha}\sigma_e^{\beta}}{\sigma_{ion}^{\alpha}+\sigma_e^{\beta}}}_{\propto (R^{\delta})^{-1}}\underbrace{\left[\frac{1}{c_{ion}^{\alpha}}\frac{\partial\ln a_{ion}^{\alpha}}{\partial\ln c_{ion}^{\alpha}}+\frac{1}{c_e^{\beta}}\frac{\partial\ln a_e^{\beta}}{\partial\ln c_e^{\beta}}+\frac{F^2s^2}{RT\varepsilon\varepsilon_0}\right]}_{\propto (C^{\delta})^{-1}}\nabla c_M \tag{4.12}$$

$$= -D^{\delta}\,\nabla c_M$$

Note that the third term in the bracket of (4.12) is a constant with regard to concentration and thus makes an additional contribution to the chemical diffusion. One may notice that (4.12) is a

typical formula of Fick's law, which describes the proportionality of the molar flux and the concentration gradient. The pre-factor is defined as the chemical diffusion coefficient D^{δ}. The corresponding equivalent circuit contains two elements: one resistor and one capacitor [98].[7] The first one, so called chemical resistance (R^{δ}), is composed of contributions from both ionic and electronic conductivities. It determines the permeation rate of a component at steady state. On the other hand, the transient behavior is characterized by the other element, the chemical capacitance (C^{δ}). It measures the ability to take up or release chemical components such as oxygen, hydrogen, lithium, silver etc. Since the equivalent circuit of chemical diffusion contains these two elements, the chemical diffusivity D^{δ} is inversely proportional to the product of $R^{\delta}C^{\delta}$. Equation (4.12) shows the respective definition of R^{δ} and C^{δ} in chemical diffusion. If the charge carrier concentrations are dilute, $a_{ion}^{\alpha} \approx c_{ion}^{\alpha}$, $a_{e}^{\beta} \approx c_{e}^{\beta}$, it yields a simpler formula.

$$j_M = -\underbrace{\frac{RT}{F^2}\frac{\sigma_{ion}^{\alpha}\sigma_{e}^{\beta}}{\sigma_{ion}^{\alpha}+\sigma_{e}^{\beta}}}_{(R^{\delta})^{-1}}\underbrace{\left[\frac{1}{c_{ion}^{\alpha}}+\frac{1}{c_{e}^{\beta}}+\frac{F^2 s^2}{RT\varepsilon\varepsilon_0}\right]}_{(C^{\delta})^{-1}}\nabla c_M \qquad (4.13)$$

$$= -D^{\delta}\,\nabla c_M$$

Table 4.1 summarizes the chemical diffusion coefficient in terms of chemical resistance R^{δ} and chemical capacitance C^{δ}. Unlike the classic chemical diffusivity where the ionic and electronic properties are referring to the same phase, the job-sharing chemical diffusivity benefits from the separate properties of constituting phases. Moreover, the chemical capacitance of the job-sharing diffusivity has an additional term characterized by the electrostatic force. This term is independent of charge concentrations and only consists of several physical parameters. As we will show later, it will suppress the chemical capacitance and significantly boost the mass transport rate.

[7] If we take a mixed conductor with low ionic conductivity and low electronic concentration as an example, the chemical resistance (R^{δ}) is approximately $\frac{1}{\sigma_{ion}}(\frac{L}{A})$, where L and A are the length and the cross section area. On the other hand, if neglecting the activity coefficient, the corresponding chemical capacitance (C^{δ}) is $\frac{F^2}{RT}c_e(LA)$. The time constant ($= R^{\delta}C^{\delta}$) is the typical formula $\frac{L^2}{D^{\delta}}$. See more details in Appendix IV.

Table 4.1: Comparison of chemical resistance (R^{δ}) and chemical capacitance (C^{δ}) of classic and "job-sharing" chemical diffusion coefficient.

	$D^{\delta} = \frac{RT}{F^2}(R^{\delta}C^{\delta})^{-1}$	
	$(R^{\delta})^{-1}$	$(C^{\delta})^{-1}$
Classic bulk chemical diffusion Ag_2S, $LiFePO_4$, $SrTiO_3$, etc.	$\frac{\sigma_{ion}\sigma_e}{\sigma_{ion}+\sigma_e}$	$\frac{1}{c_{ion}}\frac{\partial \ln(a_{ion})}{\partial \ln(c_{ion})}+\frac{1}{c_e}\frac{\partial \ln(a_e)}{\partial \ln(c_e)}$
"Job-sharing" chemical diffusion **α/β** = $RbAg_4I_5$/graphite	$\frac{\sigma_{ion}^{\alpha}\sigma_e^{\beta}}{\sigma_{ion}^{\alpha}+\sigma_e^{\beta}}$	$\frac{1}{c_{ion}^{\alpha}}\frac{\partial \ln(a_{ion}^{\alpha})}{\partial \ln(c_{ion}^{\alpha})}+\frac{1}{c_e^{\beta}}\frac{\partial \ln\left(a_e^{\beta}\right)}{\partial \ln\left(c_e^{\beta}\right)}+\frac{F^2s^2}{RT\varepsilon\varepsilon_0}$

$\boldsymbol{\sigma}, \boldsymbol{c}$: conductivity, concentration
Subscript: $\boldsymbol{ion}, \boldsymbol{e}$: ion and electron properties
$\boldsymbol{s}$: separation distance of the atoms

4.3.4 Chemical diffusion coefficient obtained from coulometric titration

The chemical diffusion coefficient is a key parameter in mixed ionic-electronic conductors because it measures, at given geometry and driving force, the rate at which the chemical diffusion occurs [99]. Coulometric titration technique is generally used to measure the chemical diffusivity in mixed conductors. By using the corresponding experimental data from polarization [100] or depolarization [90], the effective D^{δ} can be obtained according to the transient voltage change with time. In the short time regime[8], the cell voltage changes linearly with the square root of time, while in the long time regime it changes with time exponentially [90, 101-103].

Figure 4.13 shows the chemical diffusivity D^{δ} measured from the coulometric titration experiment. The D^{δ}-value varies with the non-stoichiometry. This phenomena is commonly observed in mixed conductors and can be explained in terms of defect chemistry [93, 96]. As we

[8] The time constant τ is equal to to $\aleph\frac{L^2}{D^{\delta}}$. The pre-factor $\aleph$ slightly varies due to different boundary conditions, i.e. blocking electrode only on one side or on both sides of the cell electrode, cf. references [90, 101]. Typically the short time regime refers to $t < \tau$ and the long time regime to $t > \tau$.

will show in the following, the experimental D^{δ} can by explained by our job-sharing chemical diffusion model developed in section 4.3.5. It is worth mentioning that the bulk percolation is insignificant as in previous section TEM image shows the $RbAg_4I_5$ thin film characteristic on graphite surface. The observed chemical diffusion thus set the lower limit of the mass transport rate.

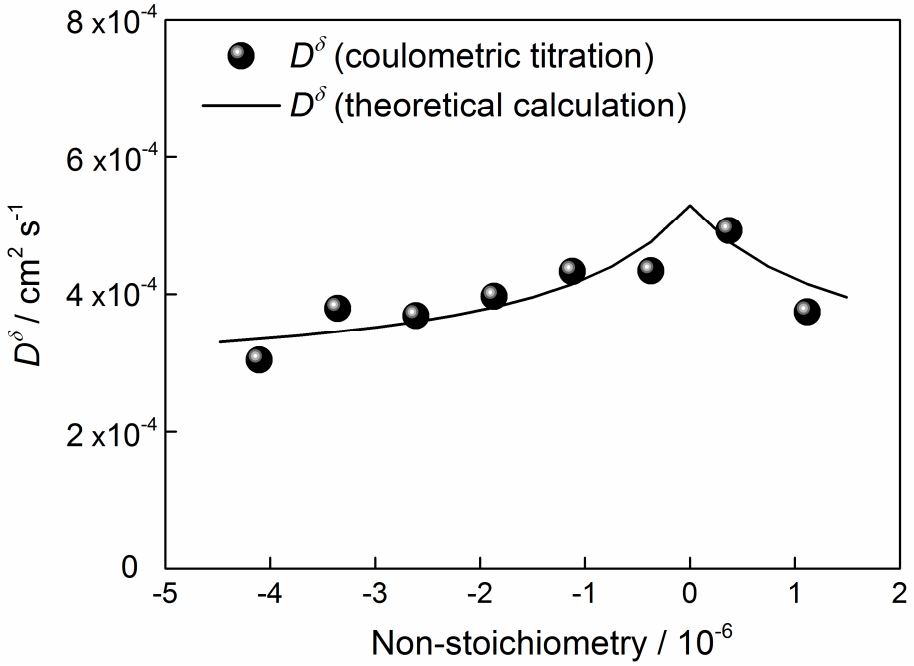

Figure 4.13. Comparison of D^{δ}-values obtained from titration experiment and theoretical calculations.

4.3.5 Theoretical calculation of chemical diffusion coefficient D^{δ}

In equation (4.12) the chemical diffusivity consists of two components: chemical resistance and chemical capacitance. This type of heterogeneous chemical diffusion relies on the physical properties of the constituting phases. As long as the required physical parameters are known, one can calculate the chemical diffusivity.

- Calculation of the inverse of chemical resistance $(R^{\delta})^{-1}$

  $\sigma_{ion}^{\alpha} = 0.27\ S/cm$ (Ref. [104]) and $\sigma_{e}^{\beta} = 1250\ S/cm$ (Ref. [71]). The inverse of chemical resistance ($\frac{\sigma_{ion}^{\alpha}\sigma_{e}^{\beta}}{\sigma_{ion}^{\alpha}+\sigma_{e}^{\beta}}$) is calculated to be $0.27\ S/cm$. The value is equal to σ_{ion}^{α} simply because σ_{e}^{β} is orders of magnitude higher than σ_{ion}^{α}.

- Calculation of the inverse of chemical capacitance $(C^{\delta})^{-1}$

  ❖ *Ionic carrier concentration contribution* $\frac{1}{c_{ion}^{\alpha}}\frac{\partial \ln a_{ion}^{\alpha}}{\partial \ln c_{ion}^{\alpha}}$

  The value of c_{ion}^{α} is calculated from the silver ion concentration of $RbAg_4I_5$, which is consistent with reference [76]. The high ionic concentration (~19M) results in a very small $\frac{1}{c_{ion}^{\alpha}}$. If we consider the activity coefficient for such high concentration case, the contribution from ionic carrier $\frac{1}{c_{ion}^{\alpha}}\frac{\partial \ln a_{ion}^{\alpha}}{\partial \ln c_{ion}^{\alpha}}$ will become even more marginal[9]. It is worth mentioning that c_{ion}^{α} is almost independent of the non-stoichiometry in excess/deficiency regime, owing to its intrinsic value being much higher than the amount of silver ion added/removed.

  ❖ *Electronic carrier concentration contribution* $\frac{1}{c_{e}^{\beta}}\frac{\partial \ln a_{e}^{\beta}}{\partial \ln c_{e}^{\beta}}$

  Graphite inevitably contains some amounts of lattice defects and impurities, so the concentration of electric carriers in graphite is strongly dependent on the defect chemistry. The effects are more severe for the graphite surfaces. Several kinds of defects, e.g. adsorbed molecules, carbon interstitial/vacancy, grain boundaries, lead to carrier density variations [105-107]. Since the intrinsic electric carrier concentration in graphite is not as high as the intrinsic ionic carrier in $RbAg_4I_5$, c_{e}^{β} varies with the non-stoichiometry. The minimum number of c_{e}^{β} occurs at the stoichiometric point. When the coulometric titration is performed, the total number of electric charge carriers (i.e. electrons + holes) increases and thus reduces the term $\frac{1}{c_{e}^{\beta}}$. Note that the concentration here refers to the local

[9] For concentrated situation, the a_{ion}^{α} value strongly deviates from c_{ion}^{α}. The pre-factor is activity coefficient.

concentration in the space charge region rather than to the bulk region. The variation of c_e^{β} upon coulometric titrations can be obtained as long as the contact area of composites (by BET measurement) is known and the monolayer assumption is made.

- *Electric potential contribution* $\frac{F^2 s^2}{RT\varepsilon\varepsilon_0}$

  The term $\frac{F^2 s^2}{RT\varepsilon\varepsilon_0}$ originates from the electrostatic potential over the interface. Unlike the other two concentration-dependent terms in (4.12), this term is only determined by fixed physical parameters. The mean dielectric constant is obtained by averaging the dielectric constants of components [108-110]. The corresponding value of *s* is estimated from the data suggested in literature [72, 111].

4.3.6 Discussion of chemical diffusion coefficient D^{δ}

As already shown in Figure 4.13, the calculated D^{δ} is in a nice agreement with the experimental data. The ultrahigh D^{δ} values can be traced both to the very low chemical resistance (R^{δ}) and the very low chemical capacitance (C^{δ}).

$RbAg_4I_5$ is a superionic conductor with high ionic conductivity and extremely low electronic conductivity. The sluggish conductivity of electrons limits the movement of neutral silver and leads to the very slow chemical diffusion [112]. Owing to graphite being the adjacent phase, the electrons are allowed to reside and move on the graphite side of the interface. The silver transport thus is significantly enhanced. Because the electronic conductivity of graphite (σ_e^{β}) dominates the ionic conductivity of $RbAg_4I_5$ (σ_{ion}^{α}), the rate-determining step for the chemical resistance (R^{δ}) of $RbAg_4I_5$/graphite composites is the silver ionic conductivity on the $RbAg_4I_5$.

The low chemical resistance is not enough to achieve such an ultrafast chemical diffusion. Another favorable factor is the low chemical capacitance. Figure 4.13 illustrates the calculated D^{δ} as a function of non-stoichiometry. The D^{δ} data from the titration experiment can be well-

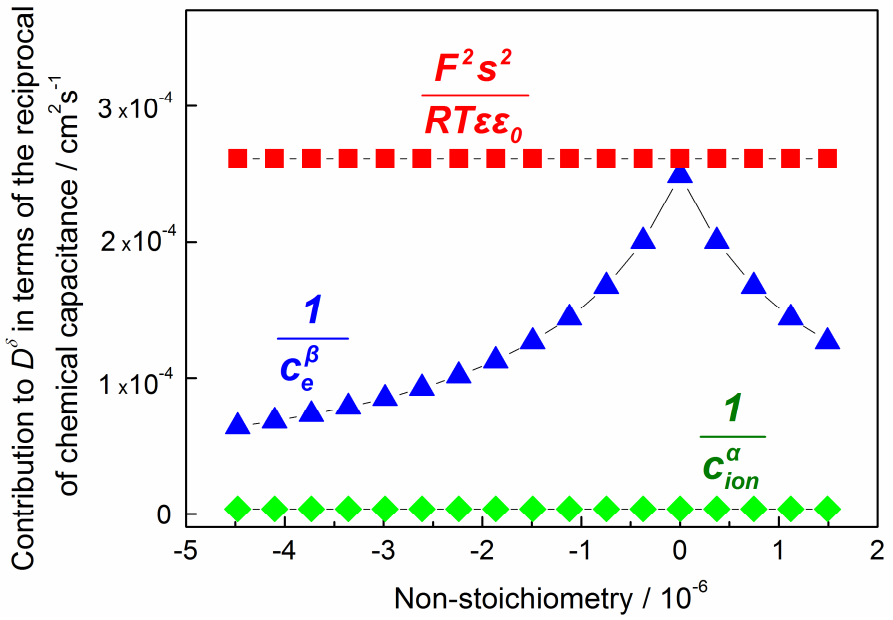

Figure 4.14 Contributions of various capacitive terms to the chemical diffusion coefficient. The characteristic term resulting from the electrostatic field effect is dominant and pushes the chemical diffusion in the composite to unprecedentedly high values.

explained by our job-sharing model. The maximum value occurs at the stoichiometric point, where c_e^β has lowest number.[10]

With the increase of non-stoichiometry, D^δ slightly drops and approaches a constant value. To discuss the behavior, it is necessary to separately analyze the contribution of each component term in $(C^\delta)^{-1}$ (see Figure 4.14). Owing to the extremely high Ag^+ concentration in $RbAg_4I_5$, $\frac{1}{c_{ion}^\alpha}$ is always marginal over the non-stoichiometry range. On the other hand, c_e^β varies with the addition/removal of silver. At the stoichiometric point where the numbers of electrons and holes are equal, c_e^β has its least value and hence $\frac{1}{c_e^\beta}$ is at maximum. As soon as excess electrons or holes are injected into graphite, $\frac{1}{c_e^\beta}$ quickly decays, e.g. the value is half of highest when

[10] Note that c_{ion}^α and c_e^β respectively refer to the total number of ionic defect and electronic defect concentration. Apart from the stoichiometric point, the silver storage leads to the increase of electrons and interstitial ions while the silver removal leads to the increase of holes and silver vacancies. The minimal c_e^β (and c_{ion}^α) occurs at the stoichiometric point where the concentration of electron and hole (and interstitial and vacancy) are equal. An analogous mathematical problem is if xy =constant then $(x+y)$ has minimum when $x=y$.

$\delta=1.5\times10^{-6}$. This is the reason why a hump is observed around the stoichiometric point in Figure 4.13. The most important contribution to the anomalously fast chemical diffusion is made by the term owing to the electrostatic field effect $\frac{F^2s^2}{RT\varepsilon\varepsilon_0}$. This characteristic term of job-sharing mechanism is independent of non-stoichiometry and dominates the others. As C^δ stands for the ability to take up or release chemical components, the appearance of the electrostatic term significantly suppresses C^δ and hence speeds up the chemical diffusion. Thermodynamically the built-in potential tends to avoid charge variation when they move along the interface.[11] In view of this, the chemical diffusion in such an "artificial" mixed conductor is faster than in a classic mixed conductor, even if exhibiting the same ionic and electronic conductivities.[12]

Electrochemical devices, such as fuel cells and batteries, require mixed conductors conveying ions and/or electrons, so it is tempted to find out mixed conductors with promisingly mass (or charge) transport. Conventional methods, e.g. doping, focus on tuning the bulk properties of the materials, but they are limited by the intrinsic characteristic of materials. Here the synergistic concept of "job-sharing" mechanism offers one more degree of freedom for designing mixed conductors. As demonstrated above, an artificial mixed conductor comprising a very good ionic and a very good electronic conductor can achieve excellent mass transport, due to not only low chemical resistance but also low chemical capacitance. Therefore the finding of the present study may open a new class of novel materials in the applications of energy storage and energy conversion.

4.3.7 Silver permeation membrane

Mass transport through the mixed conductors is of significant interest in solid state ionics. One important application is solid membranes that are used to separate different species. Taking

[11] Otherwise, the filling charges will accumulate at the interface, leading to an increase of the electrostatic potential.

[12] The conductivity σ is proportional to the product of mobility u and charge carrier concentration c. For a classic mixed conductor, $D^\delta \propto \frac{\sigma_{ion}\sigma_e}{\sigma_{ion}+\sigma_e}\left[\frac{1}{c_{ion}}+\frac{1}{c_e}\right]$. If we assume the mixed conductor with the property ($\sigma_{ion} \ll \sigma_e$ and $c_{ion} \gg c_e$), the above expression approximately turns out to be $D^\delta \propto \sigma_{ion}\left[\frac{1}{c_e}\right]$. As long as $\frac{F^2s^2}{RT\varepsilon\varepsilon_0}$ dominates $\frac{1}{c_e}$, the interfacial mass transport is anyway faster than the classic mass transport.

oxygen permeation membrane as an example, the separation of oxygen can be achieved by a ceramic membrane permeating only oxygen but no other species [113]. Besides the technology aspects, the permeation membrane technique also allows evaluating the mass transport rate. Since the movement of oxygen relies on the ambipolar motion of oxide ions and electrons, the permeation rate is directly related to the chemical diffusion of oxygen. As long as the permeation mass flux is measured, it is able to calculate the D^{δ} values.

Different from steady-state measurements, the methods involving transient concentration gradients allow us to monitor the dynamic concentration change. Such methods have been used to determine the D^{δ} value of oxygen in ceramic membranes [114-116]. By suddenly creating a constant concentration on one side of the electrode, the chemical species will diffuse though the electrode (Figure 4.15**).** As the species needs some time to convey and reach the sensing point, the signal shows a characteristic time delay τ. As long as the diffusion length and the time delay are known, one can calculate the D^{δ} of the mixed conductor [115].

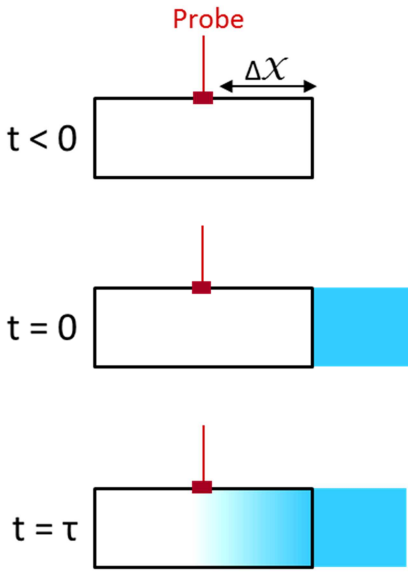

Figure 4.15 Concentration build-up at position Δx within the electrode. After a constant concentration of component (e.g. Ag) is suddenly imposed on the outer side of the electrode (bule square) at $t = 0$, the component will diffuse into the electrode. At $t = \tau$ the sensing probe detects the concentration variation and the corresponding time delay can be used to evaluate the chemical diffusivity.

In the present study, we used Pt electrode to probe the local silver concentration. The electromotive force (emf) indicates the chemical potential difference between working electrode and silver electrode. Since the chemical potential is a function of silver concentration, the rate of diffusion can be obtained by observing the emf change. The configuration of the experiment is depicted in Figure 4.16. Before the Ag source is applied, the concentration within the working electrode is c_0. As soon as the electrode is contacted by Ag on the outer side, the concentration at $x = L$ suddenly becomes c_L. Moreover, due to its very low electronic conductivity, $RbAg_4I_5$ is impermeable for Ag.

The silver concentration c_{Ag} can be solved by Fick's second law

$$\frac{\partial c_{Ag}}{\partial t} = D^{\delta} \frac{\partial^2 c_{Ag}}{\partial x^2} \tag{4.14}$$

The boundary and initial conditions are

$$\frac{\partial c_{Ag}(0,t)}{\partial x} = 0 \tag{4.15}$$

$$c_{Ag}(L,t) = c_L \tag{4.16}$$

$$c_{Ag}(x,0) = c_0 \tag{4.17}$$

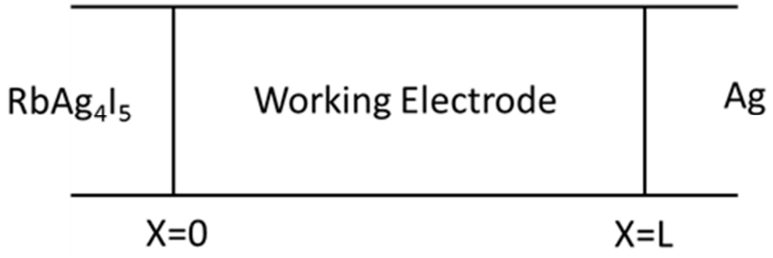

Figure 4.16. Schematic of the configuration of silver permeation experiment. At $t = 0$, the silver concentration at $x = L$ has instantaneously jumped from C_0 to C_L.

As long as c_{Ag} is solved [117], the effective chemical diffusion coefficient can be calculated by analyzing the emf response [118]. To demonstrate the superior chemical diffusion for the composites, here we also perform the permeation experiments on silver chalcogenides, as the representative of conventional mixed conductors. Silver chalcogenides exhibit very high chemical diffusivity in the superionic phase, due to the significantly cationic structural disorder [9, 79, 119]. However, the rate of mass transport drops substantially when the temperature is below the transition point.

Figure 4.17 compares the permeation rate for the $RbAg_4I_5$/graphite composites and the silver chalcogenides at room temperature. The emf of working electrode (vs. Ag/Ag^+) was stable before the permeation experiment. At t = 100 min a silver pellet was contacted on the outer side of the working electrode. As a source of constant concentration of silver, the silver pellet supplies a continuous concentration gradient driving silver through the electrode. Once the silver has moved the distance $\frac{1}{2}L$, the probe will sense the emf change. In Figure 4.17 the silver chalcogenides do not sense any emf change even after 2 hours while the $RbAg_4I_5$/graphite composite exhibits a very quick response. The invariant emf of silver chalcogenides indicates that the D^{δ} values at room temperature are very small. On the other hand, the short delay time of the composites allows us estimating D^{δ}. As mentioned in section 4.2.6, it usually takes about one minute to reconnect the measurement setup. As soon as the emf measurement was switched on, we observed that the emf transition for $RbAg_4I_5$/graphite composite already finished.

To estimate the D^{δ} from the permeation experiment, it is necessary to correlate the transient emf change with the time upon contacting the silver source. Preis and Sitte [118] suggested the solution of emf as a function of component concentration. As long as the concentration $c_{Ag}(\frac{L}{2}, t)$ is substituted into the solution, one can obtain the emf function and thus extract the effective D^{δ} from the experiment. Since the time delay for the composites is shorter than the reconnection of experiment setup, the lower limit of D^{δ} can be extracted if taking one minute as the time delay. The corresponding D^{δ} value ($\approx 5\times10^{-5}$ cm^2/s) confirms that the chemical diffusion is highly favorable. To track the rapid transient of the emf variation, the future work aims to carry out an *in-situ* experiment without interrupting the emf observation.

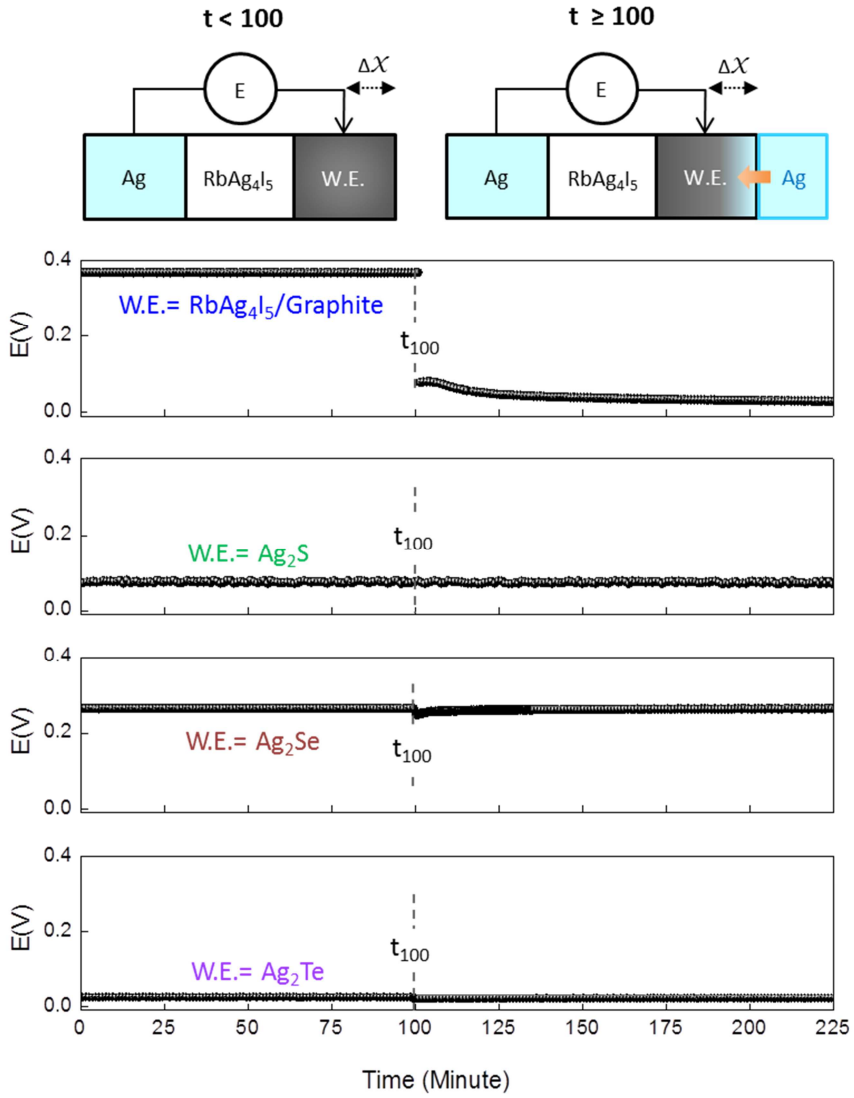

Figure 4.17 Ag permeation experiment. At t =100 min, the working electrode (W.E.) is suddenly contacted by silver. In the case of the $RbAg_4I_5$/graphite composites, the electromotive force (E) approaches zero very quickly. The comparison with silver chalcogenides shows that even after 2 hours the E value has not changed.

The obtained D^{δ} for the $RbAg_4I_5$/graphite composites have been summarized in Table 4.2. The experimental value, either by coulometric titration (electrochemical method) or permeation (chemical method), is in an agreement with the theoretical prediction. The corresponding values are at least three orders of magnitude higher than pure $RbAg_4I_5$ and even over NaCl in liquid water. A more detailed discussion will be shown in section 4.3.10.

Table 4.2: Comparison of chemical diffusion coefficients D^{δ} at 25°C

$RbAg_4I_5$/graphite composites			$RbAg_4I_5$	NaCl in water
Coulometric titration	Ag permeation	Calculation	Ref.[112]	Ref.[120]
30~50	> 5	30~60	0.0017	1.6

Values in $10^{-5}\ cm^2/s$.

4.3.8 All-solid-state battery

Another important application of mixed conductors is battery electrodes. The rate which one battery can be charged is usually limited by the mass transport of the electrode materials [87]. For instance, a lithium based battery typically cannot be charged in several minutes because of the low lithium diffusivity of the electrode [121]. To overcome the intrinsic barrier, nanostructuring the materials in the form of nanodots (0D) [122], nanowires (1D) [123], or nanosheets (2D) [124] have been widely developed. Since the diffusion time is proportional to the square of diffusion length [40], the reduction of the size of electrode materials indeed substantially enhance the rate performance.

Unlike conventional approach by shirking the diffusion length, the present work aims to improve the rate performance by enhancing the chemical diffusivity according to the job-sharing mechanism. Figure 4.18 shows the galvanostatic charge/discharge curves of a silver all-solid-state battery. Here $RbAg_4I_5$ serves as solid electrolyte as well as the component of electrode. The rather linear charge/discharge behavior is consistent with that in coulometric titration experiments. In the language of battery research, an index to evaluate the rate performance is C rate. A rate of n C denotes the rate at which a full charge or discharge takes 3600/n seconds, e.g. it takes one hour for 1 C. Figure 4.18 shows that using the above composite as electrode, the battery can be charged at very high rate. The reversible capacity still retains even at the extreme charging rate of 1240C (corresponding to charge/discharge within 2.9 seconds). The operating potential range includes silver excess and deficiency, so the excellent performance shows the

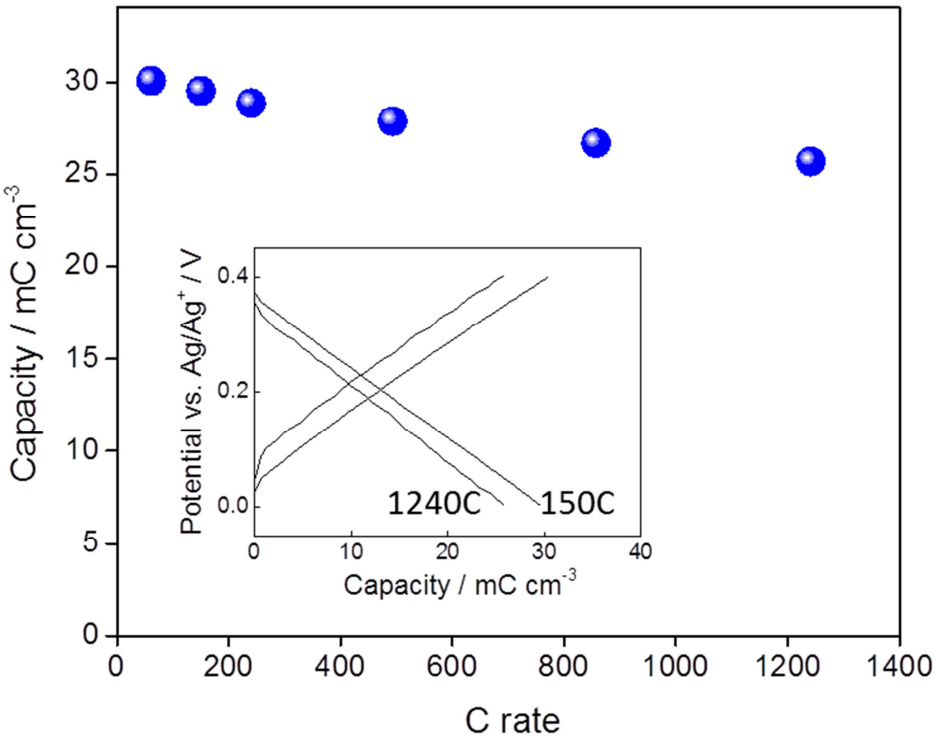

Figure 4.18 Ultrafast rate performance for a silver all-solid-state battery. The cell is galvanostatically charged/discharged between 0.01-0.4 V.

silver storage/removal is very fast. The rapid process is attributed to good electronic/ionic conductivities as well as to ultrahigh chemical diffusion. The latter turns out to be particularly important in the heterogeneous systems because it facilitates the redistribution of silver within the composite electrodes.

Technologically the all-solid-state batteries have several advantages in the application of energy storage. They are structurally robust and could be operated in a wide temperature range [125]. The cells composed of our composite electrodes are able to be charged at very high rate. As the stoichiometric variation occurs at the interfaces, the capacity naturally increases with the contact area. Therefore shrinking the size of carbon and $RbAg_4I_5$ could effectively improve the storage capacity. A good candidate could be composites of graphene and $RbAg_4I_5$, generating two-dimensional heterostructures.

4.3.9 All-solid-state supercapacitor

Supercapacitor technology is a key technology for rapid energy storage. The conventional working principle is to store the ionic charges, where are dissociated from the liquid electrolyte, on the surface of two symmetric electrodes. To hold the local electroneutrality, the dissociated cations and anions are respectively compensated by the electrons and holes formed on the electrodes. The storage capacity is limited by two factors: (i) thermodynamically the maximum capacity is determined by the total amount of dissociated ion-pairs in the electrolyte, so for electrodes with high surface area the cell may require a large electrolyte volume. (ii) Kinetically at high rates the concentration polarization in the electrolyte becomes severe, which limits the rate performance of the supercapacitors. Based on job-sharing storage mechanism, we present a new type of all-solid-state supercapacitors composed of $RbAg_4I_5$/graphite composites (electrode) and $RbAg_4I_5$ (electrolyte). Since $RbAg_4I_5$ is a cationic solid conductor that only allows the motion of Ag^+, the concentration polarization will not occur. Unlike conventional supercapacitors, the storage of the all-solid-state system relies on the local nonstoichiometry at the interface of composite electrodes. Here one realizes silver excess (interstitials on the $RbAg_4I_5$ side, electrons on the graphite side) on one side of the cell and silver deficiency (vacancies on $RbAg_4I_5$ and holes on graphite) on the other. Since $RbAg_4I_5$ electrolyte is only responsible for ionic transport, its volume (thickness) does not influence the total storage. Moreover, the atomic length of screening layer makes the cells kinetically favorable.

One useful method to evaluate the rate performance of a supercapacitor is the analysis of frequency dependence on capacitance. For a symmetric type supercapacitor, typically the equivalent circuit contains one resistance and one capacitor. An alternative approach is to consider the whole systems as a complex capacitance [78]. Thus, by using the impedance data, it yields the real (C') and imaginary (C'') part of the capacitance

$$C'(\omega) = \frac{-Z''(\omega)}{\omega|Z(\omega)|^2} \tag{4.18}$$

$$C''(\omega) = \frac{Z'(\omega)}{\omega|Z(\omega)|^2} \tag{4.19}$$

where ω is the frequency. $Z'$and Z'' stand for the real and imaginary part of the impedance data.

Figure 4.19 shows the evolution of complex capacitance as a function of frequency. The low frequency value of C'corresponds to the capacitance of galvanostatic charge/discharge. The maximum of the imaginary part at 25 Hz is used to define a characteristic time constant τ (= 1/25 = 40ms). This time constant, referring to the relaxation time of the cell [78], indicates that half of the low frequency C' still retains at τ. In Figure 4.19, the 40 ms relaxation time suggests that the silver addition/removal process is extremely fast and almost as high as recently reported values for liquid systems [126].

It is worth mentioning that in addition to charge transport to the interface the chemical diffusion in all-solid-state cells may play a crucial role wherever percolation is not ideal. Unlike in liquid systems, the mass transport in solid systems strongly relies on the solid-solid contact situation. Besides the necessarily quick polarization of the ionic conductor/electronic conductor interface, the rapid mass transport along the interface and hence the fast silver redistribution is also required. To unify the mass transport in the highly dimensional problem, numerical

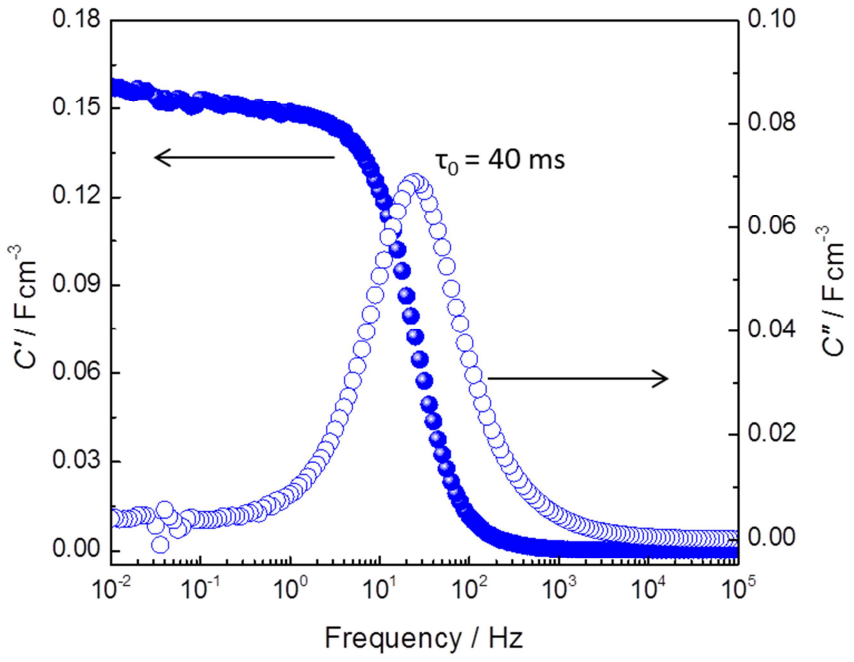

Figure 4.19 Ultrafast performance for all-solid-state supercapacitor. The frequency dependence of the real and imaginary part of capacitance (C' and C'') shows an extremely short relaxation time of 40ms.

investigations such as finite element simulation are necessary. Jamnik and Maier [98] developed a general transmission line model for charge and mass transport in mixed conductor. The corresponding equivalent circuits consist of unified "electrochemical resistors" and "electrochemical capacitors". Such type of study in the heterogeneous systems has not been explored and will be the scope of future works on the artificial mixed conductors.

4.3.10 Comparison of chemical diffusion coefficients for various materials

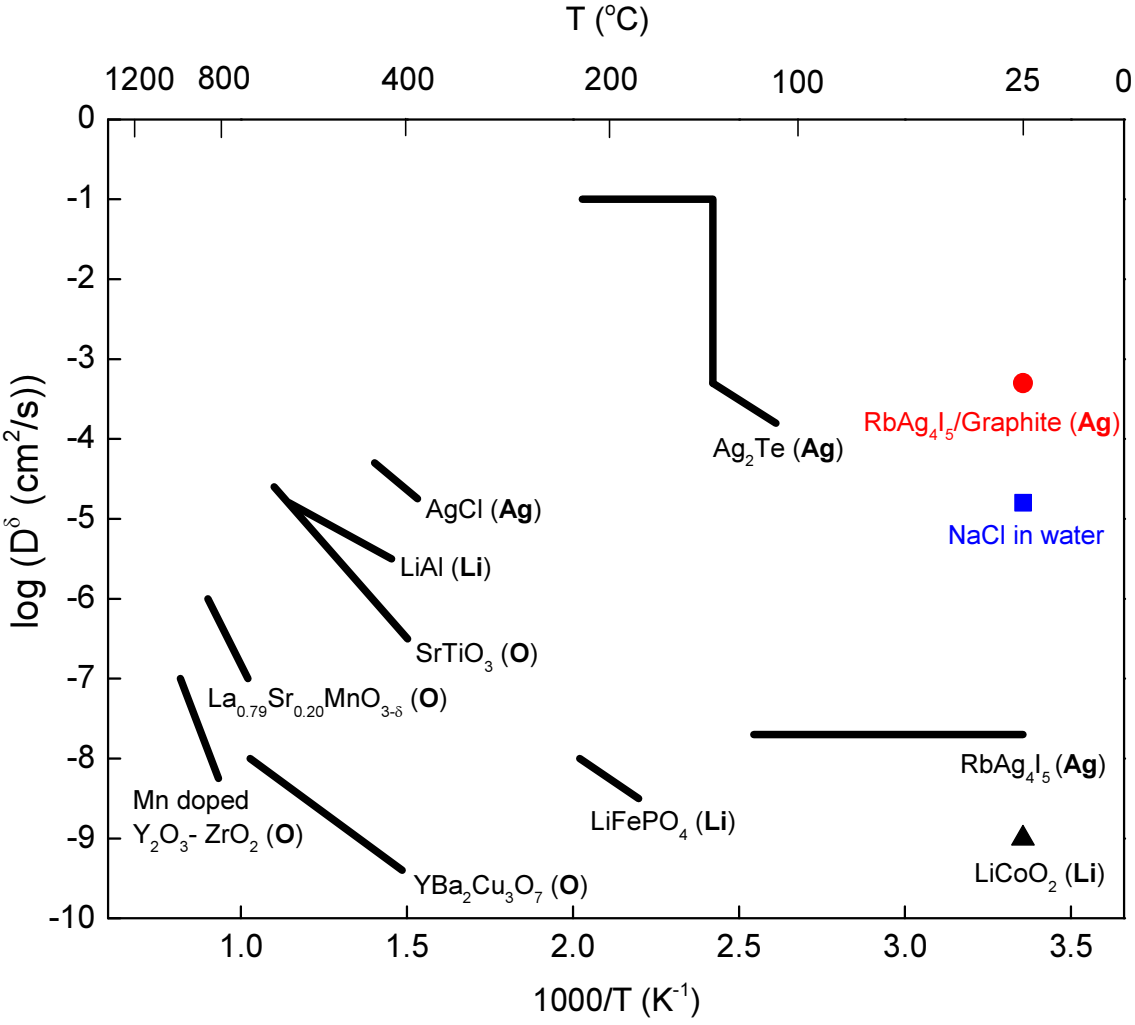

Figure 4.20 Comparison of chemical diffusion coefficients for different materials. The D^δ values for other materials are taken from [96, 112, 120, 127-135].

Chemical diffusion coefficients are the characteristic parameters of mass transport. Figure 4.20 shows a diffusivity map for different materials. Owing to their low diffusivity, oxygen mixed conductors are usually measured at temperature above 400°C. The superconductor $YBa_2Cu_3O_7$ (YBCO) has very high electronic conductivity [135], but the transport of oxide ions is sluggish and thus significantly drags the motion of oxygen. Another extreme case is Y_2O_3-ZrO_2 (YSZ), the state-of-art solid electrolyte with high ionic conductivity but low electronic conductivity [132, 136]. To facilitate the electronic motion, a doping of 9.5% of Mn has been reported an considerably enhancement of D^δ [137].

Room temperature D^δ-values are usually very low. This is also true for Li-electrode materials, e.g. $LiCoO_2$, which is due to low conductivities and high chemical capacitances. Ag_2Te is one of the mixed conductors having highest D^δ value after experiencing a phase transition about 140°C [79]. In high temperature phase, its D^δ does not strongly change with temperature and shows a plateau in Figure 4.20. $RbAg_4I_5$ is a superionic conductor with highest ionic conductivity at room temperature. Yet, as a good solid electrolyte, the extremely low electronic conductivity leads to the relatively sluggish sliver transport. As already demonstrated in previous sections, the synergistic concept of mixing $RbAg_4I_5$/graphite substantially increases the silver diffusivity. At room temperature, the extremely high D^δ value exceeds all the reported values for other solids and even values of NaCl in liquid water by at least one order of magnitude.

4.4 Conclusion

In this chapter we experimentally investigate the interfacial storage by fabricating all-solid-state storage devices. Since the all-solid-state cells have no passivation problems, they allow for a systematic study in the solid-solid interfacial properties. A full picture of the defect chemistry in the model system $RbAg_4I_5$/carbon has been established. The stoichiometric variation includes I_2 liberation, silver deficiency, silver excess, and silver deposition. The titration curve exhibits silver deficiency and excess take placing at the $RbAg_4I_5$/carbon interfaces. The silver deficiency is realized by silver vacancies (V'_{Ag}) on $RbAg_4I_5$ side and electron holes ($h^{\cdot}$) on the carbon side, while the excess must be realized by silver interstitials ($Ag_i^{\cdot}$) on one and excess electrons (e') on

the other side. The specific capacity increases with the contact area, indicating the storage really happens at the contact area.

The silver storage/removal of such composites is kinetically highly favorable. The obtained ultrahigh D^{δ} is well explained by the job-sharing chemical diffusion model. Owing to the electrostatic heterogeneity effect expressed by the built-in electrostatic field, the synergistic concept can significantly enhance the mass transport rate in ionic materials. The kinetically excellent $RbAg_4I_5$/carbon composites have been demonstrated in electrochemical applications including permeation membrane, battery electrode, and supercapacitor.

5

Main Conclusions

The present study comprehensively investigates the "job-sharing" mechanism that enables one to store matter at junction of an ionic conductor and an electronic conductor, even though the constituting phases could not accommodate the matter alone. By splitting the species into ions and electrons, the storage is realized by the ions residing on the side of ionic conductor while electrons on the electronic conductor side. Different from conventional mechanisms that store mass in the bulk regions of host materials, the interfacial (job-sharing) storage mechanism accommodates the mass in the space charge regions. As shown here, it also allows for establishing deficiency, realized by forming ion vacancies coupled with electron holes.

This thesis covers three main parts: theory of the mechanism, experimental evidence, and applications. A generalized model is developed to deal with the charge carrier distributions at different junctions. When the storage capacity is marginal, it is necessary to consider the contribution of all types of charge carriers, i.e. interstitial ions, ion vacancies, electrons, and holes. This storage domain is called intrinsically dominated mode where the metal activity a_M is constant. On storage capacity increase, the contributions of counter charges become less important. Once the counter charge carriers are negligible, the situation is simply dominated by the major carriers in the diffusive layers. This storage domain is thus termed the diffusive-layer dominated regime where $a_M \propto Q^{\pm n}$. The third storage regime emerges when significant amounts of stored charges locate in the rigid layers, leading to a perceptible electrostatic potential drop

over the interfaces. In this case, the system shows a transition from a chemical capacitor to an electrostatic capacitor with the dependence $a_M \propto e^{\gamma Q}$.

Since the generalized model is determined by several physical parameters, the evaluation of parameter variation could give a quantitative overview of the model. For instance, a rise of mass action law constant K_B leads to the change of the interfacial defect chemistry and thus the jump of the equilibrium potential around the stoichiometric point is reduced. An extreme case is when both K_F and K_B are very high, i.e. superionic conductor/(weak) metal interface, the E vs. Q curve will be a straight line. The predicted behavior is observed in the case of $RbAg_4I_5$/carbon junction.

Lithium storage is the key issue of Li based batteries. Li (i.e. Li^+ and e^-) can be reversibly brought from one electrode to the other according to their different chemical Li potentials. Here the Li^+ is transported through the electrolyte and e^- through the outer part of the circuit. As the e^- in the external circuit is able to perform electrical work, the concept allows for a reversible transformation between chemical energy and electrical energy. One scope of the study is to investigate the job-sharing storage of lithium in the model system LiF/Ni nanocomposites (≈ 1-2 nm grain size). As neither LiF (pure ionic conductor with large band gap) nor Ni (metal but not alloying with Li) could accommodate Li individually, the Li storage in the composites is only thermodynamically feasible in the space charge regions of LiF/Ni contacts. The quantitative analysis shows a transition from the diffusive-layer dominated mode to the rigid-layer dominated mode. It is shown that at interfaces one is able to establish not only Li excess but also Li deficiency. Moreover, the extracted parameters n and γ for Li storage are in agreement with those for Li removal. It indicates that the stoichiometric change of the composites is mainly due to the physical properties of the LiF/Ni junctions rather than side reactions. The finding of interfacial storage is also important for a complete understanding of conventional storage mechanism. As ionic materials always contain bulk and boundary zones, it is necessary to unify bulk and space charge storage, in particular for nanocrystalline electrodes.

Another experimental corroboration is Ag storage at $RbAg_4I_5$/carbon junctions, investigated by using all-solid-state electrochemical cells. $RbAg_4I_5$ is a silver superionic conductor with very high ionic concentration and very low electronic concentration. On the other hand, carbon (e.g. graphite) is a good electronic conductor exhibiting p- or n-type conductivity. These characteristic properties result in the $RbAg_4I_5$/carbon junction being a good model system for studying Ag non-

stoichiometry at interfaces. Within the range bound by Ag deposition (lower limit) and I_2 liberation (upper limit), the coulometric titration curve shows a distinct stoichiometric variation including silver excess ($Ag_i^{\cdot}/e'$) and deficiency ($V'_{Ag}/h^{\cdot}$). The storage capacity increases with contact area, indicating that the stoichiometric change occurs at the $RbAg_4I_5$/carbon contacts.

The aforementioned results have experimentally proved the heterogeneous mass storage being consistent with the developed model. In addition, the Ag storage/removal process in $RbAg_4I_5$/graphite composites is found to be very fast, owing to a novel mass transport mechanism (job-sharing chemical diffusion). As the ions and electrons move along the interfaces, the mass transport specifically refers to the local movement in the space charge regions. The anomalously high mass transport needs both very low chemical resistance and very low chemical capacitance. As far as the resistance is concerned, the synergistic concept offers additional degrees of freedom in that one can independently have ionic conductivity by selecting a good ionic conductor (e.g. $RbAg_4I_5$) and electronic conductivity by selecting a good electronic conductor (e.g. graphite). As far as the capacitance is concerned, the characteristic electrostatic heterogeneity effect, expressed by the built-in electrostatic field, can significantly suppress the chemical capacitance and hence enhance the mass transport rate. The apparent chemical diffusion coefficient of $RbAg_4I_5$/graphite composites is thus extremely high and even exceeds the value of NaCl in liquid water by one order of magnitude.

The marvelous kinetics of the job-sharing concept leads to excellent performance in the applications including batteries, supercapacitors, and permeation membranes. The fabricated Ag all-solid-state batteries can be charged at extremely high rate of 1240C (corresponding to charge/discharge within 2.9 seconds). In addition, the all-solid-state supercapacitor, based on the novel working principle with excess on one electrode side and deficiency on the other, exhibits an extremely short relaxation time (40 ms) close to a recent record value observed in liquid systems. At last, the ultrafast chemical diffusion of $RbAg_4I_5$/graphite composites allows for a usually high Ag permeation rate at room temperature. We hope that the present thesis can pave the way for a systematic research on a new class of novel mixed conducting materials.

Appendix I

Combining equation (2.1) and (2.2) yields Poisson-Boltzmann equation

$$\nabla^2\Phi = -\frac{F}{\varepsilon\varepsilon_0}\sum_j z_j c_{j\infty}\, exp\left(\frac{-Z_j F(\Phi-\Phi_\infty)}{RT}\right). \qquad (A.I.1)$$

Abbreviating $\frac{d\Phi}{dx} = f$, then $\frac{d^2\Phi}{dx^2}$ can be rewritten as $\frac{df}{dx} = \frac{df}{d\Phi}\frac{d\Phi}{dx} = \frac{df}{d\Phi}f$ and equation (A.I.1) as

$$\int f df = -\frac{F}{\varepsilon\varepsilon_0}\int \sum_j Z_j c_{j\infty} exp\left(\frac{-Z_j F(\Phi-\Phi_\infty)}{RT}\right) d\Phi. \qquad (A.I.2)$$

With the boundary condition $\Phi(x=\infty) - \Phi_\infty = 0 = f(x=\infty)$, it yields

$$-\frac{d\Phi}{dx} = -\sqrt{\frac{2RT}{\varepsilon\varepsilon_0}\sum_j\left(c_{j\infty} exp\left(\frac{-Z_j F(\Phi-\Phi_\infty)}{RT}\right) - c_{j\infty}\right)}. \qquad (2.3)$$

For the case of monovalent defect, the term in the bracket of equation (2.3) can be rewritten as

$$c_{j\infty}\left(exp\left(\frac{-F(\Phi-\Phi_\infty)}{RT}\right) - 2 + exp\left(\frac{F(\Phi-\Phi_\infty)}{RT}\right)\right) = \left(\sqrt{c_{j\infty}}\right)^2\left(exp\left(\frac{-F(\Phi-\Phi_\infty)}{2RT}\right) - exp\left(\frac{F(\Phi-\Phi_\infty)}{2RT}\right)\right)^2,$$

and yielding equation (2.4)

$$-\frac{d\Phi}{dx} = -\sqrt{\frac{2RT}{\varepsilon\varepsilon_0}}\left(\sqrt{c_i(x)} - \sqrt{c_v(x)}\right).$$

The total stored charge thus can be obtained, according to Poisson equation ($\rho = -\varepsilon\varepsilon_0\frac{d^2\Phi}{dx^2}$) and the boundary condition $\frac{d\Phi_\infty}{dx} = 0$, by integrating the charge density from $x_\alpha = 0$ to $x_\alpha = \infty$

$$Q_\alpha = \int_0^\infty \rho(x)dx_\alpha = \sqrt{2\varepsilon_\alpha\varepsilon_0 RT}\left(\sqrt{c_i(0)} - \sqrt{c_v(0)}\right). \qquad (2.5)$$

Appendix II

Equilibrium picture at the job-sharing contact of a weakly disordered ion conductor and a weakly disordered electronic conductor is shown in Figure A.II.1. As most strictly speaking the ionic crystal contains ($M_i^{\cdot}, V_M', e', h^{\cdot}$) four charge carriers (even though the ionic defect concentrations are orders of magnitude higher than the electronic defect concentrations, e.g. LiF) and electronic conductor contains three ($M_i^{\cdot}, e', h^{\cdot}$) charge carriers. The constancy of the potentials given at the bottom throughout the phases assumes that there are, on a low level, electronic carriers in phase α and M interstitials in phase β.

The electrochemical equilibrium of the M incorporation reaction is given by

$$\tilde{\mu}_M = \tilde{\mu}_{\mathrm{M}_i^{\bullet}} + \tilde{\mu}_{\mathrm{e}'} \ . \tag{2.14}$$

As eqn. (2.5) shows that the total charge (Q) is related with the concentration at the outmost layer, we specifically refer the electrochemical potentials of $\mathrm{M}_i^{\bullet}$ and e' to the outmost positions, i.e. $\tilde{\mu}_{\mathrm{M}_i^{\bullet}}(x_\alpha = 0)$ and $\tilde{\mu}_{\mathrm{e}'}(x_\beta = 0)$. For dilute considerations, eqn. (2.14) can be rewritten as

$$\mu_{\mathrm{M}}^0 + RT \ln a_{\mathrm{M}}$$
$$= \mu_{\mathrm{M}_i^{\bullet}}^0 + RT \ln c_i(x_\alpha = 0) + F\phi_\alpha(x_\alpha = 0) + \mu_{\mathrm{e}'}^0 + RT \ln c_n\big(x_\beta = 0\big) - F\phi_\beta\big(x_\beta = 0\big) \quad \text{(A. II. 1)}$$

where μ_j^0 is the standard potential of species j.

Rearranging (A.II.1) yields equation (2.15) in the main text:

$$\frac{c_i(0)c_n(0)}{a_{\mathrm{M}}} = K_M \times \exp\left(\frac{-F(\Phi_\alpha(0) - \Phi_\beta(0))}{RT}\right)$$

with $K_M = \exp\left(\frac{\mu_{\mathrm{M}}^0 - \mu_{\mathrm{M}_i^{\bullet}}^0 - \mu_{\mathrm{e}'}^0}{RT}\right)$.

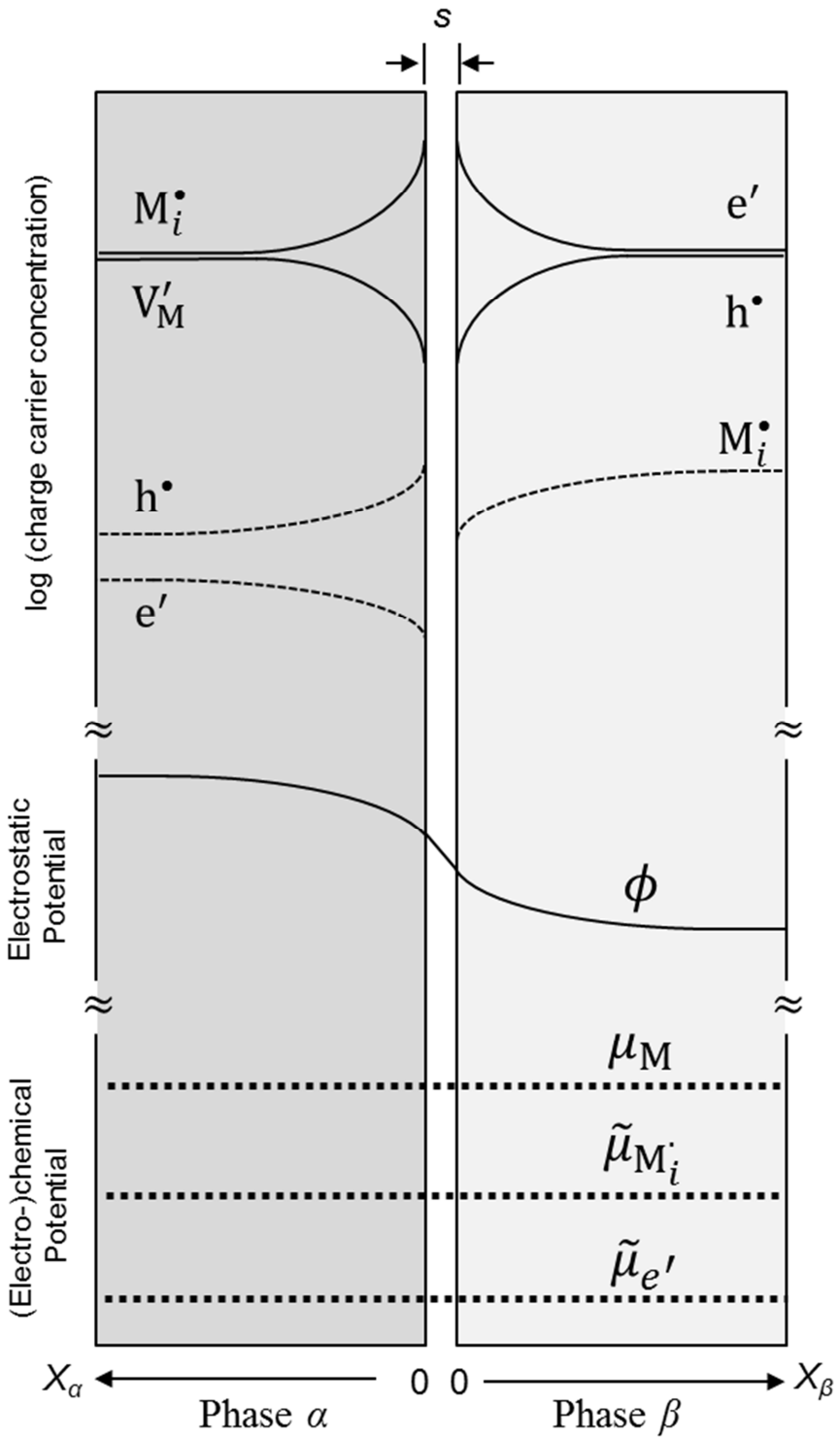

Figure A.II.1. Equilibrium picture at a weakly disordered ion conductor / weakly disordered electronic conductor junction.

Appendix III

For rigid layer dominant mode, the lithium activity a_{Li} is proportional to $e^{\gamma Q}$, where $\gamma = \frac{FS}{\bar{\varepsilon}\varepsilon_0 RT}$. Note that here Q refers to the charge per unit area. In battery application, the capacity usually refers to charge per unit mass. If we assume the Ni particles are almost fully covered by LiF (but the percolation is still guaranteed), one can replace Q by capacity per unit mass (Q_M), weight of composite electrode (M_{com}), and the contact area (A).

$$Q = \frac{Q_M M_{com}}{A} \tag{A. III. 1}$$

If, for Ni, spherical particles are assumed with radius (r_{Ni}) and density (ρ_{Ni}), the above equation yields

$$Q = \frac{Q_M M_{Ni}}{A}\left(\frac{M_{com}}{M_{Ni}}\right) = \frac{Q_M \rho_{Ni} \frac{4\pi}{3} r_{Ni}^3}{4\pi r_c^2}\left(\frac{M_{com}}{M_{Ni}}\right) = \frac{Q_M \rho_{Ni} r_{Ni}}{3}\left(\frac{M_{com}}{M_{Ni}}\right) \tag{A. III. 2}$$

where M_{Ni} is the weight of Ni in the composite. By using lithium metal as reference electrode, the dependence of equilibrium (E) potential can be described as

$$E = \text{const.} - \left[\frac{\rho_{Ni} r_{Ni} S}{3\bar{\varepsilon}\varepsilon_0}\left(\frac{M_{com}}{M_{Ni}}\right)\right] Q_M \,. \tag{A. III. 3}$$

The molar weight of the composites is determined by averaging the molar weight of Ni and LiF. The expression of γ thus can be obtained by rewriting (A.III.3)

$$\gamma = \frac{F \rho_{Ni} r_{Ni} S}{3RT\bar{\varepsilon}\varepsilon_0}\left(\frac{M_{Ni} + 2M_{LiF}}{M_{Ni}}\right). \tag{A. III. 4}$$

Appendix

With typical parameters ($\bar{\varepsilon} = 10$, $s = 0.3$ nm, r_{Ni}=1nm, ρ_{Ni}=8.91g cm^{-3}, M_{Ni}=59, ρ_{LiF}=2.64 g cm^{-3}, M_{LiF}=26), the γ value is 2.35 g (mAh)$^{-1}$.

On the other hand, if we assume LiF being embedded in Ni, then γ is expressed as

$$\gamma = \frac{F\rho_{LiF}r_{LiF}s}{6RT\bar{\varepsilon}\varepsilon_0}\left(\frac{M_{Ni} + 2M_{LiF}}{M_{LiF}}\right) \qquad \text{(A. III. 5)}$$

and the corresponding value is 0.79 g (mAh)$^{-1}$.

In view of the complexity of the system, it is pertinent to assume γ to be on the order of 1 g (mAh)$^{-1}$, which is in a good agreement with our experimental observation in Chapter 3.

Appendix IV

If we assume that a charge species *j* moves through a unit volume with cross section area A and thickness *L*, the resistance is expressed as

$$R_j = \frac{1}{\sigma_j}\frac{L}{A} \tag{A.IV.1}$$

and the capacitance is the derivative of storage charge Q_j (unit: coulomb) with respect to the potential E_j (unit: volt)

$$C_j = \frac{dQ_j}{dE_j} = \frac{FAL\, dc_j}{\frac{\mu_j}{F}} \tag{A.IV.2}$$

where c_j and μ_j are the concentration and chemical potential of species *j*. Equation (A.IV.2) can be rewritten as

$$C_j = \frac{ALF^2}{RT}\frac{dc_j}{d\ln a_j} = \frac{ALF^2}{RT}c_j\frac{d\ln c_j}{d\ln a_j} \tag{A.IV.3}$$

Since the chemical diffusion of neutral component relies on the ambipolar motion of ions and electrons, the transmission line model in reference [98] suggests the chemical resistance R^δ and chemical capacitance C^δ are

$$R^\delta = \left(\frac{1}{\sigma_{ion}} + \frac{1}{\sigma_e}\right)\frac{L}{A} = \frac{\sigma_{ion}+\sigma_e}{\sigma_{ion}\sigma_e}\frac{L}{A} \tag{A.IV.4}$$

$$C^\delta = \frac{ALF^2}{RT}\left(\frac{1}{c_{ion}}\frac{d\ln a_{ion}}{d\ln c_{ion}} + \frac{1}{c_e}\frac{d\ln a_e}{d\ln c_e}\right)^{-1}. \tag{A.IV.5}$$

The time constant is thus given as

$$\begin{aligned} R^\delta C^\delta &= \frac{L^2F^2}{RT}\frac{\sigma_{ion}+\sigma_e}{\sigma_{ion}\sigma_e}\left(\frac{1}{c_{ion}}\frac{d\ln a_{ion}}{d\ln c_{ion}} + \frac{1}{c_e}\frac{d\ln a_e}{d\ln c_e}\right)^{-1} \\ &= \frac{L^2}{\frac{RT}{F^2}\frac{\sigma_{ion}\sigma_e}{\sigma_{ion}+\sigma_e}\left(\frac{1}{c_{ion}}\frac{d\ln a_{ion}}{d\ln c_{ion}} + \frac{1}{c_e}\frac{d\ln a_e}{d\ln c_e}\right)} = \frac{L^2}{D^\delta}. \end{aligned} \tag{A.IV.6}$$

List of Symbols

A	Cross section area of electrode
a_e	Activity of electron of a classic mixed conductor
a_e^{β}	Activity of electron in phase β
a_{ion}	Activity of ion of a classic mixed conductor
a_{ion}^{α}	Activity of ions in phase α
a_{Li}	The activity of lithium
a_M	The activity of M
c_{Ag}	Concentration of silver
c_e	Concentration of electron of a classic mixed conductor
c_e^{β}	Concentration of electrons in phase β
$c_e^{\beta\,\prime\prime}$	Concentration of excess electrons in phase β
c_h	Concentration of electron hole
c_i	Concentration of metal ion interstitial
c_{ion}	Concentration of ion of a classic mixed conductor
c_{ion}^{α}	Concentration of ion in phase α
$c_{ion}^{\alpha\ \prime\prime}$	Concentration of excess ions in phase α
c_j	Concentration of charge carrier *j*
$c_{j\infty}$	Bulk concentration of charge carrier *j*
c_M	Concentration of species M
c_n	Concentration of electron
c_v	Concentration of metal ion vacancy
C^{δ}	Chemical capacitance
c_{∞}	Bulk concentration
$C'(\omega)$	Real part of the complex capacitance

$C''(\omega)$	Imaginary part of the complex capacitance
D^{δ}	Chemical diffusion coefficient
E	The equilibrium potential vs. M/M^{+}
E_0	Electric field in the charge free zone
e'	Electron
F	Faraday constant
h	Electron hole
I	Current
j_{Ag}	Molar flux of silver
j_e^{β}	Mass flux of electrons in phase β
j_{ion}^{α}	Mass flux of ion in phase α
j_M	Molar flux of species M
K_M	Mass action law constant for M storage
K_B	Mass action law constant of electron-hole equilibrium
K_F	Frenkel constant
L	Length of electrode
M	Metal
$M_i^{\cdot}$	Metal ion interstitial
M_M	Cation on its regular site
$\overline{M_W}$	Average molar mass of composite
n	Power number of diffusive-dominated storage
Q	Total stored charge
q	Stored charge by coulometric titration
Q_M	Stored capacity per unit mass
Q_{α}	Total charge in phase α
Q_{β}	Total charge in phase α
R	Universal gas constant
R^{δ}	Chemical resistance
s	Charge free zone distance
T	Temperature

List of Symbols

t	Diffusion time
u_e	The mobility of electron
V_i	Vacancy on the interstitial site
V'_{Li}	Lithium ion vacancy
V'_M	Metal ion vacancy
V_M	Molar volume of composite
Z_e	Charge number of electronic charge carrier
Z_j	Charge number of species *j*
Z'	The real part of the impedance
Z''	The imaginary part of the impedance
γ	$= \frac{Fs}{\bar{\varepsilon}\varepsilon_0 RT}$
δ	Non-stoichiometry
ε	Elative permittivity
$\bar{\varepsilon}$	Mean relative permittivity
ε_α	Relative permittivity of phase α
ε_β	Relative permittivity of phase β
ε_0	Vacuum permittivity
λ_β	Space charge layer thickness in phase β
λ_α	Space charge layer thickness in phase α
$\tilde{\mu}_{e'}$	Electrochemical equilibrium e'
μ_e^β	Chemical potential of electrons in β
$\overline{\mu_e^\beta}$	Electrochemical potential of electrons in phase β
μ_{ion}^α	Chemical potential of ion in phase α
$\overline{\mu_{ion}^\alpha}$	Electrochemical potential of ion in phase α
$\tilde{\mu}_M$	Electrochemical equilibrium of M
$\tilde{\mu}_{M_i^\cdot}$	Electrochemical equilibrium $M_i^\cdot$
ρ	Charge density
$\bar{\rho}$	Average density of composite
τ	Delay time constant of permeation experiment

τ_0	The relaxation time of supercapacitor
σ_e	Electronic conductivity of a classic mixed conductor
σ_e^{β}	Electronic conductivity in phase β
σ_{ion}	Ionic conductivity of a classic mixed conductor
σ_{ion}^{α}	Ionic conductivity in phase α
Φ	Electrostatic potential
Φ_e^{β}	The electric potential of electrons in β
Φ_{ion}^{α}	The electric potential of ions in phase α
ω	Frequency of impedance

References

[1] J.M. Tarascon, M. Armand. Issues and challenges facing rechargeable lithium batteries. *Nature* **414**, 359-367 (2001).

[2] M. Armand, J.M. Tarascon. Building better batteries. *Nature* **451**, 652-657 (2008).

[3] B. Dunn, H. Kamath, J.-M. Tarascon. Electrical Energy Storage for the Grid: A Battery of Choices. *Science* **334**, 928-935 (2011).

[4] J. Maier. Mass storage in space charge regions of nano-sized systems (Nano-ionics. Part V). *Faraday Discussions* **134**, 51-66 (2007).

[5] J. Maier. Thermodynamics of Electrochemical Lithium Storage. *Angewandte Chemie International Edition* **52**, 4998-5026 (2013).

[6] Y. Shao-Horn, L. Croguennec, C. Delmas, E.C. Nelson, M.A. O'Keefe. Atomic resolution of lithium ions in LiCoO2. *Nat Mater* **2**, 464-467 (2003).

[7] W.T. Petuskey. Interfacial effects on Ag:S nonstoichiometry in silver sulfide/alumina composites. *Solid State Ionics* **21**, 117-129 (1986).

[8] C. Wagner. Investigations on Silver Sulfide. *The Journal of Chemical Physics* **21**, 1819-1827 (1953).

[9] U.V. Oehsen, H. Schmalzried. Thermodynamic investigations of Ag_2Se. *Berichte der Bunsengesellschaft für physikalische Chemie* **85**, 7-14 (1981).

[10] T. Takahashi, O. Yamamoto. Solid-State Ionics—Coulometric Titrations and Measurements of the Ionic Conductivity of Beta Ag_2Se and Beta Ag_2Te and Use of These Compounds in an Electrochemical Analog Memory Element. *Journal of The Electrochemical Society* **118**, 1051-1057 (1971).

[11] G. Beck, J. Janek. Coulometric titration at low temperatures—nonstoichiometric silver selenide. *Solid State Ionics* **170**, 129-133 (2004).

[12] C. Wagner. The determination of small deviations from the ideal stoichiometric composition of ionic crystals and other binary compounds. *Progress in Solid State Chemistry* **6**, 1-15 (1971).

[13] J. Jamnik, J. Maier. Nanocrystallinity effects in lithium battery materials Aspects of nano-ionics. Part IV. *Physical Chemistry Chemical Physics* **5**, 5215-5220 (2003).

[14] C. Zhu, X. Mu, J. Popovic, K. Weichert, P.A. van Aken, Y. Yu, J. Maier. Lithium Potential Variations for Metastable Materials: Case Study of Nanocrystalline and Amorphous LiFePO4. *Nano Letters* **14**, 5342-5349 (2014).

[15] P. Poizot, S. Laruelle, S. Grugeon, L. Dupont, J.M. Tarascon. Nano-sized transition-metal oxides as negative-electrode materials for lithium-ion batteries. *Nature* **407**, 496-499 (2000).

[16] H. Li, P. Balaya, J. Maier. Li-Storage via Heterogeneous Reaction in Selected Binary Metal Fluorides and Oxides. *Journal of The Electrochemical Society* **151**, A1878-A1885 (2004).

[17] J. Cabana, L. Monconduit, D. Larcher, M.R. Palacin. Beyond Intercalation-Based Li-Ion Batteries: The State of the Art and Challenges of Electrode Materials Reacting Through Conversion Reactions. *Advanced Materials* **22**, E170-E192 (2010).

[18] F. Wang, R. Robert, N.A. Chernova, N. Pereira, F. Omenya, F. Badway, X. Hua, M. Ruotolo, R. Zhang, L. Wu, V. Volkov, D. Su, B. Key, M.S. Whittingham, C.P. Grey, G.G. Amatucci, Y. Zhu, J. Graetz. Conversion Reaction Mechanisms in Lithium Ion Batteries: Study of the Binary Metal Fluoride Electrodes. *Journal of the American Chemical Society* (2011).

[19] C.-X. Zu, H. Li. Thermodynamic analysis on energy densities of batteries. *Energy & Environmental Science* **4**, 2614-2624 (2011).

[20] P. Balaya, H. Li, L. Kienle, J. Maier. Fully Reversible Homogeneous and Heterogeneous Li Storage in RuO_2 with High Capacity. *Advanced Functional Materials* **13**, 621-625 (2003).

[21] H. Li, G. Richter, J. Maier. Reversible Formation and Decomposition of LiF Clusters Using Transition Metal Fluorides as Precursors and Their Application in Rechargeable Li Batteries. *Advanced Materials* **15**, 736-739 (2003).

[22] Y.F. Zhukovskii, P. Balaya, E.A. Kotomin, J. Maier. Evidence for Interfacial-Storage Anomaly in Nanocomposites for Lithium Batteries from First-Principles Simulations. *Physical Review Letters* **96**, 058302 (2006).

References

[23] Y.F. Zhukovskii, P. Balaya, M. Dolle, E.A. Kotomin, J. Maier. Enhanced lithium storage and chemical diffusion in metal-LiF nanocomposites: Experimental and theoretical results. *Physical Review B* **76**, 235414 (2007).

[24] L. Fu, C.-C. Chen, D. Samuelis, J. Maier. Thermodynamics of Lithium Storage at Abrupt Junctions: Modeling and Experimental Evidence. *Physical Review Letters* **112**, 208301 (2014).

[25] C.C. Liang. Conduction Characteristics of the Lithium Iodide - Aluminum Oxide Solid Electrolytes. *Journal of The Electrochemical Society* **120**, 1289-1292 (1973).

[26] J. Maier. Space charge regions in solid two-phase systems and their conduction contribution—I. Conductance enhancement in the system ionic conductor-'inert' phase and application on AgC1:Al2O3 and AgC1:SiO2. *Journal of Physics and Chemistry of Solids* **46**, 309-320 (1985).

[27] N. Sata, K. Eberman, K. Eberl, J. Maier. Mesoscopic fast ion conduction in nanometre-scale planar heterostructures. *Nature* **408**, 946-949 (2000).

[28] P. Lupetin, G. Gregori, J. Maier. Mesoscopic Charge Carriers Chemistry in Nanocrystalline $SrTiO_3$. *Angewandte Chemie International Edition* **49**, 10123-10126 (2010).

[29] C. Li, X. Guo, L. Gu, D. Samuelis, J. Maier. Ionic Space-Charge Depletion in Lithium Fluoride Thin Films on Sapphire (0001) Substrates. *Advanced Functional Materials* **21**, 2901-2905 (2011).

[30] C. Li, L. Gu, X. Guo, D. Samuelis, K. Tang, J. Maier. Charge Carrier Accumulation in Lithium Fluoride Thin Films due to Li-Ion Absorption by Titania (100) Subsurface. *Nano Letters* **12**, 1241-1246 (2012).

[31] C. Li, L. Gu, J. Maier. Enhancement of the Li Conductivity in LiF by Introducing Glass/Crystal Interfaces. *Advanced Functional Materials* **22**, 1145-1149 (2012).

[32] J. Maier. Space Charge Regions in Solid Two Phase Systems and Their Conduction Contribution — II Contact Equilibrium at the Interface of Two Ionic Conductors and the Related Conductivity Effect. *Berichte der Bunsengesellschaft für physikalische Chemie* **89**, 355-362 (1985).

[33] C. Li, J. Maier. Ionic space charge effects in lithium fluoride thin films. *Solid State Ionics* **225**, 408-411 (2012).

[34] H. Yamada, A.J. Bhattacharyya, J. Maier. Extremely High Silver Ionic Conductivity in Composites of Silver Halide (AgBr, AgI) and Mesoporous Alumina. *Advanced Functional Materials* **16**, 525-530 (2006).

[35] H.L. Tuller, S.R. Bishop. Point Defects in Oxides: Tailoring Materials Through Defect Engineering. *Annual Review of Materials Research* **41**, 369-398 (2011).

[36] J. Maier. Defect chemistry and ion transport in nanostructured materials: Part II. Aspects of nanoionics. *Solid State Ionics* **157**, 327-334 (2003).

[37] S.O. Kasap. *Principles of electronic materials and devices*, McGraw-Hill New York, NY, (2006).

[38] C. Barlow Jr. The electrical double layer, in: H. Eyring (Ed.) *Physical Chemistry, An Advanced Treatise*, Academic Press Inc. , New York, (1970), pp. 167-246.

[39] R.D. Armstrong, B.R. Horrocks. The double layer structure at the metal-solid electrolyte interface. *Solid State Ionics* **94**, 181-187 (1997).

[40] J. Maier. *Physical chemistry of ionic materials: ions and electrons in solids*, John Wiley & Sons, (2004).

[41] R.A. Robinson, R.H. Stokes. Tables of osmotic and activity coefficients of electrolytes in aqueous solution at 25 C. *Transactions of the Faraday Society* **45**, 612-624 (1949).

[42] K. Funke. AgI-type solid electrolytes. *Progress in Solid State Chemistry* **11, Part 4**, 345-402 (1976).

[43] J. Maier, W. Münch. Thermal Destiny of an Ionic Crystal. *Zeitschrift für anorganische und allgemeine Chemie* **626**, 264-269 (2000).

[44] J. Maier. Ionic and electronic carriers in solids—physical and chemical views of the equilibrium situation. *Solid State Ionics* **143**, 17-23 (2001).

[45] N. Kimura, T. Osaki, S. Toshima. Interfacial Capacity between a Silver Bromide Solid Electrolyte and a Blocking Electrode. *Bulletin of the Chemical Society of Japan* **48**, 830-834 (1975).

[46] A.K. Padhi, K.S. Nanjundaswamy, J.B. Goodenough. Phospho-olivines as Positive-Electrode Materials for Rechargeable Lithium Batteries. *Journal of The Electrochemical Society* **144**, 1188-1194 (1997).

References

[47] S. Laruelle, S. Grugeon, P. Poizot, M. Dolle, L. Dupont, J.-M. Tarascon. On the Origin of the Extra Electrochemical Capacity Displayed by MO/Li Cells at Low Potential. *Journal of The Electrochemical Society* **149**, A627-A634 (2002).

[48] Y.-Y. Hu, Z. Liu, K.-W. Nam, O.J. Borkiewicz, J. Cheng, X. Hua, M.T. Dunstan, X. Yu, K.M. Wiaderek, L.-S. Du, K.W. Chapman, P.J. Chupas, X.-Q. Yang, C.P. Grey. Origin of additional capacities in metal oxide lithium-ion battery electrodes. *Nature Materials* **12**, 1130-1136 (2013).

[49] J. Maier. Kröger-Vink diagrams for boundary regions. *Solid State Ionics* **32-33, Part 2**, 727-733 (1989).

[50] P. Liu, J.J. Vajo, J.S. Wang, W. Li, J. Liu. Thermodynamics and Kinetics of the Li/FeF_3 Reaction by Electrochemical Analysis. *The Journal of Physical Chemistry C* **116**, 6467-6473 (2012).

[51] P. Verma, P. Maire, P. Novák. A review of the features and analyses of the solid electrolyte interphase in Li-ion batteries. *Electrochimica Acta* **55**, 6332-6341 (2010).

[52] P. Liao, B.L. MacDonald, R.A. Dunlap, J.R. Dahn. Combinatorially Prepared $[LiF]_{1-x}Fe_x$ Nanocomposites for Positive Electrode Materials in Li-Ion Batteries. *Chemistry of Materials* **20**, 454-461 (2007).

[53] A.J. Gmitter, F. Badway, S. Rangan, R.A. Bartynski, A. Halajko, N. Pereira, G.G. Amatucci. Formation, dynamics, and implication of solid electrolyte interphase in high voltage reversible conversion fluoride nanocomposites. *Journal of Materials Chemistry* **20**, 4149-4161 (2010).

[54] B.E. Conway. *Electrochemical Supercapacitors: Scientific Fundamentals and Technological Applications*, Plenum Publishers, New York, (1999).

[55] T.G. Stoebe, R.A. Huggins. Measurement of ionic diffusion in lithium fluoride by nuclear magnetic resonance techniques. *J Mater Sci* **1**, 117-126 (1966).

[56] M. Eisenstadt. Nuclear Magnetic Relaxation in LiF at High Temperatures. *Physical Review* **132**, 630-635 (1963).

[57] J. Maier. On the conductivity of polycrystalline materials. *Berichte der Bunsengesellschaft für physikalische Chemie* **90**, 26-33 (1986).

[58] J.-Y. Shin, D. Samuelis, J. Maier. Sustained Lithium-Storage Performance of Hierarchical, Nanoporous Anatase TiO2 at High Rates: Emphasis on Interfacial Storage Phenomena. *Advanced Functional Materials* **21**, 3464-3472 (2011).

[59] C. Zhu, X. Mu, P.A. van Aken, Y. Yu, J. Maier. Single-Layered Ultrasmall Nanoplates of MoS2 Embedded in Carbon Nanofibers with Excellent Electrochemical Performance for Lithium and Sodium Storage. *Angewandte Chemie* **126**, 2184-2188 (2014).

[60] M. Faraday. *Experimental Researches in Electricity*, Taylor and Francis, London, (1839).

[61] W. Nernst. *Theoretische Chemie vom Standpunkte der Avogadroschen Regel und der Thermodynamik*, Enke, Stuttgart, (1926).

[62] J. Frenkel. Über die Wärmebewegung in festen und flüssigen Körpern. *Z. Physik* **35**, 652-669 (1926).

[63] C. Wagner, W. Schottky. Theorie der geordneten Mischphasen. *Zeitschrift für Physikalische Chemie B* **11**, 163-210 (1930).

[64] J. Maier. Ionic conduction in space charge regions. *Progress in Solid State Chemistry* **23**, 171-263 (1995).

[65] J. Maier. Nanoionics: ion transport and electrochemical storage in confined systems. *Nature Materials* **4**, 805-815 (2005).

[66] C. Tubandt, E. Lorenz. Molekularzustand und elektrisches Leitvermögen kristallisierter Salze. *Zeitschrift für Physikalische Chemie B* **24**, 513-543 (1914).

[67] L.W. Strock. Kristallstruktur des Hochtemperatur-Jodsilbers a-AgJ. *Zeitschrift für Physikalische Chemie B* **25**, 441-459 (1934).

[68] J.N. Bradley, P.D. Greene. Solids with high ionic conductivity in group 1 halide systems. *Transactions of the Faraday Society* **63**, 424-430 (1967).

[69] B.B. Owens, G.R. Argue. High-Conductivity Solid Electrolytes: MAg_4I_5. *Science* **157**, 308-310 (1967).

[70] S. Geller. Crystal Structure of the Solid Electrolyte, $RbAg_4I_5$. *Science* **157**, 310-312 (1967).

[71] K. Kinoshita. *Carbon: electrochemical and physicochemical properties*, Wiley–Interscience, New York, (1988).

[72] M.S. Dresselhaus, G. Dresselhaus. Intercalation compounds of graphite. *Advances in Physics* **51**, 1-186 (2002).

References

[73] E. Herrero, L.J. Buller, H.D. Abruña. Underpotential Deposition at Single Crystal Surfaces of Au, Pt, Ag and Other Materials. *Chemical Reviews* **101**, 1897-1930 (2001).

[74] M.N. Hull, A.A. Pilla. The Transient Behavior of Graphite-Silver Iodide and Platinum-Silver Iodide Interfaces in a Solid-State System. *Journal of The Electrochemical Society* **118**, 72-78 (1971).

[75] D.O. Raleigh. Electrochemical studies in a solid electrolyte system. *The Journal of Physical Chemistry* **71**, 1785-1797 (1967).

[76] R.D. Armstrong, R. Mason. Double layer capacity measurements involving solid electrolytes. *Journal of Electroanalytical Chemistry and Interfacial Electrochemistry* **41**, 231-241 (1973).

[77] D.O. Raleigh. Electrode Capacitance in Silver-Halide Solid Electrolyte Cells: I . Room Temperature Graphite and Platinum Electrodes. *Journal of The Electrochemical Society* **121**, 632-639 (1974).

[78] P.L. Taberna, P. Simon, J.F. Fauvarque Electrochemical Characteristics and Impedance Spectroscopy Studies of Carbon-Carbon Supercapacitors. *Journal of The Electrochemical Society* **150**, A292-A300 (2003).

[79] W. Sitte. Chemical diffusion in mixed conductors: α′-Ag_2Te and β-Ag_2Se. *Solid State Ionics* **94**, 85-90 (1997).

[80] B. Scrosati, G. Germano, G. Pistoia. Electrochemical Properties of $RbAg_4I_5$ Solid Electrolyte: I . Conductivity Studies. *Journal of The Electrochemical Society* **118**, 86-89 (1971).

[81] C. García, J.I. Franco, J.C. López Tonazzi, N.E. Walsöe de Reca. Conductivity behavior of $RbAg_4I_5$. *Solid State Ionics* **9**, 1233-1236 (1983).

[82] B. Yang, X.F. Liang, H.X. Guo, K.B. Yin, J. Yin, Z.G. Liu. Characterization of RbAg4I5 films prepared by pulsed laser deposition. *Journal of Physics D: Applied Physics* **41**, 115304 (2008).

[83] N. Valverde. Thermodynamic Stabilization of the Solid Electrolyte $RbAg_4I_5$. *Journal of The Electrochemical Society* **127**, 2425-2429 (1980).

[84] G.A. Kimmel, N.G. Petrik, Z. Dohnálek, B.D. Kay. Crystalline ice growth on Pt (111): Observation of a hydrophobic water monolayer. *Physical review letters* **95**, 166102 (2005).

[85] J.S. Hong, J.R. Selman. Relationship Between Calorimetric and Structural Characteristics of Lithium - Ion Cells II. Determination of Li Transport Properties. *Journal of The Electrochemical Society* **147**, 3190-3194 (2000).

[86] E. Bakken, T. Norby, S. Stølen. Nonstoichiometry and reductive decomposition of $CaMnO_{3-\delta}$. *Solid State Ionics* **176**, 217-223 (2005).

[87] J. Maier. Size effects on mass transport and storage in lithium batteries. *Journal of Power Sources* **174**, 569-574 (2007).

[88] H. Gerischer, R. McIntyre, D. Scherson, W. Storck. Density of the electronic states of graphite: derivation from differential capacitance measurements. *The Journal of Physical Chemistry* **91**, 1930-1935 (1987).

[89] A. Peigney, C. Laurent, E. Flahaut, R.R. Bacsa, A. Rousset. Specific surface area of carbon nanotubes and bundles of carbon nanotubes. *Carbon* **39**, 507-514 (2001).

[90] J. Maier. Evaluation of Electrochemical Methods in Solid State Research and Their Generalization for Defects with Variable Charges. *Zeitschrift für Physikalische Chemie* **140**, 191-215 (1984).

[91] J. Maier. On the correlation of macroscopic and microscopic rate constants in solid state chemistry. *Solid State Ionics* **112**, 197-228 (1998).

[92] J. Maier. Solid State Electrochemistry II: Devices and Techniques, in: C. Vayenas, R. White, M. Gamboa-Aldeco (Eds.) *Modern Aspects Of Electrochemistry*, Springer New York, (2007), pp. 1-138.

[93] J. Maier. Mass Transport in the Presence of Internal Defect Reactions—Concept of Conservative Ensembles: I, Chemical Diffusion in Pure Compounds. *Journal of the American Ceramic Society* **76**, 1212-1217 (1993).

[94] D. Grientschnig, W. Sitte. Interpretation of ionic transport properties of some silver chalcogenides. *Journal of Physics and Chemistry of Solids* **52**, 805-820 (1991).

[95] Y.-I. Jang, B.J. Neudecker, N.J. Dudney. Lithium Diffusion in Li x CoO2 ($0.45 < x < 0.7$) Intercalation Cathodes. *Electrochemical and Solid-State Letters* **4**, A74-A77 (2001).

[96] A. Bürgermeister, W. Sitte. Chemical diffusion in β-Ag_2Te. *Solid State Ionics* **141–142**, 331-334 (2001).

[97] J. Newman, K.E. Thomas-Alyea. *Electrochemical systems*, John Wiley & Sons, (2004).

References

[98] J. Jamnik, J. Maier. Generalised equivalent circuits for mass and charge transport: chemical capacitance and its implications. *Physical Chemistry Chemical Physics* **3**, 1668-1678 (2001).

[99] C. Wagner. Equations for transport in solid oxides and sulfides of transition metals. *Progress in Solid State Chemistry* **10, Part 1**, 3-16 (1975).

[100] W. Weppner, R.A. Huggins. Determination of the Kinetic Parameters of Mixed - Conducting Electrodes and Application to the System Li_3Sb. *Journal of The Electrochemical Society* **124**, 1569-1578 (1977).

[101] W. Sitte. Electrochemical cell for composition dependent measurements of chemical diffusion coefficients and ionic conductivities on mixed conductors and application to silver telluride at 160°C. *Solid State Ionics* **59**, 117-124 (1993).

[102] I. Yokota. On the Theory of Mixed Conduction with Special Reference to Conduction in Silver Sulfide Group Semiconductors. *Journal of the Physical Society of Japan* **16**, 2213-2223 (1961).

[103] W. Weppner, R.A. Huggins. Electrochemical methods for determining kinetic properties of solids. *Annual Review of Materials Science* **8**, 269-311 (1978).

[104] D.O. Raleigh. Ionic Conductivity of Single-Crystal and Polycrystalline $RbAg_4I_5$. *Journal of Applied Physics* **41**, 1876-1877 (1970).

[105] S. Ryu, L. Liu, S. Berciaud, Y.-J. Yu, H. Liu, P. Kim, G.W. Flynn, L.E. Brus. Atmospheric Oxygen Binding and Hole Doping in Deformed Graphene on a SiO_2 Substrate. *Nano Letters* **10**, 4944-4951 (2010).

[106] A. Arndt, D. Spoddig, P. Esquinazi, J. Barzola-Quiquia, S. Dusari, T. Butz. Electric carrier concentration in graphite: Dependence of electrical resistivity and magnetoresistance on defect concentration. *Physical Review B* **80**, 195402 (2009).

[107] Z. Fei, A. Rodin, W. Gannett, S. Dai, W. Regan, M. Wagner, M. Liu, A. McLeod, G. Dominguez, M. Thiemens. Electronic and plasmonic phenomena at graphene grain boundaries. *Nature Nanotechnology* **8**, 821-825 (2013).

[108] W.M. Haynes. *CRC handbook of chemistry and physics*, CRC press, (2013).

[109] G.L. Bottger, A.L. Geddes. Infrared Lattice Vibrational Spectra of AgCl, AgBr, and AgI. *The Journal of Chemical Physics* **46**, 3000-3004 (1967).

[110] S. Ergun, J.B. Yasinsky, J.R. Townsend. Transverse and longitudinal optical properties of graphite. *Carbon* **5**, 403-408 (1967).

[111] R. Shannon. Revised effective ionic radii and systematic studies of interatomic distances in halides and chalcogenides. *Acta Crystallographica Section A: Crystal Physics, Diffraction, Theoretical and General Crystallography* **32**, 751-767 (1976).

[112] S. Bredikhin, T. Hattori, M. Ishigame. Ambipolar diffusion in $RbAg_4I_5$. *Solid State Ionics* **67**, 311-316 (1994).

[113] H.J. Bouwmeester, A.J. Burggraaf, in: The CRC Handbook of Solid State Electrochemistry, 1997, pp. 481.

[114] A.W. Smith, F.W. Meszaros, C.D. Amata. Permeability of Zirconia, Hafnia, and Thoria to Oxygen. *Journal of the American Ceramic Society* **49**, 240-244 (1966).

[115] L. Heyne, N. Beekman. Electronic Transport in Calcia-stabilized Zirconia. *Proceedings of the British Ceramic Society* **19**, 229-263 (1971).

[116] K. Kitazawa, R.L. Coble. Use of Stabilized ZrO_2 to Measure O_2 Permeation. *Journal of the American Ceramic Society* **57**, 360-363 (1974).

[117] J. Crank. *The mathematics of diffusion*, Oxford university press, (1979).

[118] W. Preis, W. Sitte. Polarization studies on mixed conductors with comparable ionic and electronic conductivities employed in asymmetric electrochemical cells. *Solid State Ionics* **86–88, Part 2**, 779-784 (1996).

[119] H. Schmalzried. Ag_2S—The physical chemistry of an inorganic material. *Progress in Solid State Chemistry* **13**, 119-157 (1980).

[120] E.L. Cussler. *Diffusion: Mass Transfer in Fluid Systems*, Cambridge university press, (1997).

[121] M. Park, X. Zhang, M. Chung, G.B. Less, A.M. Sastry. A review of conduction phenomena in Li-ion batteries. *Journal of Power Sources* **195**, 7904-7929 (2010).

[122] C. Zhu, X. Mu, P.A. van Aken, J. Maier, Y. Yu. Fast Li Storage in MoS_2-Graphene-Carbon Nanotube Nanocomposites: Advantageous Functional Integration of 0D, 1D, and 2D Nanostructures. *Advanced Energy Materials* **5**, n/a-n/a (2015).

[123] C.K. Chan, H. Peng, G. Liu, K. McIlwrath, X.F. Zhang, R.A. Huggins, Y. Cui. High-performance lithium battery anodes using silicon nanowires. *Nat Nano* **3**, 31-35 (2008).

[124] C. Wang, Y. Zhou, M. Ge, X. Xu, Z. Zhang, J.Z. Jiang. Large-Scale Synthesis of SnO_2 Nanosheets with High Lithium Storage Capacity. *Journal of the American Chemical Society* **132**, 46-47 (2010).

References

[125] J. Oxley. A Solid State Electrochemical Capacitor. *141st Meeting of The Electrochemical Society, Houston, TX, Abstract 175* (1972).

[126] D. Pech, M. Brunet, H. Durou, P. Huang, V. Mochalin, Y. Gogotsi, P.-L. Taberna, P. Simon. Ultrahigh-power micrometre-sized supercapacitors based on onion-like carbon. *Nature Nanotechnology* **5**, 651-654 (2010).

[127] J. Mizusaki, K. Fueki. Electrochemical determinations of the chemical diffusion coefficient and non-stoichiometry in AgCl. *Solid State Ionics* **6**, 85-91 (1982).

[128] J. Barker, R. Pynenburg, R. Koksbang, M.Y. Saidi. An electrochemical investigation into the lithium insertion properties of Li_xCoO_2. *Electrochimica Acta* **41**, 2481-2488 (1996).

[129] R. Amin, P. Balaya, J. Maier. Anisotropy of Electronic and Ionic Transport in $LiFePO_4$ Single Crystals. *Electrochemical and Solid-State Letters* **10**, A13-A16 (2007).

[130] I. Rom, W. Sitte. Composition dependent ionic and electronic conductivities and chemical diffusion coefficient of silver selenide at 160°C. *Solid State Ionics* **101–103, Part 1**, 381-386 (1997).

[131] C.J. Wen, B.A. Boukamp, R.A. Huggins, W. Weppner. Thermodynamic and Mass Transport Properties of "LiAl" *Journal of The Electrochemical Society* **126**, 2258-2266 (1979).

[132] K. Sasaki, J. Maier. In situ EPR studies of chemical diffusion in oxides. *Physical Chemistry Chemical Physics* **2**, 3055-3061 (2000).

[133] I. Denk, F. Noll, J. Maier. In situ Profiles of Oxygen Diffusion in $SrTiO_3$: Bulk Behavior and Boundary Effects. *Journal of the American Ceramic Society* **80**, 279-285 (1997).

[134] A. Belzner, T.M. Gür, R.A. Huggins. Oxygen chemical diffusion in strontium doped lanthanum manganites. *Solid State Ionics* **57**, 327-337 (1992).

[135] X. Turrillas, J.A. Kilner, I. Kontoulis, B.C.H. Steele. Oxygen transport in superconducting ceramic $YBa_2Cu_3O_7$ and $(BiO_2)Sr_2Ca_{n-1}Cu_nO_{2n+2}$ samples. *Journal of the Less Common Metals* **151**, 229-236 (1989).

[136] O.H. Kwon, G.M. Choi. Electrical conductivity of thick film YSZ. *Solid State Ionics* **177**, 3057-3062 (2006).

[137] K. Sasaki, J. Maier. Re-analysis of defect equilibria and transport parameters in Y_2O_3-stabilized ZrO_2 using EPR and optical relaxation. *Solid State Ionics* **134**, 303-321 (2000).

Curriculum Vitae

Name :	Chia-Chin Chen
Nationality:	Taiwan
Date of Birth:	1982.12.29
Place of Birth:	Taichung, Taiwan

Aug. 2011– Feb. 2016	Ph.D. in Chemistry Max Planck Institute for Solid State Research Stuttgart, Germany
Aug. 2007 – Aug. 2010	M.S. in Chemical Engineering Illinois Institute of Technology Chicago, U.S.A
Aug. 2005 – Oct. 2006	Military Service, Taiwan
Sept. 2001 – July 2005	B.S. in Chemical Engineering National Taiwan University Taipei, Taiwan